Technical Report
TR-20-04
October 2020

Buffer swelling

Laboratory tests and modelling

Torbjörn Sandén
Ola Kristensson
Margareta Lönnqvist
Lennart Börgesson
Ulf Nilsson
Reza Goudarzi

SVENSK KÄRNBRÄNSLEHANTERING AB

SWEDISH NUCLEAR FUEL
AND WASTE MANAGEMENT CO

Box 3091, SE-169 03 Solna
Phone +46 8 459 84 00
skb.se

SVENSK KÄRNBRÄNSLEHANTERING

ISSN 1404-0344
SKB TR-20-04
ID 1885431

October 2020
Updated 2020-12

Buffer swelling

Laboratory tests and modelling

Torbjörn Sandén, Ola Kristensson, Margareta Lönnqvist,
Lennart Börgesson, Ulf Nilsson, Reza Goudarzi

Clay Technology AB

Keywords: Buffer, Deposition holes, Backfill, Compressibility, KBP1018, Modelling, Swelling.

Update notice

The original report, dated October 2020, was found to contain both factual and editorial errors which have been corrected in this updated version. The corrected factual errors are presented below.

Updated 2020-12

Location	Original text	Corrected text
Page 87, Section 7.2, paragraph 4, line 2	…in Appendix 10.	…in Appendix 3.
Page 87, Section 7.2.1, paragraph 1, line 3	…in Appendix 11.	…in Appendix 4.

Abstract

A KBS-3V repository for spent nuclear fuel is planned to be built in Forsmark. In this concept, the underground facility consists of tunnels with eight-meter-deep deposition holes bored in the tunnel floor every sixth meter. The fuel is encapsulated in copper canisters, which are placed in the deposition holes. The canisters are surrounded by a buffer consisting of highly compacted buffer blocks and a pellet filled outer slot. The reference design for backfilling of the deposition tunnels is pre-compacted blocks placed in the tunnel and bentonite pellets that fill up the space between the blocks and the tunnel walls. Pellets will also be placed on the tunnel floor in order to even out the rough rock surface and by that provide a suitable surface on which the backfill blocks can be piled.

One of the most important tasks for the backfill is to restrict upwards swelling of the buffer from the deposition holes. When the buffer swells upwards it loses density and by that also important properties e.g. decrease in swelling pressure. A possible scenario that could lead to large expansion of the buffer is when the water inflow rate into the deposition tunnel is very low but at the same time there is a substantial water inflow into a deposition hole. This could lead to that the buffer in the deposition hole hydrates and swells when the backfill is still dry, which results in a pressure build up that will push the dry backfill upwards.

The scenario with buffer swelling upwards against a dry backfill has been investigated earlier, both by modelling, and by performing a full-scale test, the Buffer Swelling Test at Äspö HRL. The modelling and investigations were then focused on the two extreme cases, (1) the backfill has been fully water saturated or (2) the backfill has been completely dry, and this in combination with a fully water saturated buffer that has access to water in the entire rock buffer interface. The main reason for focusing on these extremes is lack of knowledge of the mechanical properties of partly water saturated systems and a hypothesis that the dry backfill is the most deformable case.

A new project concerning this matter was initiated in order to better understand the upwards swelling of the buffer and subsequent compression of the backfill at different wetting scenarios of both the backfill and the buffer. In this project several scale tests of both the deposition hole and the tunnel have been performed. Modelling of these cases has also been an important part of this project, which will continue coming years.

This report describes scale tests performed in laboratory to investigate the behaviour of buffer and backfill at different wetting scenarios. Two scale tests in the scale 1:10 of a deposition hole have been performed with different wetting scenarios. The backfill was in these tests simulated by a combination of springs placed in the top of the deposition hole with a force-displacement relation that corresponds to the expected resistance from a dry backfill according to the full-scale test at Äspö. They were run for about one year and then carefully sampled and the distribution of density and water content measured. Four scale tests in the scale 1:20 of a 6-meter-long section of a deposition tunnel above a deposition hole with different wetting scenarios have also been performed. A plate in the floor of the tunnel simulated the swelling buffer by displacing it upwards and simultaneously measures the force. The tests were run with between 0 days (dry test) and 52 days of wetting before simulating the upwards swelling and then carefully sampled with measurement of the distribution of density and water content.

The results from the tests were used to increase the understanding regarding different wetting scenarios and to study the possibility to upscale the results to full scale. Two important observations and preliminary conclusions from those tests were:

- Wetting of only the lowest part of the deposition hole (beneath the canister) may cause larger up swelling and larger local loss of density in the buffer than if the wetting is evenly distributed along the rock surface.
- The dry case of the tunnel backfill seems to be more critical and yield less resistance to swelling than other types of wetting scenarios.

In parallel, development of new numerical models, of both buffer and backfill behaviour, have been made since it has been judged that there is a need to verify and develop the present models so that they can also be used for calculations of different wetting scenarios of the buffer and backfill.

The models were primarily made to simulate the scale tests. Modelling of the backfill in the deposition tunnel was made with the code 3DEC and modelling of the buffer in the deposition hole was made with Code_Bright. Both models could well simulate the scale tests. A model of the full scale backfill test in Äspö was also made and the results compared to the measurements with good agreement. Continued modelling of the buffer wetting cases until full saturation was also made, with more typical full-scale properties of the pellet filling in the slot between the buffer blocks and the rock, was also made for both wetting cases. The results showed larger swelling in the case of wetting of the lowest part of the deposition hole than in the case of wetting along the entire rock surface.

Some preliminary conclusions regarding desired continuation of the modelling work were also made:

Backfill model: The reasonable agreement of the modelling of the backfill, obtained between modelling results and measurements in both the lab-scale test and the full-scale Buffer swelling test, indicate that 3DEC is a suitable modelling tool for this type of problem. However, more work can be done to improve the general agreement between models and measurements and to test to what extent upscaling results from lab-scale to full scale is possible.

Buffer model: The water supply is a factor which affects the system significantly. Other layouts should be investigated in order to see if there are other wetting situations that produce results which are worse in a safety perspective. A potentially problematical water supply layout is one where water enters around the canister top. In this first stage only smaller scale geometries have been used. In order to have full confidence in that results are valid at full scale (are fully scalable); full scale models should be developed.

Sammanfattning

Ett KBS-3V slutförvar för utbränt kärnbränsle är planerat att byggas i Forsmark. Anläggningen under jord består av tunnlar där åtta meter djupa deponeringshål är borrade i tunnelgolvet var sjätte meter. Bränslet är inkapslat i kopparkapslar, som är placerade i deponeringshålen. Kapslarna är omgivna av högkompakterade buffertblock. Referensdesignen för återfyllning av deponeringstunnlarna innefattar inplacering av kompakterade block i tunnlarna som i sin tur är omgivna av bentonitpellets som fyller upp utrymmet mellan block och tunnelväggar. Pellets kommer också att placeras på tunnelgolvet för att jämna ut den grova bergytan och därigenom skapa ett passande underlag på vilket återfyllningsblocken kan staplas.

En av de viktigaste uppgifterna för återfyllningen är att begränsa buffertens uppsvällning i deponeringshålen mot återfyllningen. När bufferten sväller uppåt tappar den densitet och därmed också viktiga egenskaper. Till exempel kommer svälltrycket att sjunka. Ett möjligt scenario som skulle kunna leda till en stor sådan svällning av bufferten är om vatteninflödet till deponeringstunneln är lågt men att där samtidigt är ett vatteninflöde in till ett deponeringshål. Detta betyder att bufferten i deponeringshålet hydrerar och sväller vilket leder till att ett svälltryck byggs upp som trycker den torra återfyllningen uppåt.

Scenariot med buffert som sväller uppåt mot en torr återfyllning har undersökts tidigare, både genom modellering och genom att ett fullskaligt test är utfört, Buffertuppsvällningsförsöket på Äspö HRL. Modelleringen och undersökningarna har därvid fokuserat på två extrema fall, (1) återfyllningen har varit helt vattenmättad och (2) återfyllningen har varit helt torr, och dessa fall i kombination med en helt vattenmättad buffert som har tillgång till vatten från hela den omgivande bergytan. Huvudanledningen till att fokus har legat på dessa extrema fall har varit brist på kunskap om de mekaniska egenskaperna hos delvis mättade system och en hypotes att torr återfyllning är det mest deformerbara fallet.

Ett nytt projekt avseende dessa frågor initierades för att bättre förstå buffertens uppåtsvällning och den medföljande kompressionen hos återfyllningen vid olika bevätningsscenarier. I detta projekt har ett flertal skalförsök av både deponeringshålet och tunneln gjorts. Modellering av skalförsöken har också varit en viktig del i detta projekt som kommer att ha en fortsättning.

Denna rapport beskriver skalförsök utförda i laboratorium för att undersöka hur buffert och återfyllning beter sig vid olika typer av bevätning. Två skalförsök i skalan 1:10 av ett deponeringshål med olika bevätningsmönster har gjorts. Återfyllningen har i dessa försök simulerats med en kombination av styva fjädrar placerade i toppen på deponeringshålet med ett kraft-deformationssamband som motsvarar motståndet från en torr återfyllning enligt fullskaleförsöket på Äspö. Båda försöken drevs i cirka ett år och åtföljdes av en noggrann provtagning och bestämning av densitet och vattenhalt. Fyra skalförsök i skala 1:20 av en 6 meter lång sektion av en deponeringstunnel ovanför ett deponeringshål har också utförts. En platta i tunnelgolvet simulerade den svällande bufferten genom att tryckas uppåt med samtidig mätning av kraften. Dessa försök drevs med mellan 0 (torrt försök) och 52 dagars bevätning innan start av den simulerade buffertuppsvällningen. Försöken blev sedan noggrant provtagna med mätning av fördelningen av densitet och vattenkvot.

Resultaten från dessa försök har använts för att öka förståelsen när det gäller olika typer av bevätningsscenarier och till att studera möjligheten att skala upp resultaten till full skala. Två viktiga observationer och preliminära slutsatser från dessa försök var:

- Bevätning av bara den understa delen av deponeringshålet (under kapseln) kan orsaka större uppsvällning och större lokal förlust av densitet i bufferten än om bevätningen är jämnt fördelad längs hela bergytan.
- Det torra fallet av tunnelåterfyllning tycks vara det mest kritiska och ge lägst motstånd mot uppåtsvällning än andra bevätningsscenarier.

Parallellt med laboratorieförsöken har nya modeller av både buffert och återfyllningens egenskaper utvecklats eftersom det har bedömts vara nödvändigt för att verifiera och utveckla de nuvarande modellerna så att de kan användas för att beräkna olika bevätningsfall för buffert och återfyllning.

Dessa modeller gjordes huvudsakligen för att simulera skalförsöken. Modelleringen av återfyllningen gjordes med koden 3DEC och modelleringen av deponeringshålet gjordes med Code_Bright. Båda modellerna kunde simulera skalförsöken väl. En modell av det fullskaliga återfyllningsförsöket i Äspö gjordes också med god överensstämmelse mellan mätta och modellerade resultat.

Fortsatt modellering av de två skalförsöken av deponeringshålet till full vattenmättnad gjordes också med egenskaper hos spaltfyllningen som stämmer mer överens med referensutformningen. Resultaten visade att svällningen blev större för fallet med bevätning av bara den undre delen av deponeringshålet än för fallet med bevätning längs hela bergväggen.

Några preliminära slutsatser avseende önskad fortsatt arbete med modelleringen drogs också:

Återfyllningsmodellen: Den hyggliga överensstämmelsen mellan modelleringsresultaten och mätresultaten, både för skalförsöken och det fullskaliga försöket i Äspö, visar att 3DEC är en lämplig kod för att modellera denna typ av problem. Emellertid, kan mer arbete behövas för att ytterligare förbättra överensstämmelsen mellan modell och försök och för att undersöka i vilken utsträckning man kan skala upp resultaten från labbskala till full skala.

Buffertmodellen: Bevätningssituationen är en faktor som påverkar systemet avsevärt. Andra bevätningsfall bör undersökas för att se om det ur säkerhetssynpunkt finns värre buffertuppsvällningsfall. Ett möjligt problematiskt fall är om bevätning sker runt kapseltoppen. Hittills har endast geometrier i labbskalan 1:10 modellerats. För att få full tillit till resultaten bör man även modellera fullskaliga geometrier.

Contents

1 Introduction

1.1 General

A KBS-3V repository for spent nuclear fuel is planned to be built in Forsmark. In this concept, the underground facility consists of tunnels with eight-meter-deep deposition holes bored in the tunnel floor every sixth meter. The fuel is encapsulated in copper canisters, which are placed in the deposition holes. The canisters are surrounded by highly compacted buffer blocks. The reference design for backfilling of the deposition tunnels is pre-compacted blocks placed in the tunnel and bentonite pellets that fill up the space between the blocks and the tunnel walls. Pellets will also be placed on the tunnel floor in order to even out the rough rock surface and by that provide a suitable surface on which the backfill blocks can be piled. Figure 1-1 shows a schematic drawing of the reference design.

One of the most important tasks for the backfill is to restrict upwards swelling of the buffer from the deposition holes. If the buffer can swell upwards it will lose density and by that also important properties e.g. a decrease in swelling pressure. A possible scenario that could lead to such expansion of the buffer is when the water inflow rate into the deposition tunnel is very low but at the same time there is a substantial water inflow into a deposition hole. This could lead to that the buffer in the deposition hole hydrates and swells when the backfill is still dry, which results in a pressure build up that will push the dry backfill upwards. The backfill blocks will be piled according to a predefined pattern, which leads to an improved distribution of the restricting load (i.e., it is not only the self-weight of the directly overlying backfill blocks that is restricting the movements but also adjacent interlocked blocks). The slots between the backfill blocks and the rock will be filled with bentonite pellets and the compression properties of this filling at the floor and the roof will strongly influence the ability of the backfill to resist heaving of the buffer.

The scenario with buffer swelling upwards against a dry backfill has been investigated earlier, both by modelling e.g. in Börgesson and Hernelind (2014, 2017) and by performing a full-scale test, the Buffer Swelling Test at Äspö HRL (Sandén et al. 2017). The full-scale test simulated a completely dry deposition tunnel where the backfill was compressed by a swelling buffer (hydraulic jacks were used to simulate the swelling bentonite).

The previous modelling and investigations were focused on the two extreme cases, (1) the backfill has been fully water saturated or (2) the backfill has been completely dry, and this in combination with a fully water saturated buffer that has access to water in the entire rock buffer interface. The main reason for focusing on these extremes was lack of knowledge of the mechanical properties of partly water saturated systems and a belief that the dry backfill was the worst case.

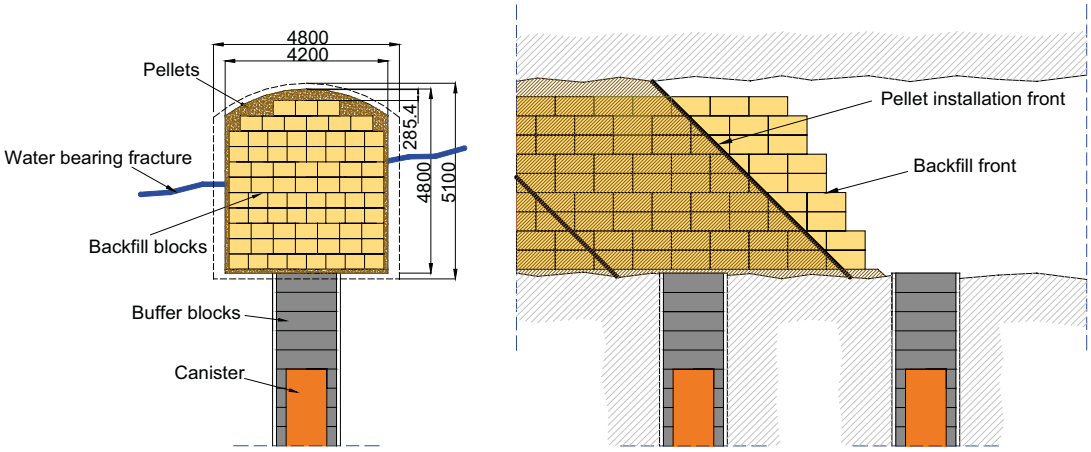

Figure 1-1. *Schematic drawing showing the reference design for backfill considered by SKB.*

However, since cracking occurred in the blocks in the backfill in the field test, and the cracking resulted in very low resistance against upwards swelling, it has been judged of high importance to also investigate cases where the backfill has been partly saturated and backfill blocks possibly has cracked due to the wetting. Another concern is that actual modelling of the buffer water uptake may result in a different behaviour than for the simplified case where full saturation is prescribed from start. Previous modelling has for instance shown that the resulting upwards swelling force becomes higher if initial block and pellet filling densities are represented as compared to a model where a fully homogenized buffer is used from start.

In order to better understand the upwards swelling of the buffer and subsequent compression of the backfill at different wetting scenarios several scale tests of both the deposition hole and the tunnel have been performed. Modelling of these cases has also been an important part of this investigation.

1.2 Objectives

This report is focused on presenting the experimental design and the results of the scale tests of the buffer and the backfill and the modelling of those tests. The tests and the modelling have led to very interesting results and some analyses and comparisons will also be done but additional deeper analyses of all results will be performed in the next step of the project.

1.2.1 Scale tests

An important part of the investigation has been to perform scale tests in the laboratory with the objective to better understand the behaviour of the buffer and the backfill at different wetting scenarios. The results from the tests will be used to:

- Increase the understanding regarding which wetting scenarios that gives the largest buffer swelling.
- Compare the results with different models.
- Scale the results up to full scale.

To streamline the scale tests, the buffer swelling from the deposition hole and the compression of the backfill have been tested separately in different test equipment.

1.2.2 Modelling

The objective of the modelling is to verify and develop the existing modelling tools so that they can be used for calculations of different wetting scenarios of buffer and backfill.

Since it is likely that the modelling tools are insufficient to yield results with very high accuracy the laboratory tests can be used for comparison and increase of confidence of the predictions by upscaling the model results.

1.3 Requirements

There are several technical design requirements on the buffer and on the backfill specified in Posiva SKB (2017) e.g. regarding the dry density yielding a certain swelling pressure, hydraulic conductivity and shear strength.

This report concerns investigations regarding the deformation properties of the backfill and the upwards swelling of the buffer at different wetting scenarios. The deformation properties of the backfill will have an impact on the technical design requirement specified in Posiva SKB (2017):

"*The overall deformation of the installed backfill both in dry and saturated state shall resist the swelling pressure from the buffer and maintain the buffer swelling pressure > 3 MPa in average over the buffer volume*". The buffer volume extends from the bottom of the deposition hole to a distance of 500 mm above the canister.

One of the main objectives with the investigation has thus been to investigate if this requirement can be fulfilled regardless of which wetting scenario that arises for either the backfill or the buffer.

2 Reference designs

2.1 General

The performed scale tests are designed based on the present reference design for deposition tunnels including the backfill and the deposition holes including the buffer. The reference designs of these are, however, updated continuously and changes may influence the results and the conclusions drawn in this report.

2.2 Reference design of backfill

A detailed description of the reference design for backfill, can be found in SKB (2010a, b). The reference design described in these reports was the same as was used for the application for the construction of a final repository. The design has, however, later been further developed within a SKB project (Arvidsson et al. 2015) regarding e.g. the backfill block dimensions, the block stack dimensions and the stacking pattern but also regarding the installation technique.

2.2.1 Deposition tunnel

A schematic drawing showing the updated reference design of an SKB deposition tunnel is provided in Figure 2-1. The accepted volume exceeding the nominal (19.1 m^2) is 0.30 × $A_{nominal}$ × $L_{blasting}$ round m^3. The accepted largest cross-section area exceeding the nominal is 0.35 × $A_{nominal}$ m^2. The drawing shows both the nominal tunnel geometry and a supposed over break.

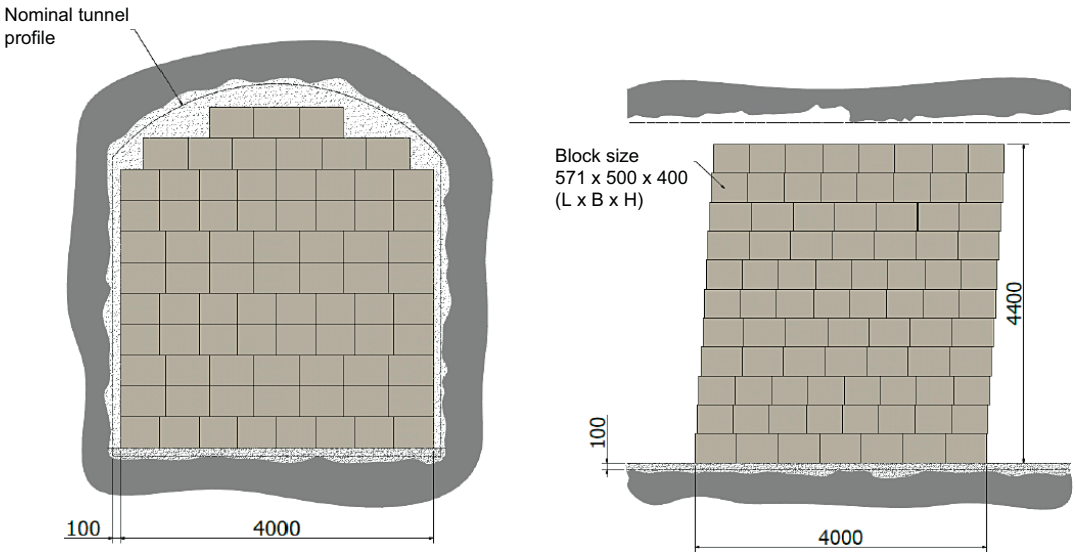

Figure 2-1. *Reference design of the deposition tunnels. The size of the backfill blocks and the block stack pattern is optimized to the tunnel profile.*

2.2.2 Backfill

Backfill blocks

The reference design for the backfill blocks is described in SKB (2010b). Important requirements are e.g. that the raw bentonite should have a montmorillonite content of 50–60 % (accepted variation of 45–90 %) and that the blocks should have a dry density of 1 700 kg/m^3 (accepted variation ± 50 kg/m^3).

The backfill reference design was later updated (Arvidsson et al. 2015). In the updated reference design, the backfill block dimensions are changed to 571 × 500 × 400 mm and this block size was also used in the Buffer Swelling test performed at Äspö HRL (Sandén et al. 2017).

Backfill block stack

The updated backfill reference design includes a new stacking pattern with overlapping blocks (Arvidsson et al. 2015), Figure 2-1. The block stack has a width of 4 000 mm and a height of 4 400 mm. The nominal block volume is 16.5 m^3/m tunnel which should be compared with the nominal tunnel area which is 19 m^2. With an average amount of overbreak of 16 %, the block filling degree will be approximately 75 %.

2.3 Reference design of buffer

A detailed description of the reference design of the buffer can be found in SKB (2010a, c). The reference design described in these reports was the same as was used for the application for the construction of a final repository. An update of the design has later been made, see schematic drawing provided in Figure 2-2.

2.3.1 Deposition hole

The nominal diameter of a deposition hole is 1 750 mm and it has a depth of approximately 7 930 mm (in the updated design). It should be noted that the uppermost meter of the deposition hole is regarded as a part of the backfill but has in these tests been included as buffer, since it was judged that it will affect the buffer swelling properties. The bevel, positioned in uppermost part of the deposition hole in the reference design, has not been included in the scale tests.

2.3.2 Buffer

A schematic drawing showing the new reference design of the buffer is provided in Figure 2-2. The buffer consists of ring-shaped blocks, solid blocks and pellets. A compilation of the most important data for these three components is provided in Table 2-1.

Table 2-1. Reference design of buffer blocks and pellets.

Design parameter	Nominal design	Accepted variation
Solid blocks		
Bulk density, kg/m^3	1 987	± 20
Water content, %	17	
Height, mm	540	± 1
Diameter, mm	1 650	± 1
Ring-shaped blocks		
Bulk density, kg/m^3	2 057	± 20
Water content, %	17	± 1
Height, mm	477	± 1
Diameter, mm	1 650	± 1
Pellets		
Bulk density (loose filling), kg/m^3	1 035	± 40
Water content, %	15	± 1
Dimensions, mm	16 x 16 x 8	

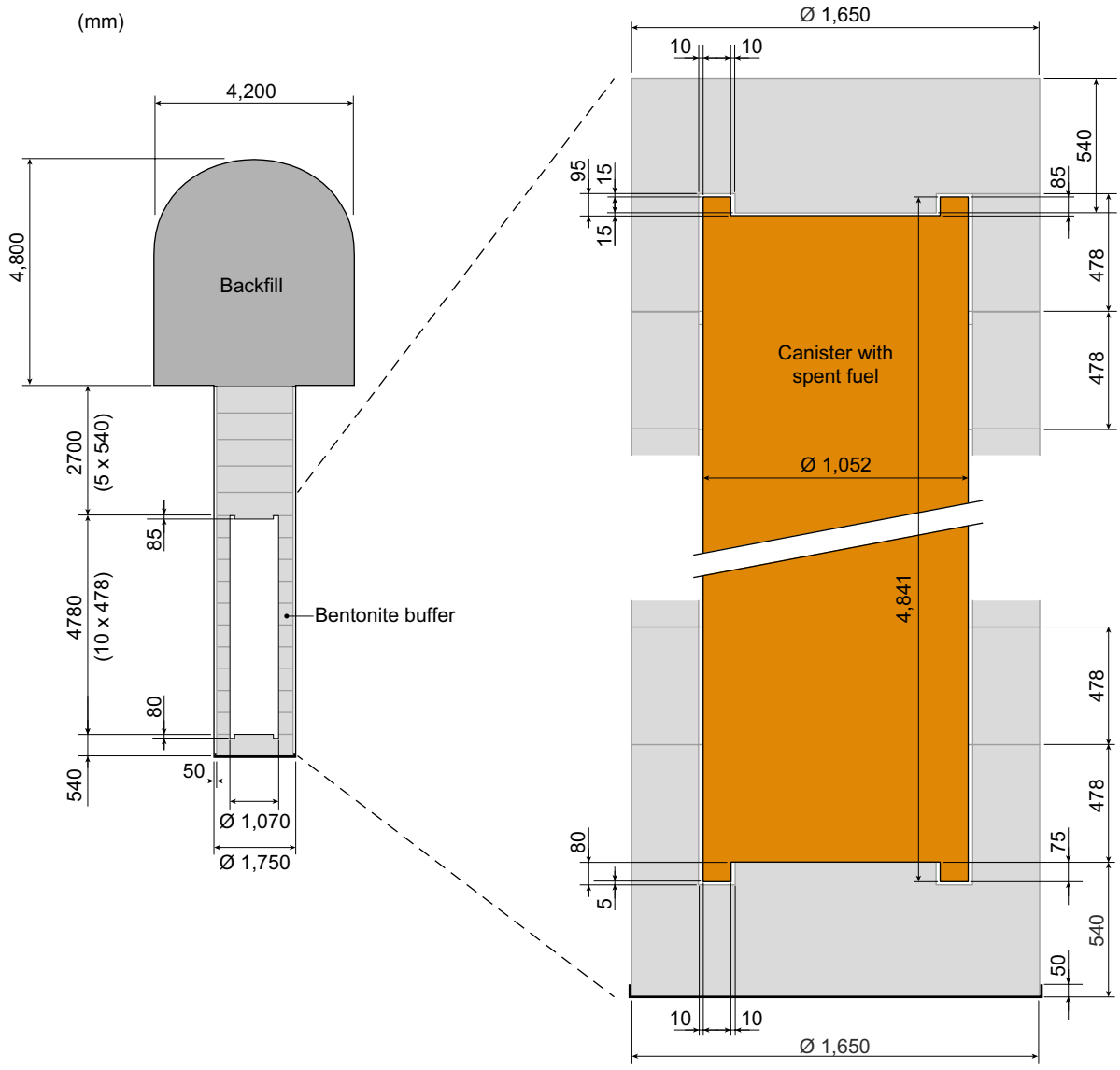

Figure 2-2. *The updated reference geometry of the installed buffer and the nominal dimensions of a deposition hole.*

2.4 Changes in the reference design

The reference designs for buffer and backfill are continuously updated. Investigations are e.g. ongoing regarding the possibility to use buffer blocks consisting of several minor block pieces. It should be noted that any changes in the design may influence the results and the conclusions drawn in this report, see e.g. Section 11.2 regarding new tunnel profiles that are suggested.

3 Deposition tunnel tests in scale 1:20

3.1 General

One of the most important properties of the backfill is to restrict the buffer expansion/swelling upwards into the deposition tunnel. Tests were performed in scale 1:20 where the resistance of the backfill to limit the buffer swelling has been investigated. The buffer swelling has been simulated by pressing a piston upwards from the tunnel floor. This was made by placing the complete test equipment in a hydraulic press. The investigated test conditions were varied from a completely dry backfill to an almost completely saturated and homogenized backfill.

3.2 Test equipment

The test tunnel is built in steel, Figure 3-1. Five stiffeners are welded to the outer periphery to prevent strains of the test tunnel during the test. Steel lids are bolted to the tunnel at both ends. To control the water saturation, filters are positioned on the ceiling, the walls and on the floor. The filters have a thickness of 2 mm and are made of plastic. In total ten water inlets/outlets are connected to the filters. No filters are placed on the tunnel ends.

The deposition hole is simulated by a steel tube mounted below the floor. A piston that can be pushed upwards is simulating the upward swelling of the buffer. The simulated upwards buffer swelling is done by placing the test equipment in a hydraulic press, see description in Section 3.5. The applied load on the piston is registered by a load cell and the displacement is registered by a strain gauge positioned on the press.

3.2.1 Scaling

The cross-section of the test tunnel was built in scale 1:20 according to the current reference design for a deposition tunnel, Figure 3-1. The chosen dimensions are mean values of the nominal dimensions and the dimensions at an overbreak of 22 % (evenly distributed around the tunnel periphery), see data on the dimensions used provided in Table 3-1. The length of the test tunnel is 300 mm which in this scale means that the distances between the centre of the deposition hole to the tunnel ends are 150 mm i.e., the half distance between two deposition holes in this scale.

Table 3-1. Compilation of dimensions used to calculate the size of the scale test.

Tunnel	Nominal mm	Maximum mm	Average mm	Scale test mm
Width	4 200	4 800	4 500	**225**
Wall height	4 050	4 400	4 218	**211**
Total height	4 800	5 100	4 950	**248**

The test tunnel has a cross-section area of 0.053 m^2 which is approximately 400 times smaller than a tunnel with the average dimensions given in Table 3-1 (21.05 m^2).

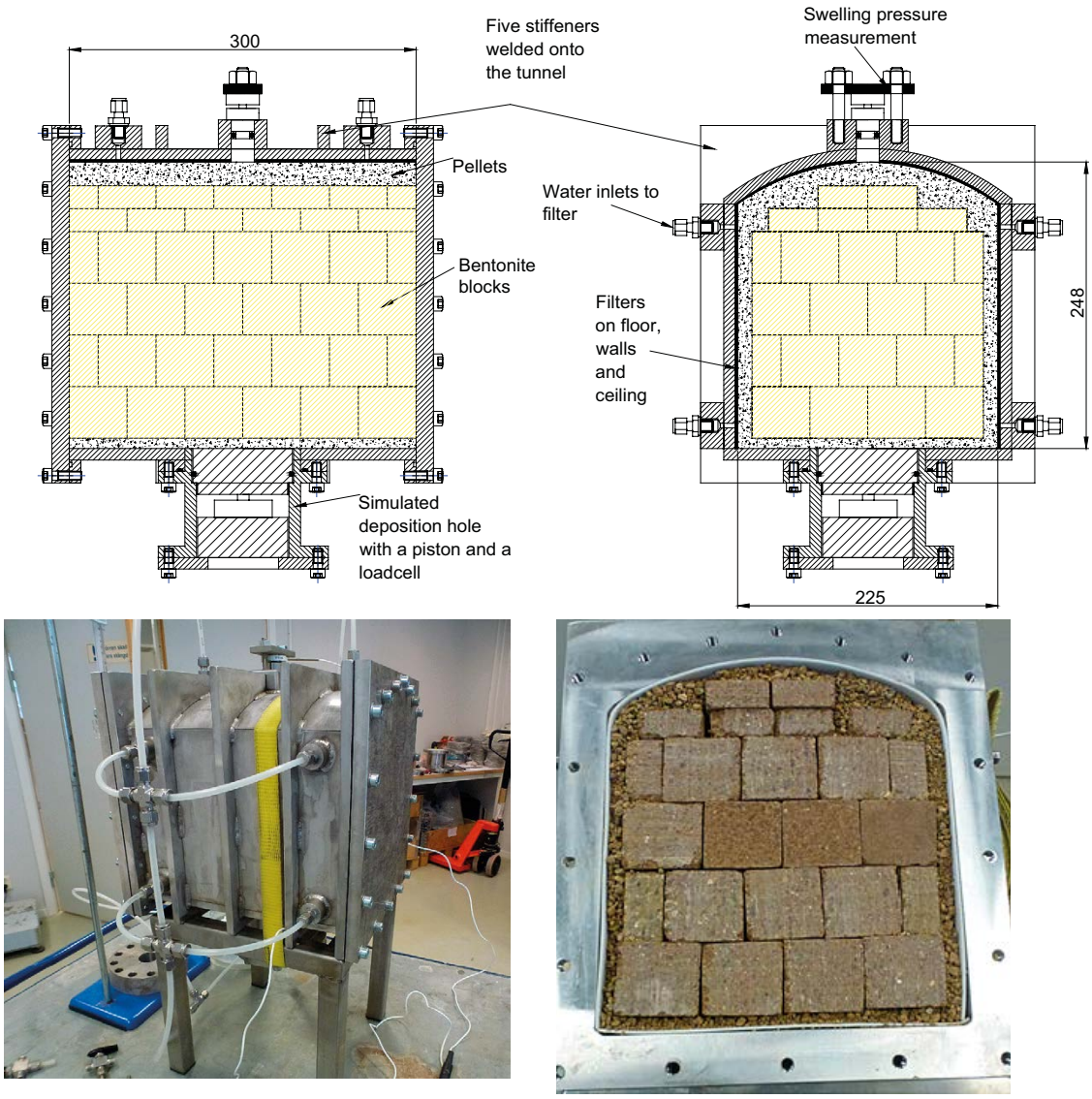

Figure 3-1. *Upper: Schematic drawing of the test equipment. Lower left: The complete test equipment after preparation. Lower right: Photo showing a cross-section at one of the tunnel ends. The photo is taken after preparation of a new test.Figure 3-1. Upper: Schematic drawing of the test equipment. Lower left: The complete test equipment after preparation. Lower right: Photo showing a cross-section at one of the tunnel ends. The photo is taken after preparation of a new test.*

3.3 Material

3.3.1 Bentonite

The backfill blocks were manufactured of Asha NWL-L bentonite from a batch delivered to SKB 2012. This material is produced by Ashapura Minechem Co, India. The bentonite is sodium dominated with a montmorillonite content of about 70 %. The material has earlier been investigated:

1. The Asha bentonite was included in a laboratory investigation of different backfill materials (Sandén et al. 2014).
2. Backfill blocks in full scale were produced and investigated (Sandén et al. 2016). One conclusion from this investigation was that the block quality increased when the water content was adjusted to about 20 %.

3.3.2 Backfill block manufacturing

Based on the results from earlier investigations the water content of the raw material was adjusted from 16–17 % to 20 % before compaction. The backfill block manufacturing was made by compacting cylindrical blocks with a diameter of 175 mm and a height of 50 mm, which then were sawed into backfill blocks with the desired dimensions, see below.

The deposition tunnel and the outer dimensions of the block stack were scaled to 1:20, but for practical reasons it was decided to scale the individual block size to approximately 1:10 (in total 156 blocks in one test setup instead of 1 248).

Two block sizes were manufactured, Figure 3-2 (see also schematic drawing in Figure 3-1):

1. Block to the four first layers. These blocks had the dimensions 50 × 50 × 45 mm.
2. Blocks to the two uppermost layers. These blocks had the dimensions 20 × 43 × 45 mm.

The backfill blocks used in the test had a bulk density of 2 064 kg/m^3 and a dry density of 1 720 kg/m^3. The water content was 20 %.

3.3.3 Backfill pellets

The backfill pellets are difficult to scale. It was therefore decided to use granules sieved out from the raw materials as pellets filling in the outer slot. The granules had a size between 1 to 6 mm. The compression properties of the simulated pellet filling were determined by performing a test in the laboratory, see Chapter 4.

3.3.4 Water

The water used in the test had a salinity of 1 % by weight (50/50, Na/Ca).

Figure 3-2. *Photo showing the two block types.*

3.4 Test matrix

In total four tests were performed within this investigation, Table 3-2. The main test parameter varied was the wetting time of the backfill after installation. The first test was performed without any access to water at all i.e., the backfill properties were tested as installed. In the two following tests, Test 2 and Test 3, the backfill was tested after different wetting times. Originally, one additional test with longer wetting time was planned, but due to the results from the early tests (Test 1 to Test 3), it was later decided to instead perform a different test where the access to inflowing water was limited (Test 4).

Table 3-2. Test matrix for the deposition tunnel tests performed in scale 1:20.

Test no.	Wetting time	Water pressure	Remarks
Test 1	0 days	na	Dry backfill
Test 2	52 days	10 kPa	
Test 3	8 days	10 kPa	
Test 4	7 days	0 kPa	Limited access to water (1 liter)

3.5 Implementation

The test procedure can be divided into several different activities. These activities were almost the same for all four tests performed in this test series.

3.5.1 Preparation of the test tunnel

The preparation of the test equipment consisted of the following steps:

1. One of the steel lids (tunnel ends) was mounted on the test cell.
2. Installation of filter mats in the simulated tunnel.
3. The simulated deposition hole was mounted on the tunnel section together with piston (simulating buffer) and load cell.
4. The piston measuring the swelling pressure at the ceiling was mounted.

3.5.2 Installation of block and pellets in the test tunnel

The installation of the backfill started with the bottom bed of the pellets that were spread to an evenly layer on the floor. The blocks were thereafter stacked manually, and gradually pellets were installed in the gaps between the block stack and the simulated tunnel walls, Figure 3-1 and Figure 3-3. The last pellets were installed after leaning the tunnel, see right photo in Figure 3-3. After installation of all bentonite, the last steel lid (tunnel end) was mounted.

3.5.3 Water saturation phase

Tubes were connected to all water inlets (Test 2, Test 3 and Test 4), which in turn had connection to the filter mats. The tube ends were then connected to one tube feeding the whole test with water.

Water was filled up from the bottom of the tunnel. When the initial filling was ready (tubes, filters and parts of the pellet filling were filled with water) the single feeding tube was connected to a burette. The water uptake was thereafter measured continuously during the saturation phase.

3.5.4 Compression of backfill – simulation of the buffer swelling

After finishing the water saturation phase (if any), the complete test equipment was placed in a hydraulic press, Figure 3-4. The piston in the simulated deposition hole was pushed upwards into the backfill at a constant rate of 0.05 mm/min. The force from the simulated deposition hole and the displacement were registered continuously. The stress at the ceiling above the deposition hole was also registered, Figure 3-1. The maximum allowed pressure from the simulated deposition hole was set to 5 MPa.

Figure 3-3. *Photos taken during the installation of the backfill in the simulated deposition tunnel.*

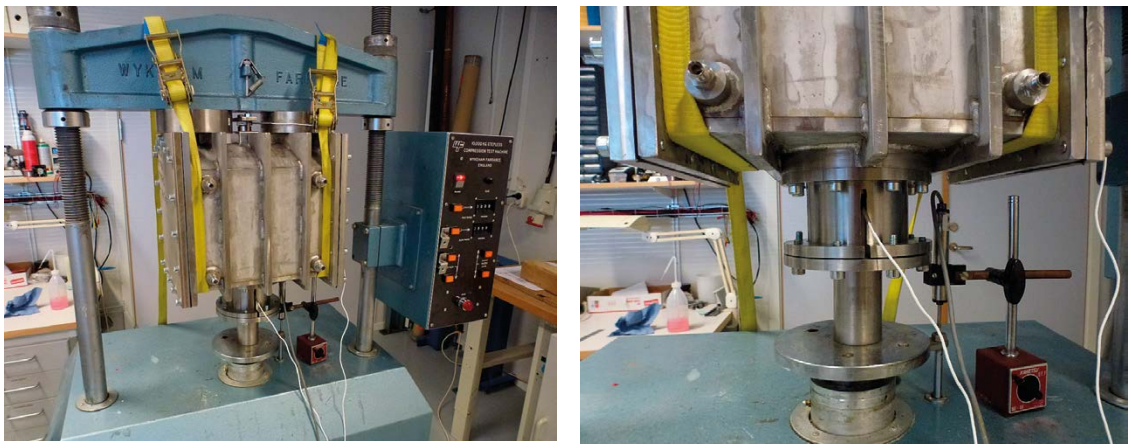

Figure 3-4. *Left: The complete test equipment is placed in a hydraulic press. Right: Close-up of the simulated deposition hole.*

3.5.5 Dismantling and sampling

After reaching 5 MPa pressure on the piston the tests were dismantled. Samples were cut or sawed out at 63 positions in three different cross-sections, Figure 3-5, i.e., in total 189 samples (Test 2 and Test 3). The water content and the density were determined at every position.

Test 1 was a dry test and no sampling was made on this test. Test 4 had a limited wetting and thereby also a limited sampling since large parts of the installed backfill was unaffected by the injected water.

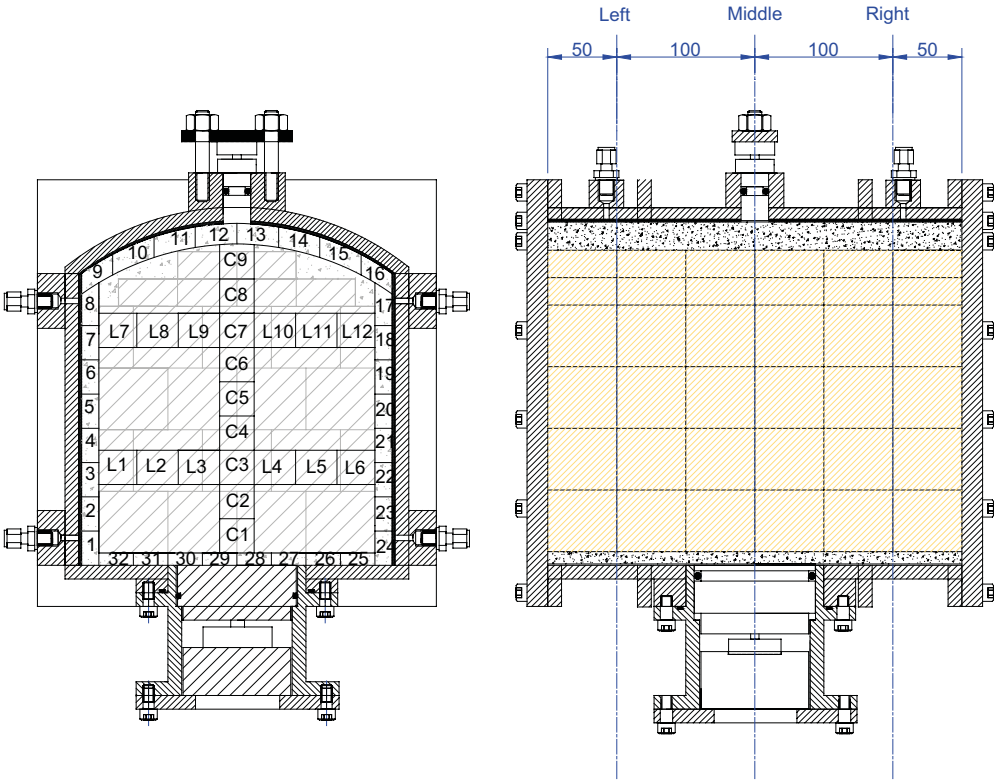

Figure 3-5. *Left: Cross-section of the simulated tunnel showing the positions of all samples. Right: The sampling was made at three cross-sections.*

3.6 Results

The results from all four tunnel tests are presented in this chapter. In order to facilitate the comparison between the different tests, the results are presented in parallel for all tests.

3.6.1 Preparation

In conjunction with the installation of bentonite blocks and pellets in the test cell, all material was weighed. Table 3-3 shows the determined dry density of the components and also the average dry density in the test cell. With this data it was possible to calculate the saturated density and the amount of water needed to reach saturation.

As shown in the table, the installed density of both blocks and pellets were similar for all four tests.

Table 3-3. Table showing the installed dry density of the different components, the calculated saturated density and the water needed to reach saturation for all four tests.

Test	Bentonite installation, dry density			Test phase	
	Block stack kg/m³	Pellets kg/m³	Average kg/m³	Water for saturation liters	Saturated density kg/m³
1	1655	826	1469	2.94	1943
2	1655	791	1462	3.01	1938
3	1668	791	1472	2.92	1944
4	1675	796	1478	2.86	1948

3.6.2 Water uptake

The first tunnel test, Test 1, was simulating a dry backfill and the last test, Test 4, was simulating limited access to water i.e., about one liter was injected and then the backfill had no further access to water. However, two of the four performed tunnel tests had unlimited access to water via the filter mats during a certain time, Test 2 and Test 3. The measured accumulated water uptake for these two tests is presented in Figure 3-6. The amount of water needed to reach complete saturation was calculated to 3.01 (Test 2) and 2.92 (Test 3) liters respectively. As shown in the graph, about 1.75 liters were injected during the test start in both tests. After this first phase, the water uptake clearly decreases with time. In total 2.4 liters were injected in Test 3 for eight days and in Test 2 almost 2.8 liters were injected during 52 days.

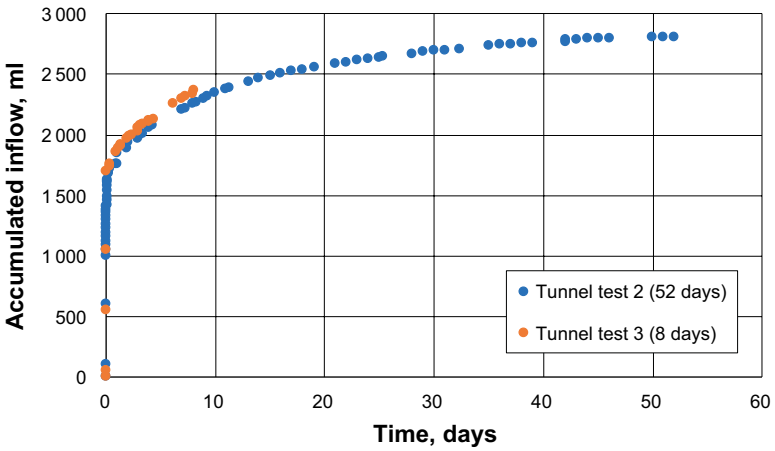

Figure 3-6. *The accumulated water inflow plotted versus time for the two tests that have had unlimited access to water during a decided time (Test 2 and Test 3).*

3.6.3 Swelling pressure development

The swelling pressure development for the three tests that had access to water (Test 2 and Test 3 during different times and Test 4 with a limited amount of water) is presented in Figure 3-7. As shown in the graphs, the behaviour is similar for Test 2 and Test 3 during the first eight days i.e., the test duration of Test 3. In Test 2, the swelling pressure continues to increase with time and has after 52 days reached between 1 100 to 1 200 kPa. The registered swelling pressure in Test 4 is below 100 kPa after seven days test and there is no tendency that it should increase. This depends clearly on the limited access to additional water after the first filling of one liter.

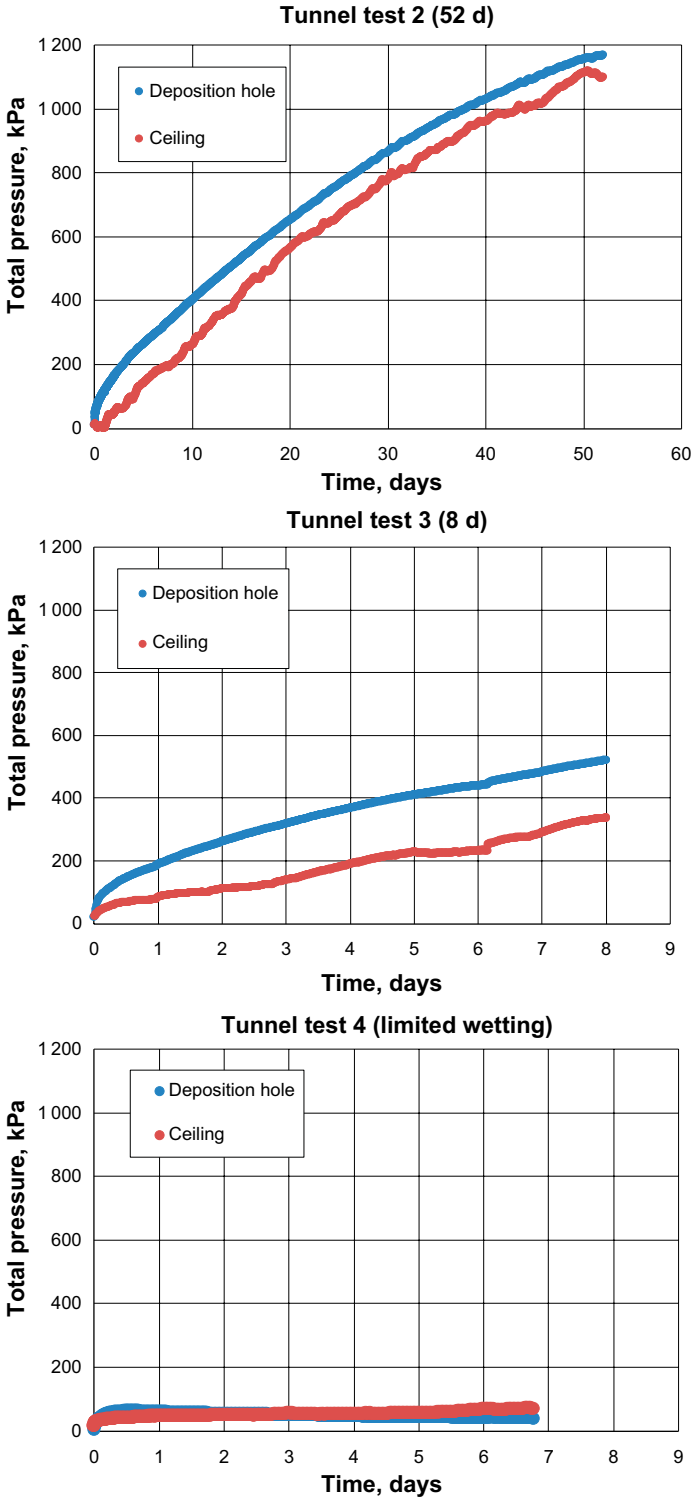

Figure 3-7. Total pressure plotted versus time for the three tunnel tests that have had access to water. Upper: The 52-day test. Middle: The 8-day test. Lower: The test with limited access to water.

3.6.4 Compression tests

After having finished the water saturation phase (Test 2, Test 3 and Test 4), and before the dismantling, the compression test simulating a swelling buffer from the deposition hole was performed on all four tests. The results from the compression tests are provided in Figure 3-8.

The simulated buffer, a steel piston, was pushed upwards into the backfill at a constant rate of 0.05 mm/min, see photos provided in Figure 3-4. The force from the simulated deposition hole and the displacement were registered continuously. The maximum pressure from the simulated deposition hole was set to 5 MPa.

As shown in the graphs, the registered displacement for the dry test, Test 1, was almost 14 mm before reaching the maximum stress of 5 MPa. This displacement was considerably more than for the other tests that have had access to water. The least displacement during compression, about 6 mm, was noted for Test 2. This was also the test that has had access to water for the longest time.

In Test 1, it was noted that the backfill blocks seemed to fail and reach their maximum strength just below 5 MPa, see blue line for Test 1.

The measured stress at the ceiling was clearly lower than at the piston for all four tests. This reduction in stress is caused by stress spreading due to the interlocking of the blocks and the friction between the backfill and the steel walls but also on internal friction in the block stack. The reason for the very low stress at the ceiling in test 4 (200 kPa) is not clear.

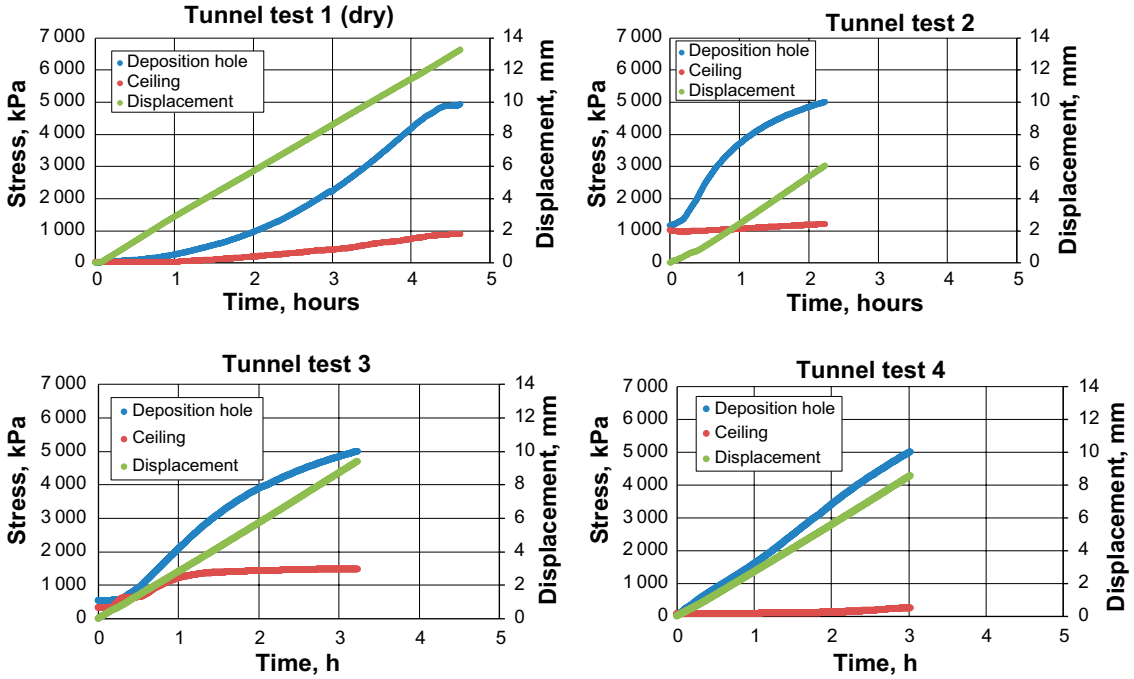

Figure 3-8. *Graphs showing the registered stresses from the deposition hole and at the ceiling together with displacement plotted versus time for all four tests.*

A compilation of the results from all tests are provided in Figure 3-9. The graph shows the registered stress from the simulated buffer plotted versus displacement.

As shown in the graph, it is obvious that the worst case regarding large displacements is when the backfill is dry. A minor wetting of the backfill, see Test 3 and Test 4, clearly increase the stiffness of the backfill and when the backfill is close to saturation, Test 2, the stiffness increases additionally.

3.6.5 Comparison with full scale

In conjunction with a backfill installation test performed at Äspö HRL, a full-scale test on Buffer Swelling was performed (Sandén et al. 2017). Due to low strength of the backfill blocks that were used in this test, it was only possible to reach a simulated swelling pressure from buffer of 1.8 MPa. In Figure 3-10 the stress for all laboratory tests are plotted versus strain. In addition, the results from the field test are added. In the field test, the stress was applied in steps which explain the appearance of the curve. Strain is calculated as the displacement divided to the height of the tunnel.

In the field test there was an applied load on the buffer at the test start of 150 kPa originating from the overload of the block stack. If the same start value is used also for the dry test performed in laboratory, Test 1, by sliding the curve about 1 % strain, the relation between stress and strain becomes very similar to the one from the field test (see red dotted line in the graph). In addition, the relative thickness of the pellets in the bottom bed was 2 times thicker in the scale tests than in the field test. If that is considered, the agreement will be even better.

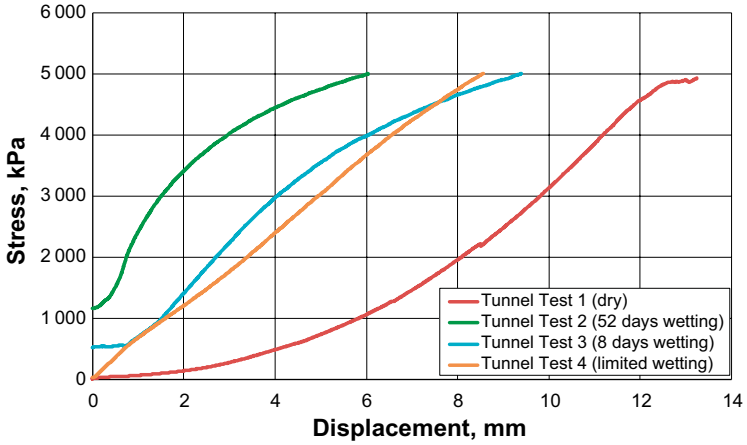

Figure 3-9. *The registered stress plotted versus displacement for all four tests.*

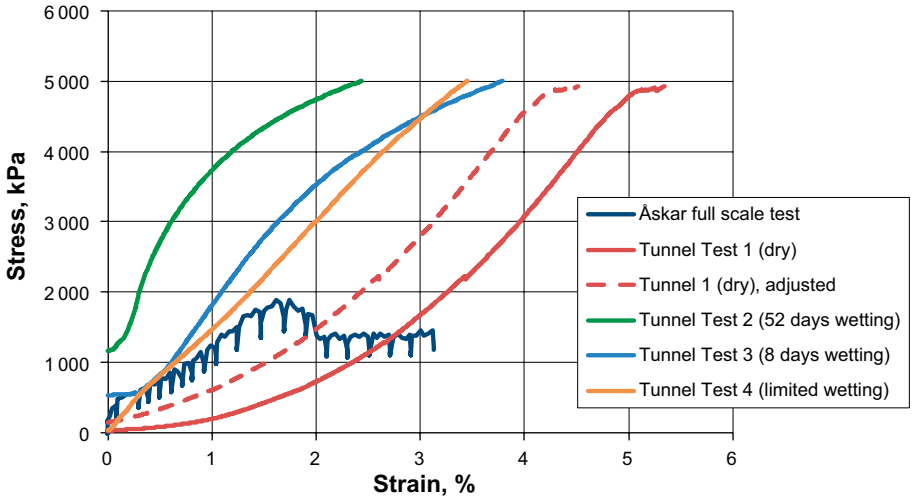

Figure 3-10. *Stress plotted versus strain for laboratory tests and the field test.*

3.6.6 Dismantling

Dismantling of Test 1 (dry backfill)

Photos taken during the dismantling of Test 1 (the dry test) are provided in Figure 3-11. As shown on the photos, the pellet layer on the floor had been compacted above the deposition hole. The blocks above the deposition hole were clearly moved upwards and this movement was also influencing large parts of the block stack.

Figure 3-11. *Upper left: The block stack is clearly affected of the simulated swelling buffer. Upper right: Some of the blocks close to the deposition hole had cracked. Lower left: The pellet filling on the floor had been compressed. Lower right: The top of the simulated deposition hole.*

Dismantling of Test 2 (52 days wetting)

Photos taken during the dismantling of Test 2 (52 days wetting) are provided in Figure 3-12. The complete backfill specimen was pushed out from the test cell using a hydraulic piston. Visually, all backfill seemed to be close to saturation, see also results from the sampling in Section 3.6.7. Despite the high degree of saturation, fractures occurred along the former block boundaries during the sawing. As shown on the photo provided in Figure 3-12 (lower right), the filter above the simulated deposition hole has been pushed into the former pellet filling at the floor.

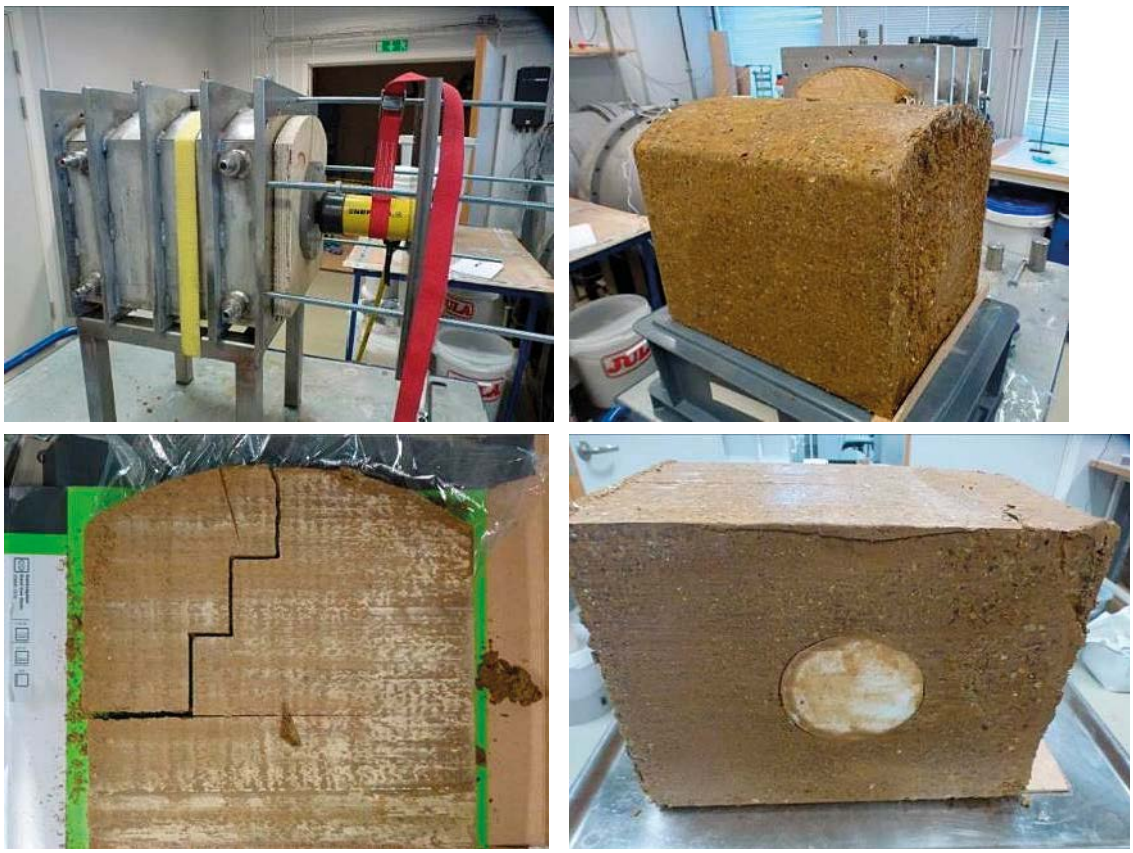

Figure 3-12. *Upper left: The backfill was pressed out from the steel tunnel with a hydraulic piston. Upper right: The complete backfill section. Lower left: During sampling it was observed that the backfill cracked along the former block surfaces. Lower right: Photo showing the backfill section from below. The white filter was positioned above the deposition hole but had been pushed into the pellet filling.*

Dismantling of Test 3 (8 days wetting)

Photos taken during the dismantling of Test 3 (8 days wetting) are provided in Figure 3-13. The complete backfill specimen was pushed out from the test cell using a hydraulic piston (the same technique as was used for Test 2). The outer periphery i.e., the former pellet filling and parts of the block stack were clearly wetted while the innermost parts of the block stack seemed to be almost unaffected of the water uptake. As shown on the photo provided in Figure 3-13 (lower left), the filter above the simulated deposition hole has been pushed into the former pellet filling at the floor (the same as observed for Test 2).

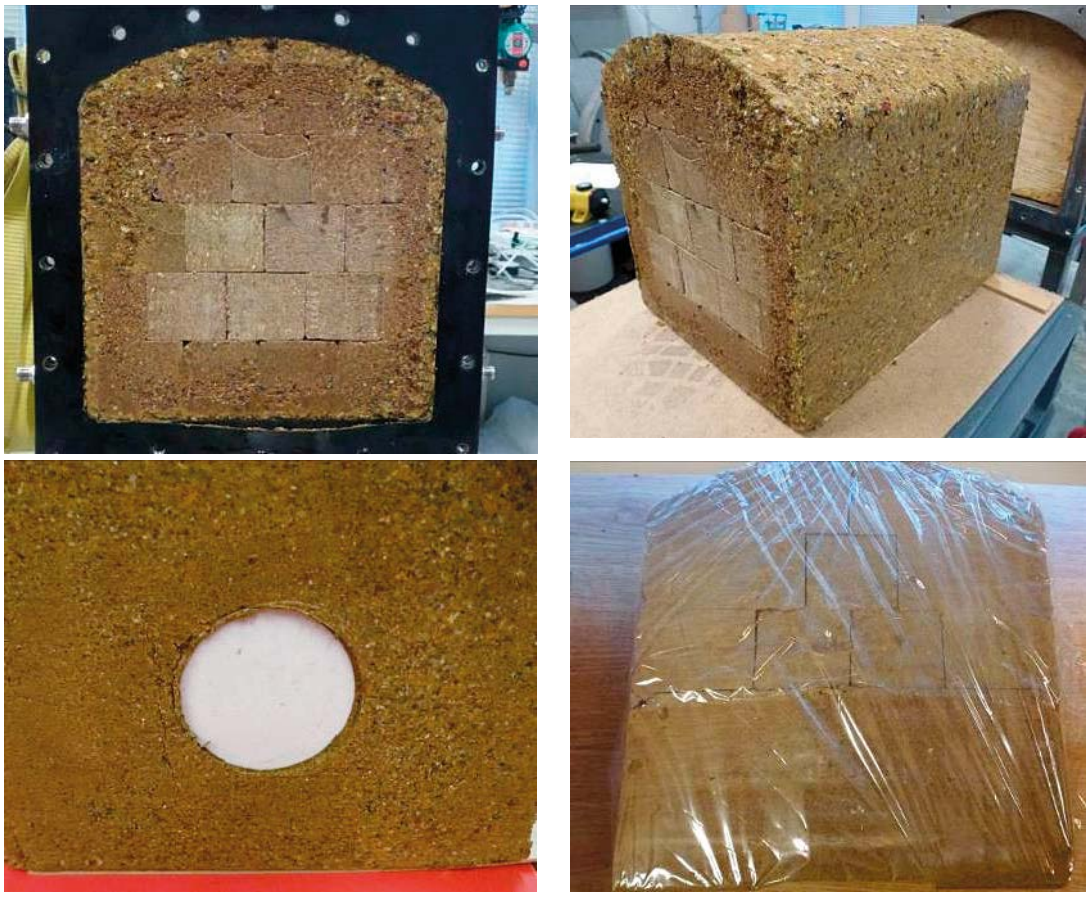

Figure 3-13. *Upper left: There are still dry sections in the middle of the backfill. Upper right: The complete backfill section has been pressed out from the steel tunnel. Lower left: The filter positioned at the top of the deposition hole has been pressed into the backfill. Lower right: Cracks occur along the block surfaces.*

Dismantling of Test 4 (7 days with a limited amount of water)

Photos taken during the dismantling of Test 4 (7 days with a limited amount of water) are provided in Figure 3-14. The complete backfill specimen was pushed out from the test cell using a hydraulic piston (the same technique as was used for Test 2 and Test 3). The main part of the outer periphery i.e., the former pellet filling was wetted, except for the part that had been close to the ceiling. The block stack seemed, however, to be almost unaffected of the water uptake. The simulated buffer swelling had resulted in a local displacement of the blocks above the deposition hole, see photo provided in Figure 3-14 (lower right).

3.6.7 Sampling

The tests were after dismantling sampled according to the plan provided in Figure 3-5 (Test 2 and Test 3). Test 1 was a dry test and no sampling was made on this test. Test 4 had a limited wetting and thereby also a limited sampling since large parts of the installed backfill was unaffected of the injected water. The water content and the density were determined at every position. An interpolation program was used to provide contour plots. Parts of the results from the sampling are provided in Figure 3-15 to Figure 3-17. The black dots represent the actual measuring points while everything in between is interpolated. The graphs show the results from the sampling of the mid-sections. The dry density and degree of saturation are missing for test 4 since the backfill was too dry in order to be able to determine the dry density. All results from the sampling are provided in Appendix 1 to 3.

Figure 3-14. *Upper left: It is mainly the pellet filling that has been affected by the limited water volume. Upper right: The complete backfill section has been removed from the steel tunnel. Lower left: The block stack is clearly affected of the simulated swelling buffer. Lower right: The top of the simulated deposition hole.*

Figure 3-15 shows the water content distribution determined in the middle section of Test 2, Test 3 and Test 4. The differences in wetting observed during dismantling, see photos provided in Figure 3-12 to Figure 3-14, can clearly be seen also in the contour plots.

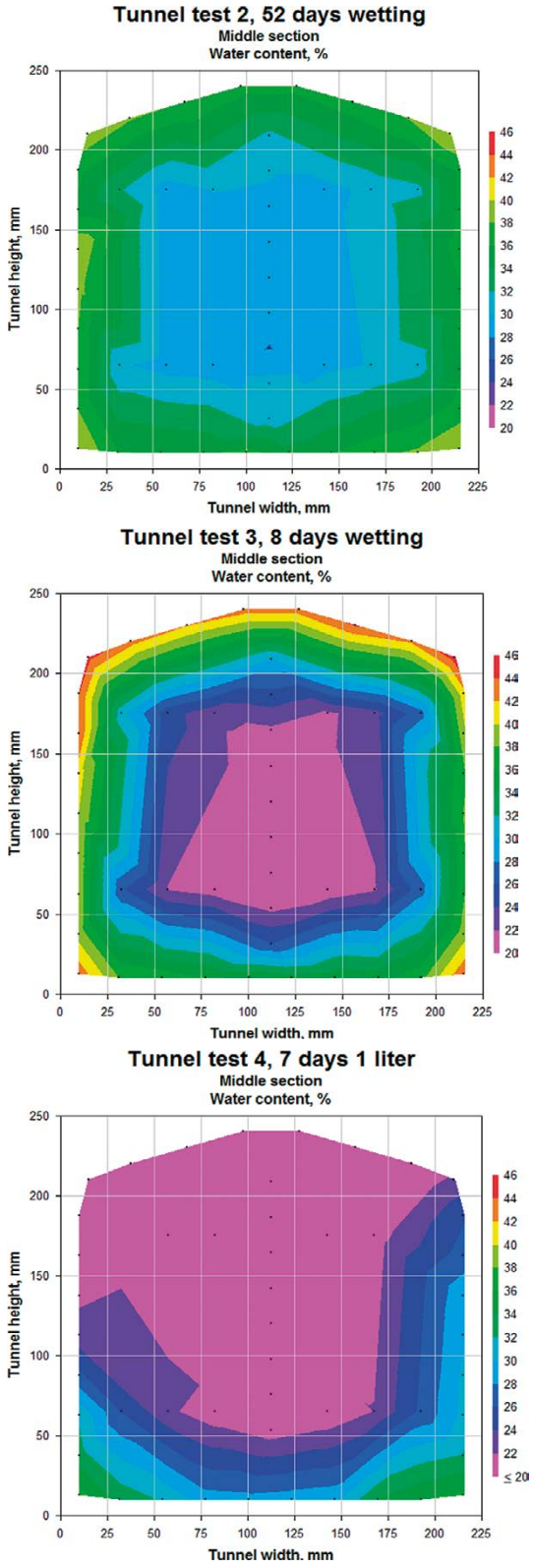

Figure 3-15. *Water content distribution in the mid cross-sections of Test 2 (upper), Test 3 (middle) and Test 4 (lower).*

Figure 3-16 shows the dry density distribution in Test 2 and Test 3. It is obvious that the homogenization has proceeded longer in Test 2 (52 days wetting) compared to Test 3 (8 days wetting).

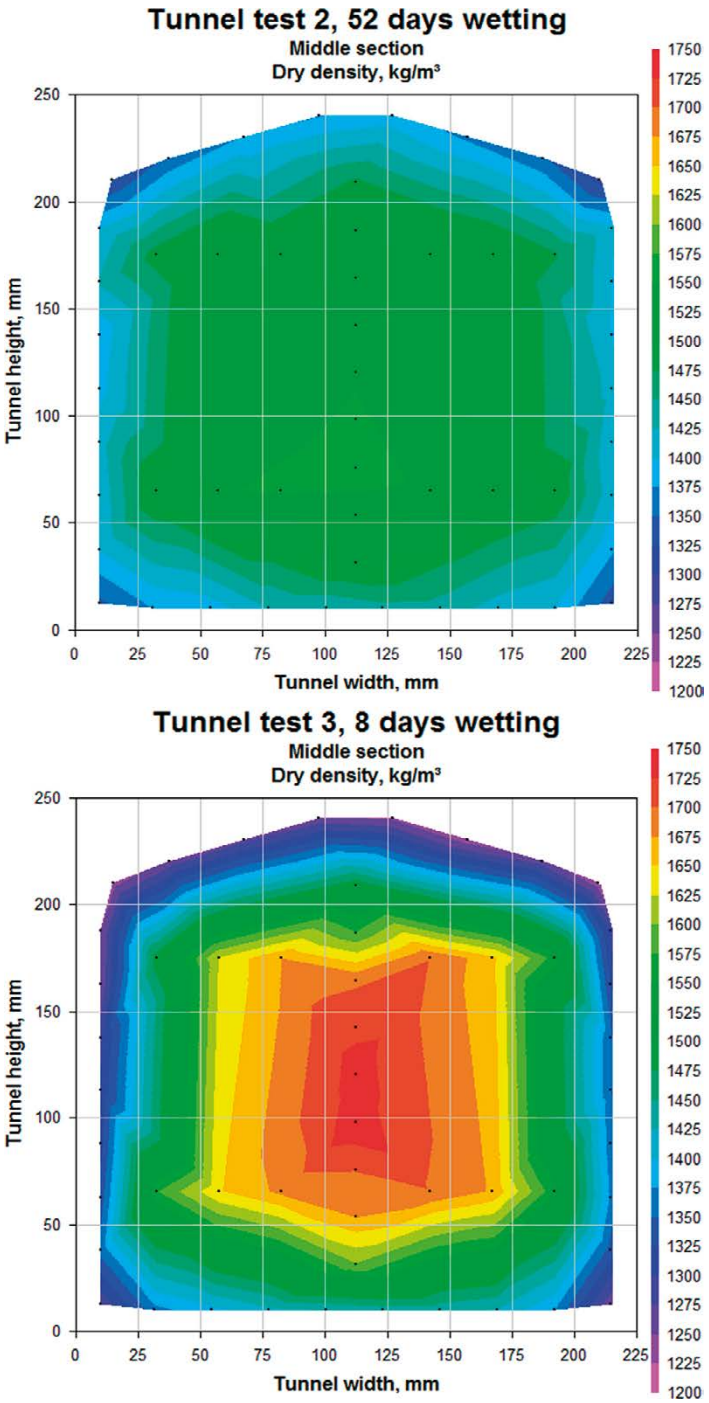

Figure 3-16. *Dry density distribution in the mid cross-sections of Test 2 (upper) and Test 3 (lower).*

Figure 3-17 shows the degree of saturation in Test 2 and Test 3. As shown in the graphs, the degree of saturation is generally high in Test 2, between 91 and 100 %. In Test 3, the central parts of the block stack are almost unaffected after eight days test duration and the degree of saturation is in general between 85 and 90 % which corresponds to the initial state of the backfill blocks.

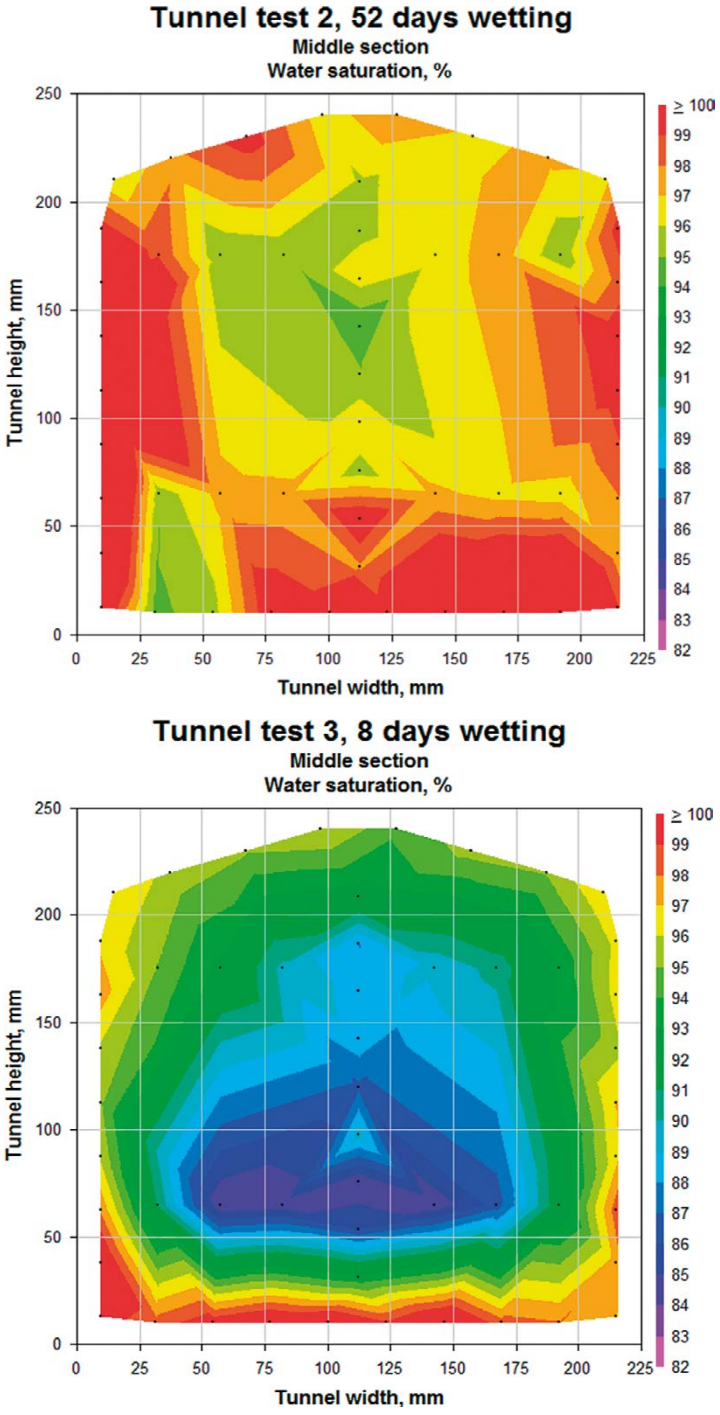

Figure 3-17. *Degree of saturation distribution in the mid cross-sections of Test 2 (upper) and Test 3 (lower).*

3.7 Comments

Some comments to the results achieved from the scale tests are provided below:

- The block filling degree in the scale tests was calculated to 73.7 % which should be compared to 71 % which was calculated for the Äspö Buffer Swelling test performed in full scale (Arvidsson et al. 2015).
- The results from the scale tests show clearly that the case with a completely dry backfill results in the largest displacements.
- The results from the scale test performed with dry backfill are similar to the results achieved from the full-scale test, especially when compensating for the initial load from the block stack in the full-scale test and the thickness of the bottom bed.
- Access to water results in that the backfill becomes stiffer. Backfill that have had access to water for long time will homogenize and will probably get stiffer with time.

4 Additional tests on the backfill components

4.1 General

Several complementary tests have been made on the different backfill components to facilitate the evaluation of the test results and to achieve parameters for the modelling. The following additional tests have been performed:

1. **Block strength**. The block strength is an important parameter for minimizing the upwards swelling from the buffer into the backfilled deposition tunnel. Data from earlier investigations are available but additional tests on the current blocks used in the scale tests have been made.
2. **Volume of gaps in a block stack**. This is an important parameter that is needed for the modelling of the tests.
3. **Compressibility of the block stack**. The compressibility of a block stack has been investigated.
4. **Compressibility of the pellet filling**. The pellet filling has in the scale tests been replaced with granules with a size between 1 to 6 mm. The compressibility of this filling has been determined.

4.2 Block strength

The backfill block strength has been investigated with two different types of tests: Beam tests and Uniaxial compression tests.

4.2.1 Beam tests

Investigations have earlier been made to study the strength on compacted backfill blocks (Sandén et al. 2015, 2016). This data was later completed in conjunction with an investigation on blocks manufactured for a full-scale test on Buffer Swelling performed at Äspö HRL (Sandén et al. 2017). The data from these earlier investigations have been used for comparison with the new results achieved in the present project.

Method

Rectangular beams were prepared by sawing. Testing involved placing the individual beam on supports and then loaded to failure by applying a constant deformation rate of 0.10 mm/min at a localized point in the middle of the beam. The load and the displacement were measured continuously.

The tensile stress (σ_t) and the strain (ε_t) were evaluated with the following equations (see also Figure 4-1).

$$\sigma_t = \frac{6Qc}{4ba^2} \tag{4-1}$$

$$\varepsilon_t = \frac{a\omega 6}{c^2} \tag{4-2}$$

where

Q = vertical force

a = sample height

b = sample width

c = the length between the support points

ω = the vertical displacement at the middle of the beam

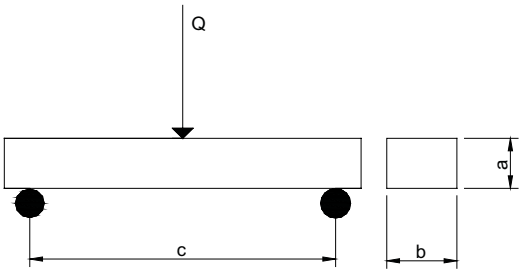

Figure 4-1. *Test arrangement for determination of the tensile strength.*

Test matrix

In total six beam test were performed. The beams were sawed out from blocks compacted in laboratory. The blocks were of the same type as used for sawing out blocks for the scale tests i.e., the same material (Asha 2012), same dry density (1 725 kg/m³) and the same water content (20 %).

The size of the beams used in this test was 20 × 20 × 80 mm.

Results

Figure 4-2 shows the results from the new tests on the tensile strength (black crosses) plotted versus the dry density. The results are presented together with results from earlier laboratory tests performed on the same material (Sandén et al. 2017). As shown in the graph, the achieved block densities are rather high, 1 725 kg/m³, compared to the densities achieved for the full-scale Buffer Swelling test, 1 650–1 680 kg/m³ (red dots in the lower left corner). This has influenced the strength of the blocks which has increased to between 800–1 200 kPa compared to between 100 and 500 kPa for the full-scale blocks.

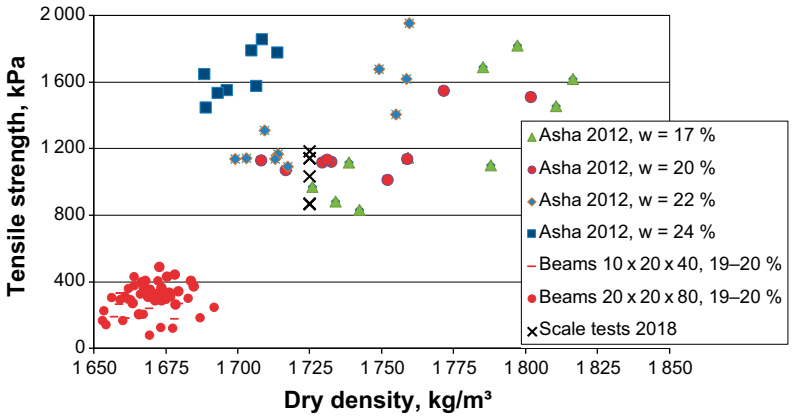

Figure 4-2. *Test results from the present study plotted into a diagram from Sandén et al. (2017). The maximum tensile strength is plotted versus dry density for every specimen. The new results are plotted with black crosses.*

4.2.2 Uniaxial compression tests

The unconfined compression test is an experimentally simple but useful method where a cylindrical specimen is compressed axially under a constant rate of strain with no radial confinement or external radial stress. The method has been used in several studies (e.g. Börgesson et al. 2003, Dueck 2010, Dueck et al. 2011, Svensson et al. 2011). The specimens tested are placed in a mechanical press where a constant rate of deformation is applied to the specimen. During the test the deformation and the applied force are measured by means of a load cell and a deformation transducer.

Method

Preparation of specimen

The method is usually used for saturated cylindrical specimens with a height which is double the diameter. In the test series presented in this report, unsaturated specimens with a rectangular cross-section were used. Rectangular shaped specimens were used since these were possible to prepare by sawing, which were considered the best available method for sampling of the unsaturated Asha 2012 blocks containing large granules.

Test procedure

The specimens were placed in a mechanical press and the compression was run at a constant deformation rate of 0.32 mm/min (which corresponds to 0.8 %/min for a specimen with the height 40 mm), a test procedure which has been used also in earlier test series (see e.g. Dueck et al. 2011). After failure the water content and density were determined.

Evaluation of test results

The deviator stress q (kPa) was calculated as the ratio of the measured vertical load and the initial cross-section area. No correction is made for the change in the cross-section area in the calculated q since the specimen failed after very small deformation (about 2 % strain). The strain e (%) was calculated as the ratio between the change in length and the initial height of the specimen.

Test matrix

The specimens were sawed out from the same type of blocks as used for the scale tests i.e., the same material (Asha 2012), same dry density (about 1 725 kg/m³) and the same water content (20 %).

Three test series have been performed:

1. Specimens with a size of 20 × 20 × 40 mm (five tests).
2. Specimens with a size of 50 × 50 × 45 mm (five tests). These specimens have the same size as the blocks used in the scale tests.
3. Specimens with a size of 50 × 50 × 90 mm (four tests). Same as above but with double height.

Results

In Figure 4-3 the results from the new tests (black, red and green crosses) are plotted together with results from earlier investigations (Sandén et al. 2017). As shown in the graph there is a scatter in the maximum stress, between 2 300 and 4 500 kPa. There is, however, no evident influence of the specimen size.

As for the beam tests, the achieved block densities are rather high, 1 718–1 725 kg/m^3, compared to the densities achieved for the blocks in the full-scale Buffer Swelling test, 1 650–1 700 kg/m³ (cluster of dots in different colours in the lower left corner). This increase in density has influenced the block strength evidently.

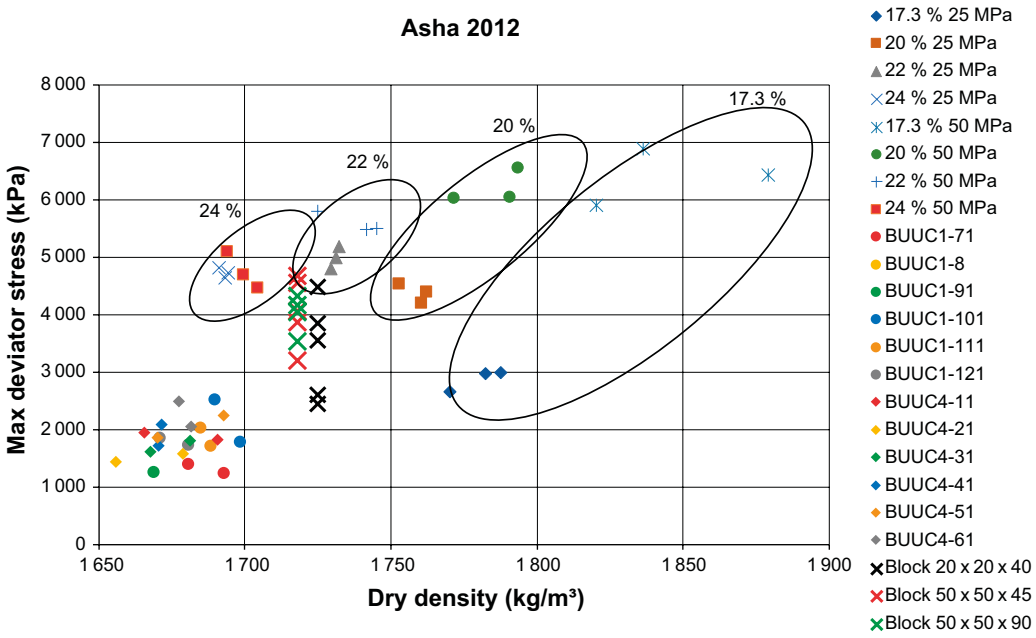

Figure 4-3. *Test results from the present study plotted into a graph from Sandén et al. (2017).*

4.3 Volume of gaps in a block stack

The actual volume of all gaps in a block stack is important data when modelling the backfill compressibility and the water saturation process.

4.3.1 Method

A test was performed in laboratory using the same type of blocks as also was used for the scale tests. The four first layers of the block stack, Figure 3-1, were stacked within a corner of a rigid box, Figure 4-4.

The calculation of the volume of the gaps between the blocks was made according to the following:

1. The outer dimensions of the block stack were measured and then the outer volume of the stack was calculated.
2. The weight of all blocks was determined. With a known bulk density of the backfill blocks it was possible to calculate the actual volume of the blocks.
3. The difference between the whole volume (Bullet 1) and the block volume (Bullet 2) was assumed to be the volume of the gaps in the block stack.

4.3.2 Results

Using the results from the test, the volume of the gaps was estimated to 5.0 %. This result is valid for this scale and with this block quality and can probably be improved using blocks with higher tolerances on the dimensions. In the earlier performed full scale backfill installation test that was performed at Äspö HRL, the volume of the gaps was determined to 2.5 % (Arvidsson et al. 2015).

Figure 4-4. *Backfill blocks were stacked in a corner of a rigid box.*

4.4 Compressibility of the block stack and of the pellet filling at dry conditions

The compression properties of a dry backfill in a deposition tunnel, depends mainly on two things:

- The compression of the block stack i.e., how the initial gaps between the blocks are behaving (closing) when exposed for an outer pressure.
- The compression properties of the pellet filling that is installed both as a bed material on the floor but also in the gaps between the block stack and the ceiling (and walls).

Laboratory tests have been performed to determine the properties of these two components used in the scale tests.

4.4.1 Compression of the block stack

Method

A test was performed in laboratory using the same type of blocks as also was used for the scale tests. The four first layers of the block stack, Figure 3-1, were stacked on a rigid steel plate. Another steel plate was placed at the top of the block stack. The complete test setup was placed in a hydraulic press that compressed the block stack at a constant rate of 0.05 mm/sec, Figure 4-5. During the test time, the applied load and displacement were registered continuously.

The maximum applied stress was set to 1 MPa.

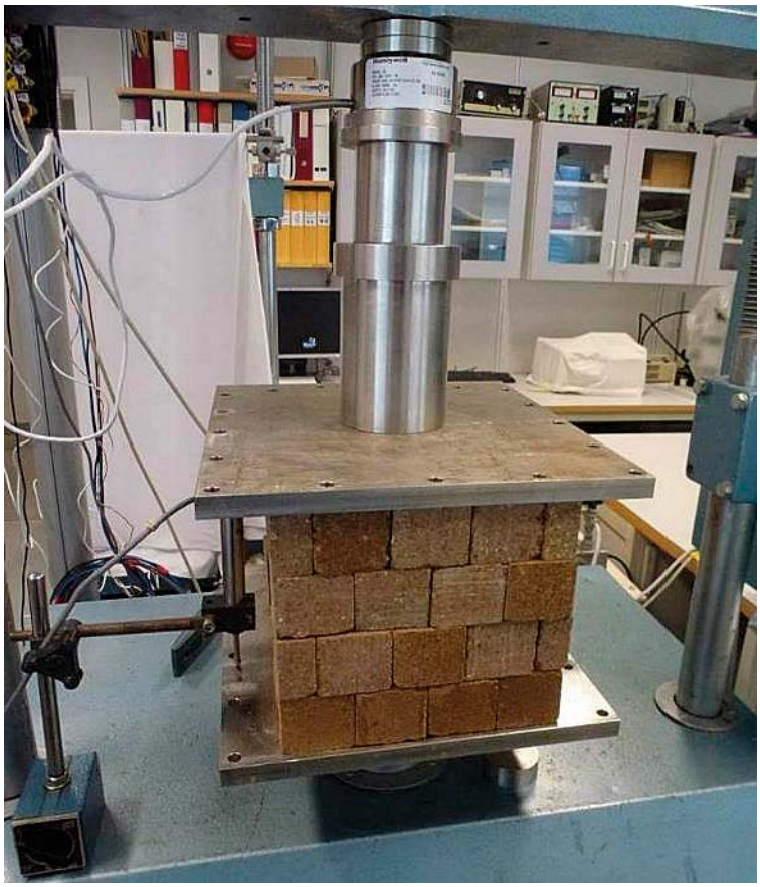

Figure 4-5. *Photo showing the test setup for determining the compression properties of a block stack.*

Results

The results from the test are presented in Figure 4-6 where the applied stress on the block stack is plotted versus the strain. The determined strain of the block stack at a stress of 1 MPa was about 1.7 %.

In Figure 4-7, the results from the compression of the block stack is plotted together with the results from the scale test performed at dry conditions (Test 1). This graph shows the applied stress plotted versus displacement. At an applied stress of 1 MPa, the displacement of the block stack is about 3 mm which corresponds to the total displacement registered for the tunnel test, 6 mm if only the stress on the swelling buffer is considered. The tunnel test includes, except for the block stack, also pellet filling and the difference in displacement depends partly on the compaction of this and partly on the stress spreading in the block stack. Considering the average vertical stress 1 MPa in the blocks stack (average of the stress from the buffer and the stress on the roof) yields the displacement 7.5 mm instead of 6 mm, which additionally increases the difference and shows the large influence of the pellet filling.

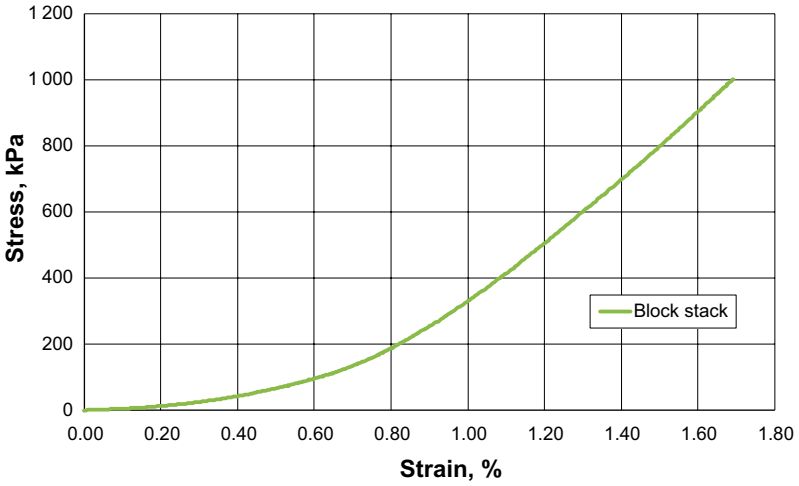

Figure 4-6. *Graph showing the applied stress plotted versus the strain of the block stack.*

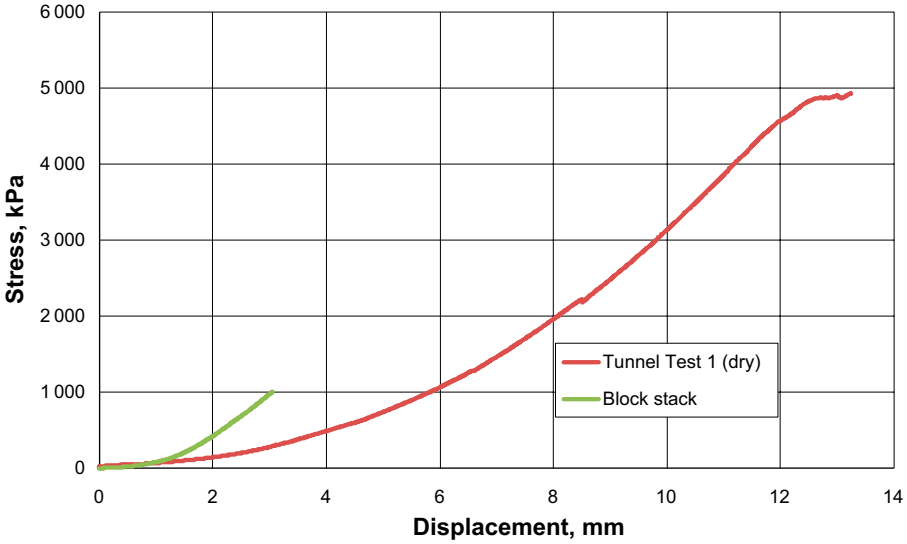

Figure 4-7. *The results from the compression of the block stack is plotted together with the results from the scale test performed at dry conditions, Test 1.*

4.4.2 Compression of the pellet filling

A test has been performed in order to determine the compression properties on the simulated pellet filling used in the scale tests. The simulated pellet filling consists of granules, size 1–6 mm, that were sieved out from the as-delivered raw material (Asha 2012).

Method

The compressibility of the dry pellet filling was evaluated using a CRS-test (Constant Rate of Strain). The test was performed at the following conditions:

- The pellet filling sample was placed in a steel cylinder with a diameter of 101 mm. At the bottom of the cylinder there was a fixed steel plate. At the top of the sample there was a greased piston.
- A hydraulic press was used in order to get a constant deformation rate of 1 mm/min, pushing the piston down to compress the sample.
- The pellet filling sample had an initial height of 80 mm.
- The test was run up to a maximum pressure of 5 MPa.
- Load and deformation were continuously registered by a load cell and a strain gauge.

Results

The results from the test are presented in the graph provided in Figure 4-8. The graph shows the applied stress plotted versus strain. The black line is the test performed with the current granules while the red line represents a test performed in an earlier project (Andersson and Sandén 2012) on the raw material i.e., all grain sizes are included. The green line represents a test with 6 mm pellets manufactured of Asha. This pellet type was used in the full-scale field test concerning Buffer Swelling that was performed at Äspö HRL (Sandén et al. 2017). The compressibility of the granules used in the present test is thus lower than the compressibility of the pellet filling, which has to be taken into account when comparing the tests.

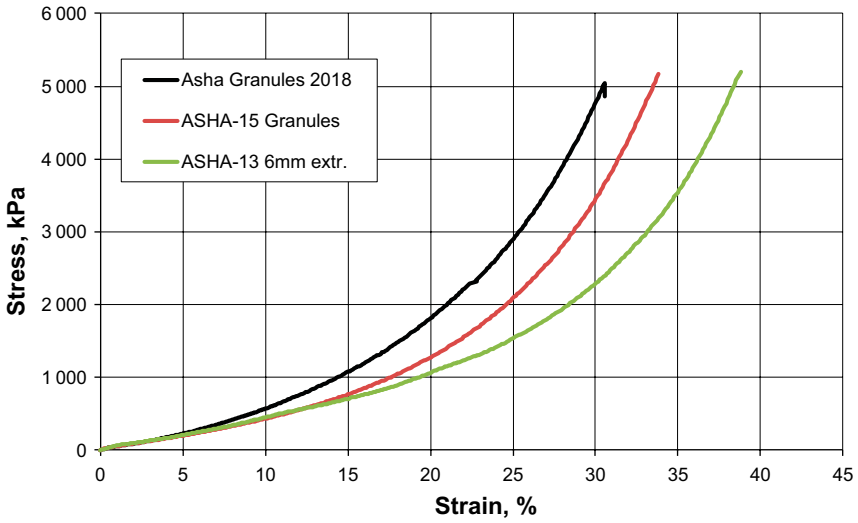

Figure 4-8. *The applied stress plotted versus strain. The black line is the test performed with the current granules while the other two lines represent tests performed in an earlier project (Andersson and Sandén 2012).*

5 Modelling of the deposition tunnel tests

5.1 General

The purpose of this study is three-fold: (1) to develop modelling techniques for the compression of the backfill material due to the upwards swelling of the buffer, (2) to reproduce the results from the laboratory tests, and (3) to assess the potential for up-scaling the laboratory tests to full scale. The modelling efforts are focused on the dry tunnel test as this is the case with the least mechanical resistance to the buffer swelling (cf Figure 3-9).

5.2 Modelling approach

5.2.1 Description of modelling tool

The modelling work is performed with 3DEC, v. 5.2 (Itasca 2016), which is a three-dimensional modelling tool based on the distinct-element method. 3*DEC* simulates mechanical processes (including coupled thermo-mechanical and hydro-mechanical processes) in discontinuous systems that are subjected to either quasi-static or dynamic loads. In this study, no couplings with temperature or hydraulics are considered to imply that all calculations are purely mechanical.

A 3DEC model is constructed from an assemblage of blocks, which can be either rigid or deformable. The interfaces between the blocks can be kept active to simulate a fracture network or be "glued together" for continuum analyses. In this study, each material (i.e., steel/rock, pellets and bentonite blocks) are represented as separate entities with gaps between them. All materials are assumed to be deformable and are discretized with tetrahedral finite-different elements which respond to prescribed stress-strain laws. The relative movements of the gaps are controlled by prescribed force-displacement-relations assigned to so-called subcontracts. To prevent numerical problems, e.g., elements turning inside-out in regions with very large strain such as where the piston pushes against the pellets, the models are analysed in small-strain mode.

5.2.2 Model geometry

The compression of the backfill material is simulated using two different geometrical models: (1) a small-scale model based on the 1:20-scale models used in the tunnel tests (see Chapter 3) and (2) a full-scale model of a tunnel segment with pellets and block stacking pattern based on the reference design (e.g. Arvidsson et al. 2015). Note that an artificial boundary is introduced within the pellets material to avoid numerical problems (a singularity) where the piston pushes against the pellets.

The small-scale model consists of a 300 mm long tunnel-segment with block dimensions and stacking pattern as described in subsection 3.2.1 and shown in Figure 3-1 (top). The model is discretized with tetrahedral finite-difference elements with edge lengths ranging from 3 mm to 7 mm. The model geometry is shown in Figure 5-1 (left).

The full-scale model consists of a 12 m long tunnel-segment. The dimensions of the tunnel cross-section are set at the average between the theoretical tunnel cross-section and the maximum allowed overbreak (cf Table 3-1). The dimensions of the bentonite blocks are set according to the reference design (Arvidsson et al. 2015). For easier implementation in 3DEC, the 25 mm horizontal offset between each layer of blocks is ignored. The rock mass surrounding the tunnel is represented by a more-or-less rigid shell. The model is discretized with tetrahedral finite-difference elements with edge lengths ranging from 42 mm to 170 mm. The model geometry is shown in Figure 5-1 (right).

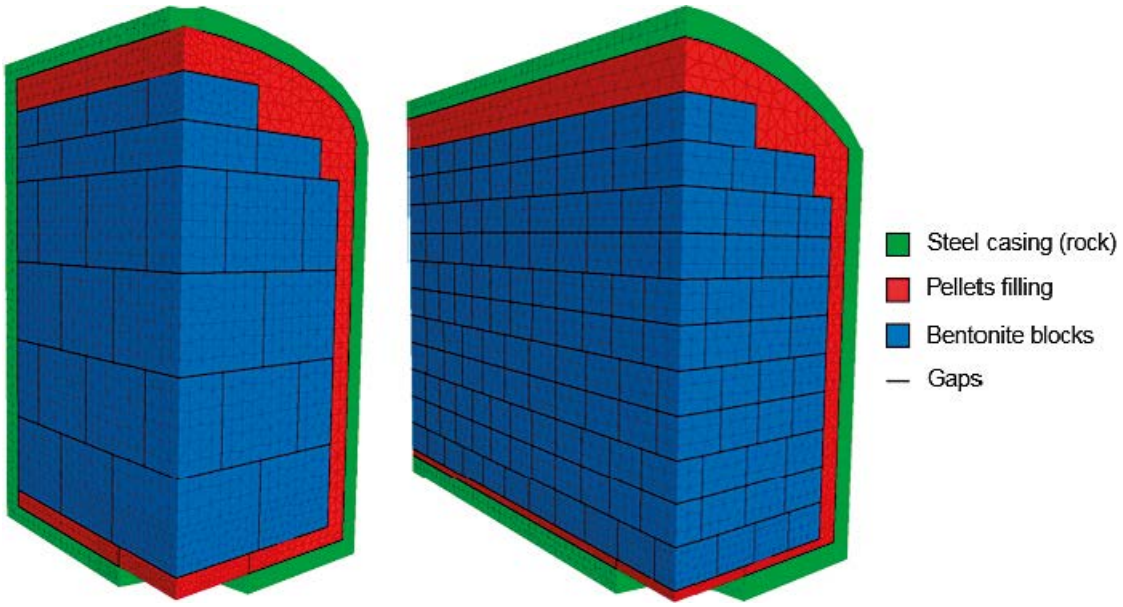

Figure 5-1. *Outline of the numerical models: small-scale model (left) and full-scale model (right). Note that three quarters of each model are hidden to expose the pellets filling and the bentonite blocks.*

5.2.3 Material models and input data

During the early stages of compression, the deformations of the backfill material are likely to be primarily taken up by the pellets and by the gaps between the bentonite blocks. At later stages, the deformability, and ultimately the strength, of the blocks will influence the effective stiffness of the backfill material. To simulate the effective stiffness obtained in the laboratory test, different material models are used for each component; the material models and their parameters are described separately in the sections below.

Steel casing

The main purpose of the steel casing in the scale test is to hold the backfill materials in place. It is represented by a homogeneous, isotropic, and linear elastic material with property values based on typical values for steel, see Table 5-1. In the full-scale models, the rock mass is assumed to be a practically rigid material and is assigned the same properties as the steel casing used in the lab-scale test.

Table 5-1. Material properties and parameter values for the steel casing.

Parameter	Unit	Value
Young's modulus (E)	GPa	200
Poisson's ratio (ν)	-	0.3
Density (ρ)	kg/m^3	8 000

Pellets filling

The pellets material is simulated in 3*DEC* using a material model known as the "double-yield model", which is "*intended to represent materials in which there may be significant irreversible compaction in addition to shear yielding, such as hydraulically placed backfill or lightly cemented granular material*" (Itasca 2016). Input parameters to 3*DEC* are the density (ρ); a multiplier (R) that relates the elastic and plastic bulk moduli; the cap pressure (p_c) and its variation with plastic volumetric strain; the maximum elastic bulk (K) and shear (G) moduli; the friction angle (ϕ), the dilation angle (ψ), the cohesion (c) and their variations with plastic shear strain; and the tensile strength (σ_t) and its variation with plastic tensile strain. Quantities with variations given as functions of plastic strain are provided to 3DEC in tables. A summary of the parameter values is presented in Table 5-2. A justification for the choice of parameter values is provided below.

Table 5-2. Material properties and parameter values for the pellets filling.

Parameter	Unit	Lab-scale	Äspö field test
Maximum elastic bulk modulus (K)	MPa	1 250	1 250
Maximum elastic shear modulus (G)	MPa	577	577
Density (ρ)	kg/m^3	966	1 000
Cap pressure (p_c)*	kPa	0	0
Multiplier (R)	-	100	100
Friction angle (ϕ)**	°	35	30
Dilation angle (ψ)**	°	0	0
Cohesion (c)**	kPa	0	0
Tensile strength (σ_t)**	kPa	0	0

* Initial value. Its variation with plastic strain is proved to 3DEC as a table with values from 0 to 1 in steps of 0.05, cf Figure 5-2 (dashed lines).
** Assumed to be constant.

The parameter values relating to the volumetric properties of the material (i.e., R, p_c, K and G) should ideally be derived from isotropic triaxle compression tests that include small unloading sequences (Itasca 2016). Such tests have not, however, been performed within the scope of this study. Instead, the values for the abovementioned parameters are estimated from stress-strain-relations obtained from confined uniaxial compression tests (oedometer tests) of the pellets (see subsection 4.4.2 and Figure 4-8). As these tests provide only parts of the necessary information needed to derive all parameter values to the material model (including those related to the shear strength), some assumptions are made. The relevance of these assumptions is tested by simulating the oedometer tests with 3DEC (see below):

- It is assumed that the loading results in deformations that are primarily inelastic, which implies that R should be set at a large value. For the purpose of this study, R is set at 100.
- An approximation of the value of p_c for a given value of the plastic volumetric strain is given by $((1 + R)/R)\, p$ (Itasca 2016), where p is the confining pressure (equal to the axial stress). To obtain p_c from the oedometer tests, it is firstly assumed that the measured vertical strain is equal to the volumetric strain and secondly assumed that $p = \sigma_v\, ((1 + \nu)/(1 - \nu))/3$ where σ_v is the measured vertical stress and ν is Poisson's ratio.[1] The data from the oedometer tests are subsequently extrapolated using a function of the form $\sigma_v = A \exp(b\varepsilon_v) - A$, where ε_v is the vertical strain and A and b are parameters (see Figure 5-2). The extrapolated relations are used as input to 3DEC.
- The maximum elastic bulk (K) and shear (G) moduli are estimated using a trial-and-error method from the simulated oedometer tests.
- Parameter values relating to the shear strength (friction angle) of the material used in the small-scale tests are estimated by pouring the pellets into a heap and measuring the angle of the slope. The parameter values in the full-scale models are estimated from the simulated oedometer tests. The artificial boundary within the pellets material (cf subsection 5.2.2) has the same shear strength as the solid material.

Figure 5-3 shows an illustration of the 3DEC model used to simulate the oedometer tests. The model consists of two parts: an inner cylinder with a height of 80 mm and diameter of 101.4 mm that represents the pellets material and an outer, hollow, cylinder that represents the test equipment:

- The test equipment is assumed to respond to loading as a linear elastic material with material property values that are relevant for steel (cf Table 5-1).
- The pellets materials are assumed to respond to loading according to the double-yield model (Itasca 2016). Input parameter to be derived from the simulations are the maximum elastic bulk and shear moduli (assumed to be the same for both the lab-scale models and the large-scale models) and the internal angle of friction of the pellets material used in the large-scale models. Other parameter values are set according to Figure 5-2 and Table 5-2.

[1] The slope of a stress-strain curve obtained from an isotropic triaxial compression test gives a measure of the bulk modulus (K) whereas the slope of a corresponding curve obtained from an oedometer test gives a measure of the oedometer modulus (M). The M modulus is converted to bulk modulus using $K = M\, ((1 + \nu)/(1 - \nu))/3$.

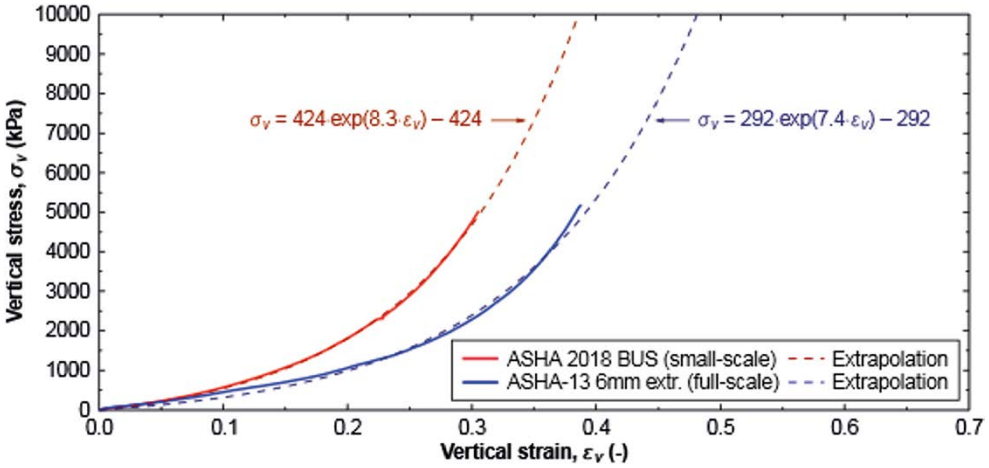

Figure 5-2. *Stress-strain relations obtained from oedometer tests (solid lines, redrawn from Figure 4-8). The extrapolated relations (dashed lines) are used as input to the 3DEC models.*

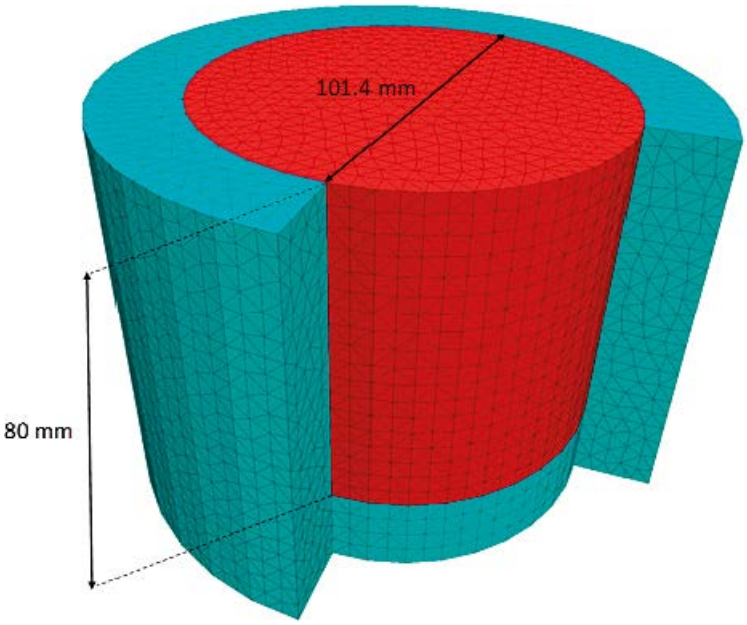

Figure 5-3. *Illustration of the 3DEC model used to simulate the oedometer tests of the pellets materials. Note that parts of the test equipment (marked in turquoise) are hidden to expose the pellets material (marked in red).*

The gaps between the pellets and the test equipment are assumed to respond to loading according to an idealised elastic-plastic constitutive relation with Mohr-Coulomb shear failure. The normal and shear stiffness's are set at high values in order to suppress elastic deformations. The cohesion and tensile strength are both set at zero. Different values of the friction angle are considered to test influence of friction between the pellets material and the test equipment.

The bottom surface of the model is locked in all directions; all other outer boundaries of the parts of the model that represent the test equipment are free. The top surface of the pellets is assigned a velocity boundary condition and is compressed downwards in steps of 5 mm to a total deformation of 50 mm.

The maximum elastic bulk ($K = E/[3(1-2\nu)]$) and shear ($G = E/[2(1+\nu)]$) moduli are determined using a trial-and-error method. The starting point is a model with the maximum elastic Young's modulus (E_{max}) set at 500 MPa and no friction between the pellets sample and the test equipment. The value of E_{max} is increased in steps of 500 MPa in subsequent models. Poisson's ratio (ν) set at 0.3 in all models. The results are shown in Figure 5-4a. All three models show a similar response to loading at low strain with

significant differences occurring at strains above ~40 %. The best fit to the extrapolated stress-strain curve at strains in the range 50–60 % is found for the highest tested value of E_{max} = 1 500 MPa. This value is, therefore, used as input to the models (see Table 5-2).

The influence of friction between the pellets sample and the test equipment is assessed by comparing the results from the model without friction (E_{max} = 1 500 MPa) with a corresponding model in which the friction angle is set at 50 % of the internal angle of friction (0.5 × 35° = 17.5°). The results are shown in Figure 5-4b. For strains lower than about 30 %, i.e., within the range tested in the laboratory, any friction between the pellets sample and the test equipment does not appear to have any significant impact on the stress-strain relations. Note that, although wall friction does influence the stress-strain relations at larger strains, the true mechanical response of the pellets is unknown. It is, therefore, not feasible to attempt to compensate the stress-strain relations used in the numerical models (cf Figure 5-2, dashed lines) for wall-friction.

The internal angle of friction (ϕ_P) of the pellets material used in the large-scale test has not been determined. Given the results from the oedometer test of the pellets material used in the lab-scale models (cf Figure 5-4), it is firstly assumed that the values determined for the maximum elastic bulk and shear moduli are also appropriate for the pellets material used in the large-scale test. Secondly it is assumed that there is no friction between the pellets and the test equipment. Three different values for the internal angle of friction of the pellets are tested: 38° (pellets with a similar shape, see Glamheden et al. (2010, Appendix F)), 35° (value used in the modelling of the lab-scale tests in this study) and 30° (value used by Börgesson and Hernelind (2017)). The results are presented in Figure 5-5. Here, the lowest tested value gives the best fit to the measurement data and to the extrapolated relation and is, therefore, used as input to the large-scale models (see Table 5-2).

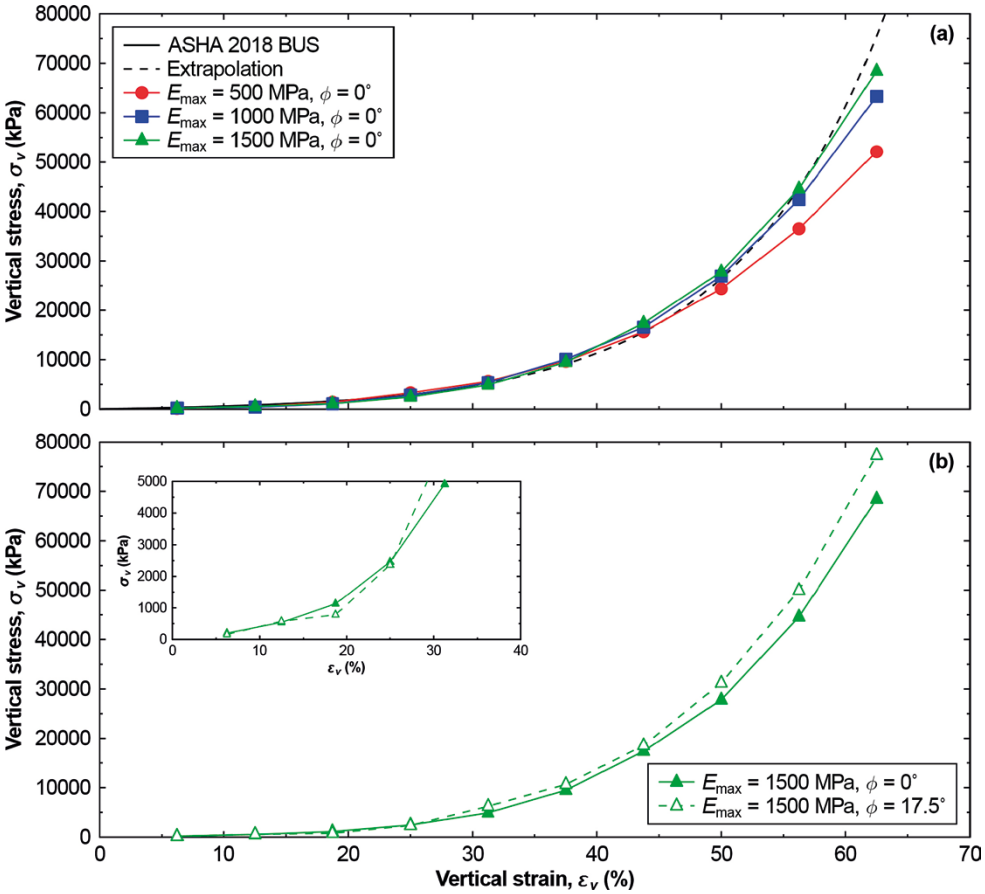

Figure 5-4. *(a) Stress-strain relations for different assumptions regarding the value of the maximum elastic Young's modulus. (b) Comparison between the case without friction between the pellets and the test equipment (ϕ = 0°) and a case in which the friction angle of the gaps between the pellets material and the test equipment is set at 50 % of the internal angle of friction of the pellets (ϕ = 17.5°). The inset shows the results plotted between 0 and 40 % strain, i.e. approximately in the range of the measurements.*

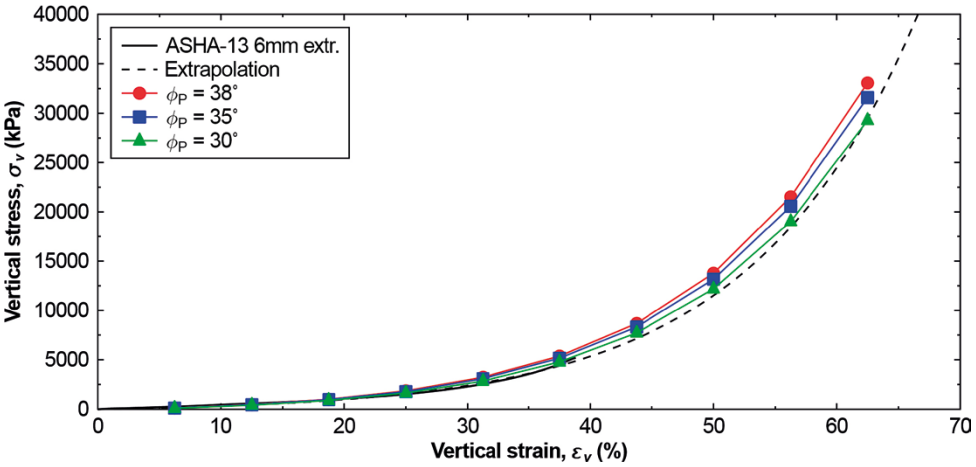

Figure 5-5. *Comparison between the oedometer test of the pellets material used in the large-scale test (solid black line), the extrapolated relation (dashed black line) and the corresponding 3DEC models with the internal friction angle of the pellets (ϕ_p) set at 38°, 35° or 30° (coloured lines).*

Bentonite blocks

The bentonite blocks are assumed to respond to loading either as a linear elastic material or as a Mohr-Coulomb material, see Table 5-3 for a summary of input parameters and values. The means to determine the parameter values relating to the deformability and to the shear and tensile strengths are described in the subsections below.

Table 5-3. Material properties and parameter values for the backfill blocks.

Parameter	Unit	Lab-test	Äspö field test
Young's modulus (E)	MPa	387	245
Poisson's ratio (v)	-	0.17	0.17
Density (ρ)	kg/m^3	1 986	1 989
Friction angle* (ϕ)	°	35	30
Cohesion** (c)	kPa	1 100	460
Tensile strength*** (σ_t)	kPa	1 000	200

* The friction angle is set at the same value as for the pellets (see previous section and Table 5-2).
** The cohesion is preserved after shear failure has occurred.
*** The tensile strength is reduced to zero after tensile failure has occurred.

Block deformability and uniaxial compressive strength

The value of Young's modulus (E) and the uniaxial compressive strength (UCS) of the bentonite blocks used in the lab-scale test are based on the results from the uniaxial compression tests described in subsection 4.2.2. The values of E and UCS used in the large-scale modelling work are taken from Börgesson and Hernelind (2017) and from Sandén et al. (2017, Section 7.5), respectively.

For the purpose of deriving material property values for the small-scale models, only the samples with the same cross-sectional area as the blocks used in lab-scale tests (i.e., 50×50 mm^2) are considered here: in total 9 samples. Five of these have a height of 45 mm and the remaining ones 90 mm. Figure 5-6 shows the deviator stress (vertical stress), q, for each sample as a function of the (vertical) strain, ε. Note that the mechanical response of sample h45_1 deviates significantly from all other samples. This sample is, therefore, not considered in the evaluation of Young's modulus and of the uniaxial compressive strength.

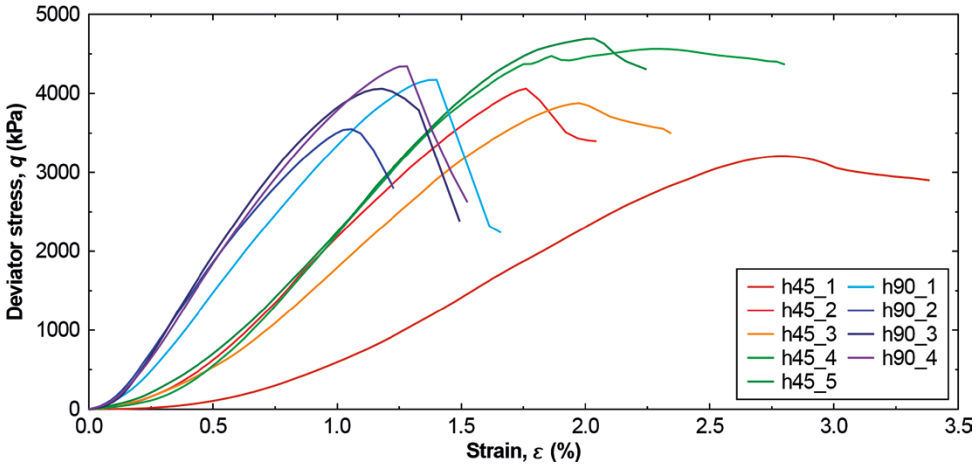

Figure 5-6. *Deviator stress (vertical stress) as a function of the (vertical) strain for samples with a cross-section area of 50 × 50 mm², see Section 4.2.2. Samples labelled h45_x and h90_x have heights of 45 mm and 90 mm, respectively.*

The uniaxial compressive strength and Young's modulus of each sample are evaluated as follows (see Table 5-4 and Table 5-5):

- $UCS = \max(q)$.
- $E = \Delta q/\Delta\varepsilon$ between 40 % and 60 % of the *UCS*.

The values of the uniaxial compressive strength are in the range 3 500–4 700 kPa with a mean value of 4 300 kPa for the 45 mm-samples and 4 000 kPa for the 90 mm-samples.

The values of Young's modulus are in the range 285–473 MPa with a mean value of 333 MPa for the 45 mm-samples and 440 MPa for the 90 mm-samples. The large differences between the two sample sets could possibly be attributed to the loading direction in the tests compared with the original compaction direction of the larger blocks the samples were extracted from. It appears that only the deformation properties are influenced by the loading direction as a corresponding difference between the two sample sets was not observed in the uniaxial compressive strength.

Note that the orientation of each block with regard to the original compaction direction was not documented during the installation of the lab-tests. It is, therefore, not meaningful to attempt to account for the observed anisotropy in the numerical models. Instead, an average value based on all samples is used as input to the models.

Table 5-4. Values of the uniaxial compressive strength (*UCS*) for each sample. Note that all values have been rounded to the nearest 100 kPa.

Sample name	*UCS* (kPa)	Sample name	*UCS* (kPa)
h45_2	4 100	h90_1	4 200
h45_3	3 900	h90_2	3 500
h45_4	4 600	h90_3	4 100
h45_5	4 700	h90_4	4 300
Average (h45)	4 300	Average (h90)	4 000
Average (all samples): 4 200 kPa			

Table 5-5. Values of Young's modulus (*E*) for each sample.

Sample name	*E* (MPa)	Sample name	*E* (MPa)
h45_2	324	h90_1	394
h45_3	285	h90_2	439
h45_4	368	h90_3	473
h45_5	357	h90_4	455
Average (h45)	333	Average (h90)	440
Average (all samples): 387 MPa			

The value of Poisson's ratio (v) is assumed to be same in both the lab-scale models and in the model of the Äspö field test (see Börgesson and Hernelind 2017).

Block strength

The failure envelope is given by a Mohr-Coulomb criterion with a tension cut-off (cf Itasca 2016):

- The friction angle of the blocks is unknown. For convenience, it is assumed that the internal angle of friction (ϕ) in the blocks is the same as the internal angle of friction in the pellets (see Table 5-2).
- The cohesion (c) is determined by fitting a Mohr-Coulomb failure envelope to a Mohr-circle representation of the state of stress at the onset of failure, i.e., $\sigma_1 = UCS$ (see Figure 5-7). The UCS for the small-scale blocks is assumed to be about 4 200 kPa (see Figure 4-3 and Table 5-4) and 1 600 kPa for the full-scale blocks (Sandén et al. 2017, Section 7.5).
- The tensile strength (σ_t) in the small-scale models is assumed to be an average value based on the results presented in Figure 4-2 (Scale tests 2018). In the large-scale models, the value is estimated from lab-tests performed by Sandén et al. (2017, Figure 6-6).

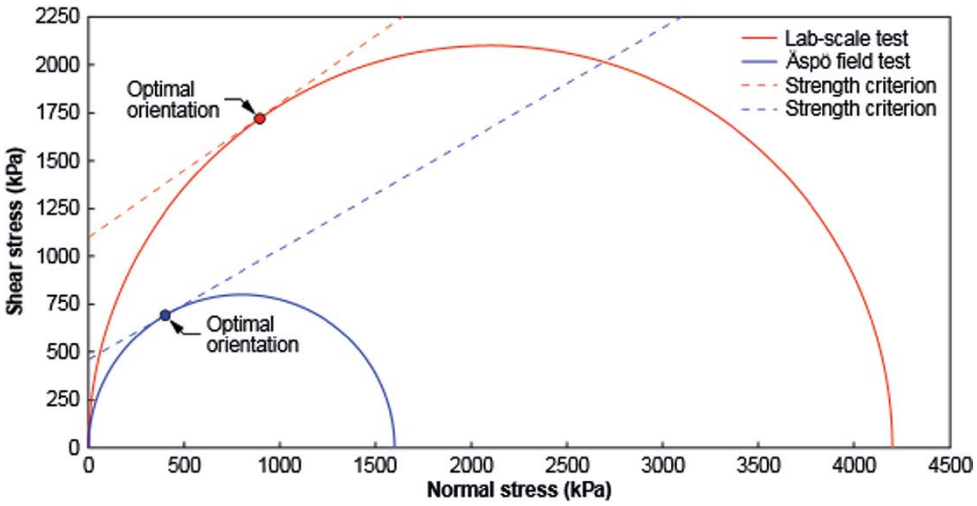

Figure 5-7. *Mohr circle representation of the state of stress at failure.*

Gaps

The gaps between the different components (i.e., pellets/steel or rock, blocks/steel, blocks/pellets and blocks/blocks) are assumed to respond to loading according to an idealised elastic-plastic constitutive relation with Mohr-Coulomb shear failure.

The gaps between the pellets (or blocks) and the steel casing have constant normal and shear stiffness's set at high values in order to suppress elastic deformations. The friction angle is set at 50 % of the internal angle of friction of the pellets/rock in the lab-scale test and 100 % of the internal angle of friction in the large-scale test, respectively (cf Table 5-2 and Table 5-3).

The normal stiffness of the gaps between the blocks is estimated from a compression test of the block stack, cf subsection 4.4.1. Figure 5-8 shows an illustration of the test setup. The test setup consists of a block stack with four layers of blocks with a total height (H) of 4×45 mm. It is assumed in the following that the individual blocks in the block stack respond to loading as a linear elastic material. It is further assumed that the block stack is in contact with the steel plates and that the three horizontal gaps marked in red are the only ones that contribute to the effective stiffness of the block stack. The gaps between the blocks and the steel plates (marked in blue) are, therefore, ignored. Note that this approach may have resulted in an underestimate of the normal stiffness in the stress range 0–1 MPa.

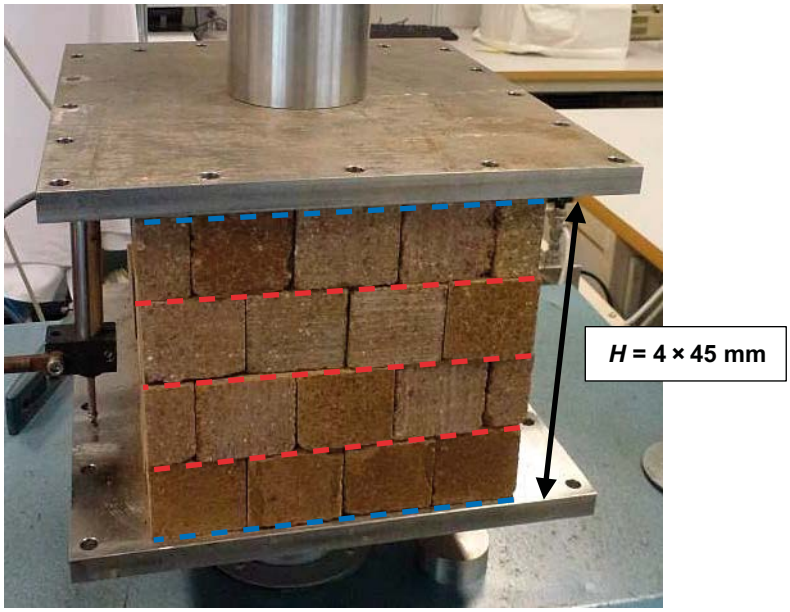

Figure 5-8. *Illustration of the test setup to determine the compressibility of the block stack (modified from Figure 4-5). It is assumed here that the three horizontal gaps marked in red are the only ones that contribute to the effective stiffness of the block stack. The gaps between the blocks and the steel plates (marked in blue) are ignored.*

Figure 5-9a shows the measured deformation of the block stack (u_B) as a function of the normal (vertical) stress (grey line) and corresponding estimates of the deformation of the blocks for different assumptions regarding the value of Young's modulus (E). Here, three values are tested: the mean value E = 387 MPa based on all blocks, the minimum value (E = 285 MPa) and the maximum value (E = 473 MPa), cf Table 5-5. For each value of E, the gap-deformation (u_G) as a function of the normal stress (σ_N) is subsequently calculated (see Figure 5-9b):

$$u_G(\sigma_N) = \frac{u_B(\sigma_N) - \left(H\frac{\sigma_N}{E}\right)}{3} \tag{5-1}$$

where $H = 4 \times 45$ mm is the height of the block.

Since the response of the gaps in the normal direction at stress-levels above 1 MPa is unknown, the estimated gap-deformations in Figure 5-9b are extrapolated using a relation of the form:

$$\sigma_n = Au_n^b \tag{5-2}$$

where σ_n is the normal stress, u_n is the normal deformation of a gap, and A and b are parameters. For consistency with the input assumption to the lab-scale models (cf subsection 5.2.3), the curve based on the mean value E (black line in Figure 5-9b) is used here to derive stress-stiffness relations for the gaps. Three different values of b = 2.0, 2.5 and 3.0 are chosen to investigate the sensitivity of the results in the lab-scale models to the gap stiffness. In the large-scale models, Equation (5-2) is fitted to the relation used by Börgesson and Hernelind (2017) using b = 2.5. The resulting gap-deformations as functions of the normal stress are presented in Figure 5-10a.

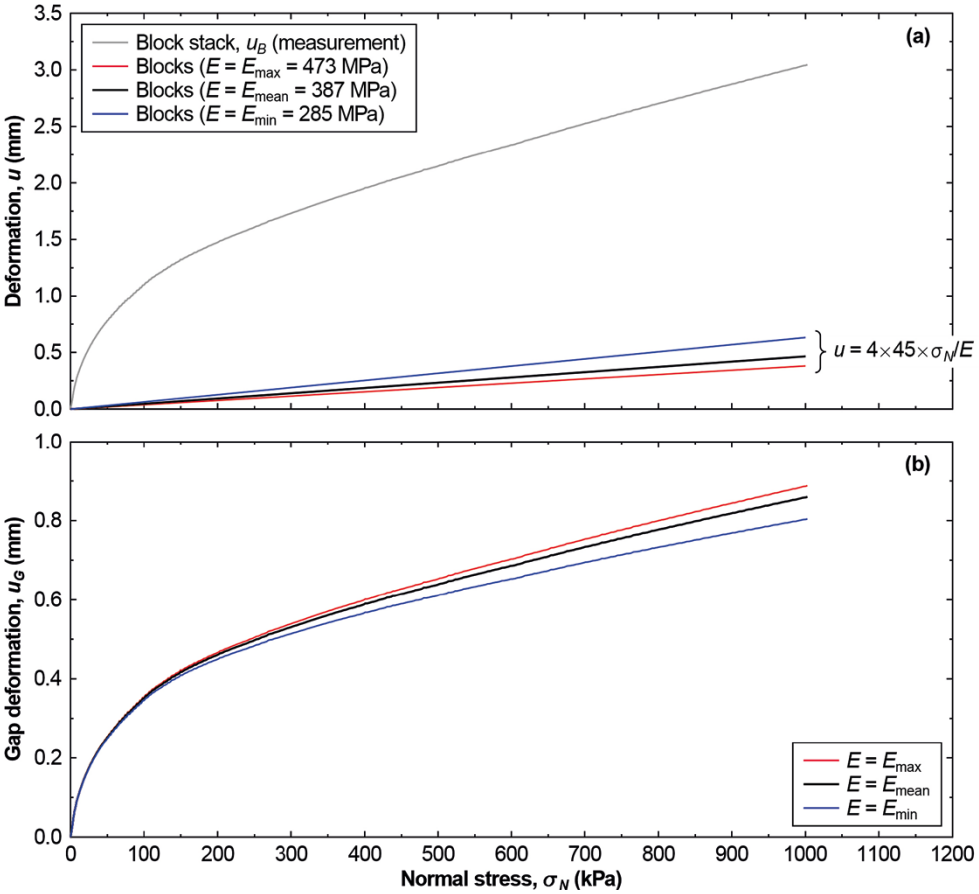

Figure 5-9. *(a) Comparison between the deformation of the block stack and the deformation of the blocks for different assumptions regarding the value of Young's modulus. (b) Gap deformations as functions of the normal stress evaluated using Equation (5-1).*

It follows from Equation (5-2), that the normal stiffness (k_n), as a function of σ_n, is given by

$$k_n = \frac{d\sigma_n}{du_n} = A^{1/b} b \sigma_n^{1-1/b} \tag{5-3}$$

The stress-stiffness relations are presented in Figure 5-10b. The stiffness relation is implemented in 3DEC using the programming language *FISH* and updated at regular intervals during the calculation process.

The shear strength of the gaps between the small-scale blocks is determined from three tilt tests of two blocks with (1) pressed/pressed surfaces put together, (2) sawed/sawed surfaces put together, and (3) pressed/sawed surfaces put together. In the small-scale models, the friction angle between the individual blocks is based on the average value from the three tests. In the large-scale model, the same values as in the study by Börgesson and Hernelind (2017) are used. The cohesion is assumed to be 0 kPa in both types of models.

For the purpose of this study, it is assumed that the response of the gaps between the pellets and the blocks is the same for the block-block-gaps. The parameter values are summarised in Table 5-6 and in Figure 5-10b.

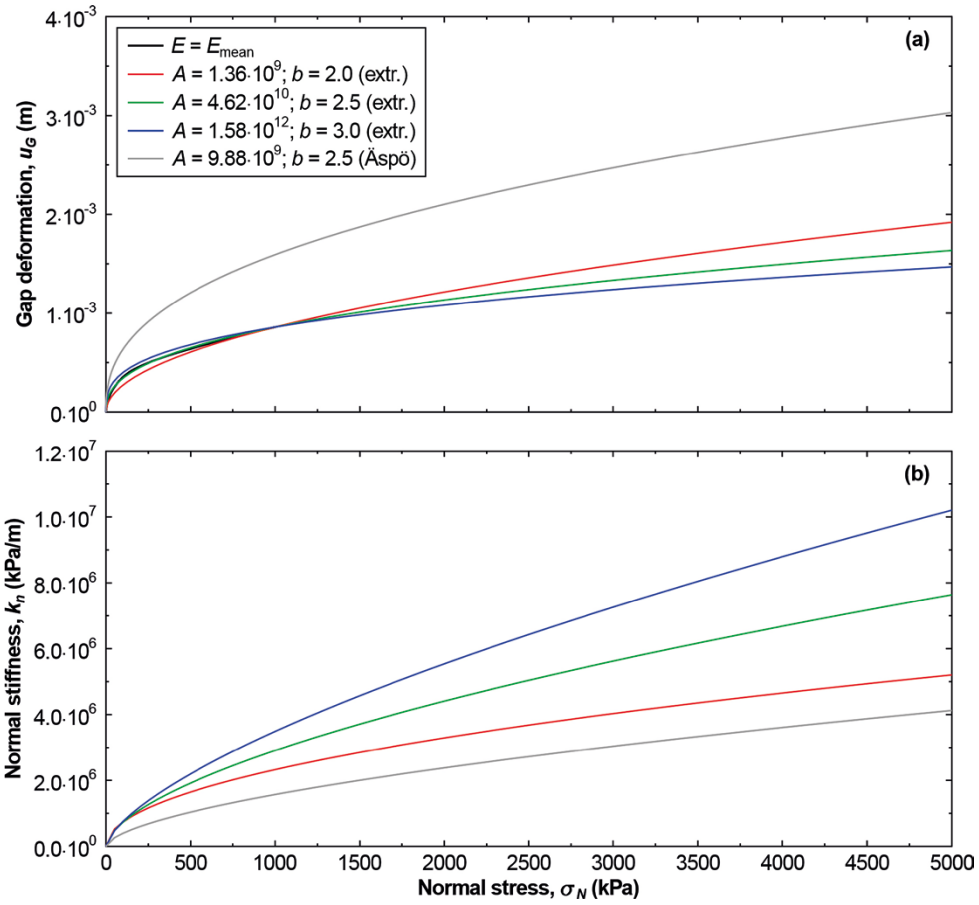

Figure 5-10. *(a) Stress-deformation relations for the gaps based on the compression test of the block stack (black line, cf Equation (5-1)) and for different assumptions regarding the values of the parameters A and b. (b) Corresponding stress-stiffness relations for the gaps used as input to the numerical models. The same legend applies to both sub-figures.*

Table 5-6. Material properties and values for the gaps. Values in brackets refer to the ones used in the Äspö field experiment (see Börgesson and Hernelind 2017).

Parameter	Unit	Pellets-Steel*	Blocks-Steel**	Blocks-Pellets	Block-Block
Normal stiffness (k_n)	kPa/m	3.5e8	3.5e8	see Figure 5-10b	see Figure 5-10b
Shear stiffness (k_s)	kPa/m	3.5e8	3.5e8	3.5e8	3.5e8
Friction angle (ϕ)	°	17.5 (30)	17.5	25 (20)	25 (20)
Cohesion (c)	kPa	0	0	0	0
Tensile strength (σ_t)	kPa	0	0	0	0

* Pellets-Steel corresponds to Pellets-Rock in the full-scale models.
** Combination used only in the lab-scale experiment.

5.2.4 Initial- and boundary-conditions

In the small-scale models, the outer boundaries of the model are locked in all directions and gravity is ignored.

In the full-scale models of the Äspö field test, the tunnel end surfaces are treated as symmetry planes (although this is not strictly the case) and assigned roller boundaries. All other outer boundaries are locked in all directions. In these models, gravity is included.

5.2.5 Simulation sequence

All models are subjected to quasi-static loading. Thus, the models must be compressed in discrete steps and cycled to equilibrium between each step. To do so, a velocity boundary condition is assigned on a circular area on the pellets corresponding to the piston. Preliminary calculations (not presented here), indicated that the model results were sensitive to abrupt changes in velocity. To obtain a smooth transition from acceleration to retardation, a sinusoidal velocity function, v, is applied over N cycles:

$$v(c) = \frac{\Delta z\left(\sin\left(2\pi\left[c - 0.25N\right]/N\right)+1\right)}{N\Delta t} \tag{5-4}$$

where c is the current cycle, Δz is the change in vertical compression, N is the number of cycles and Δt is the mechanical timestep. Each N-cycle compression-step corresponds to a compression of Δz mm. After each step, the boundary is locked in all directions and the model is cycled to equilibrium.

5.2.6 Evaluation of results

The results are presented as a weighted average of the vertical stress over an area corresponding to the deposition hole as a function of the vertical deformation of the pellets. In the lab-scale models, a corresponding evaluation is made of the stress in the ceiling (the weighted average is here made over a circle with diameter 20 mm).

5.3 Results

5.3.1 Lab-scale tests

Sensitivity to compression speed

To test the sensitivity of the stress above the piston to the compression speed, the model is compressed in 2-mm-steps over 2 500, 5 000 and 10 000 cycles to in total 14 mm. The results are presented in Figure 5-11. As the difference between the results obtained using a compression over 5 000 and 10 000 cycles is very small, a compression rate of 2 mm in 5 000 cycles is used in the following.

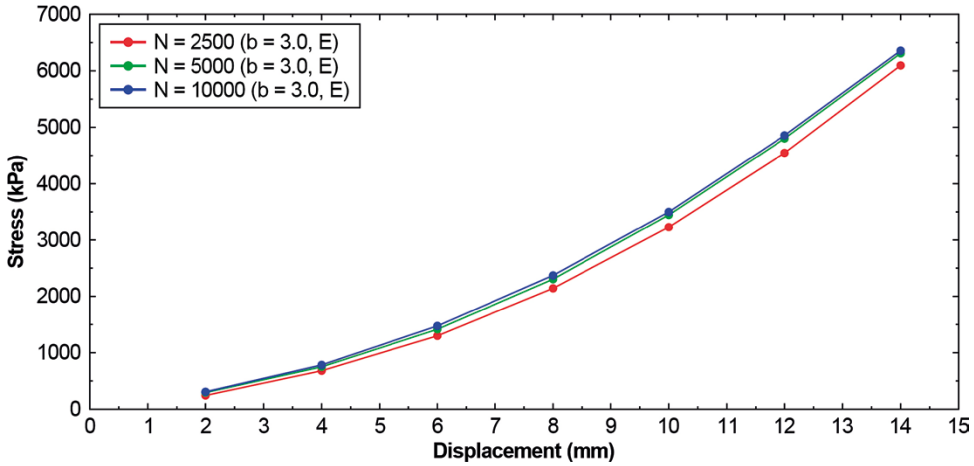

Figure 5-11. *Influence of the rate of compression on the stress above the piston.*

Sensitivity to gap-stiffness variations

Having established a suitable speed of compression of the pellets (cf Figure 5-11, $N = 5\,000$), the influence of the normal stiffness of the gaps between the blocks is tested. The results are shown in Figure 5-12. Since the block stack was tested up to a normal stress of only 1 MPa, three different assumptions are made for the gap-stiffness at high normal stress. For low normal stress (up to about 1 MPa), all three models give approximately the same results and overestimate the measured stress in the floor. At higher normal stress, the results diverge. The stiffest of the three tested gap-stiffness-models overestimates the measurement but qualitatively gives the best fit to the data. All three models underestimate the measurements in the ceiling.

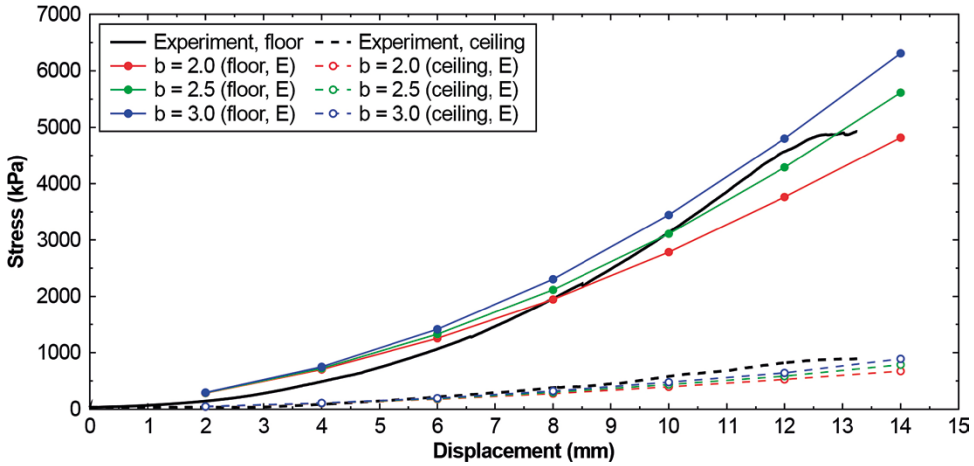

Figure 5-12. *Comparison between the measured stress in the floor/ceiling and corresponding results from 3DEC models with linear elastic blocks and different assumptions regarding the stiffness between the blocks.*

Influence of block strength

The block strength in the experiment was reached after about 12–13 mm of compression (see subsection 3.6.4 and Figure 3-11). To simulate failure, each 3DEC model is re-analysed with the block material model changed to one with Mohr-Coulomb shear strength. The results are presented in Figure 5-13. In the all three models, failure appears to be initiated after 10–12 mm of compression, i.e., slightly earlier than in the experiment.

Comparison between modelled and measured deformations of blocks and gaps

To assess to what extent the overall pattern of deformation in the test could be reproduced by the numerical models, the results after 14 mm of deformation obtained from the 3DEC model which best reproduced the measured stress-deformation curve (linear elastic blocks, $b = 3.0$) are compared with a photograph taken during the dismantling of the test, see Figure 5-14. Note that the upwards displacements of the blocks in the experiment were not measured meaning that only qualitative comparisons between the experiment and model results are possible. The pattern of vertical deformations is similar in both the experiment and in the model: a compaction of the pellets directly above the piston and a "fan-shaped" deformation pattern of the blocks. The pattern of opening and closure of the gaps between the blocks could also be reproduced very well by the model.

5.3.2 The Buffer swelling test at Äspö HRL

The Buffer swelling test at Äspö HRL has previously been modelled by Börgesson and Hernelind (2017) and by Leoni et al. (2018). In this study, the experiment is modelled again using the approach described above.

Sensitivity to compression speed

First, a test is made to determine if the boundary velocity can be upscaled, i.e., if the pellets can be compressed in steps that are 20 times larger than in the lab-scale model in the same number of cycles. This would correspond to 40 mm of compression in 5 000 cycles. Here, however, the pellets are compressed 20 mm in 5 000, 10 000, 20 000 or 40 000 cycles to, in total, 120 mm. As seen in Figure 5-15, 20 mm compression in 20 000 or 40 000 cycles yields approximately the same results, i.e., upscaling is not possible and approximately the same rate as in the small-scale models is needed. In the following, compression over 20 000 cycles is used.

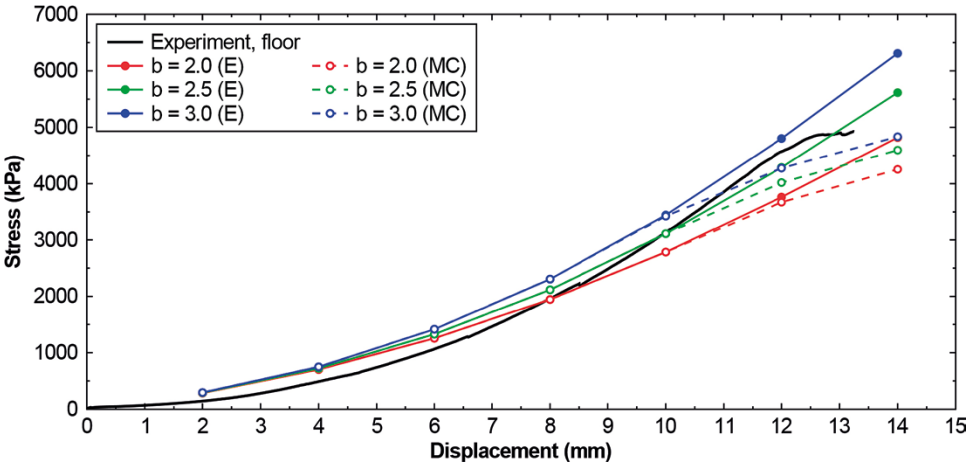

Figure 5-13. *Stress above the piston as functions of the vertical deformation assuming either linear elastic blocks (E) or linear elastic blocks with Mohr-Coulomb shear strength (MC).*

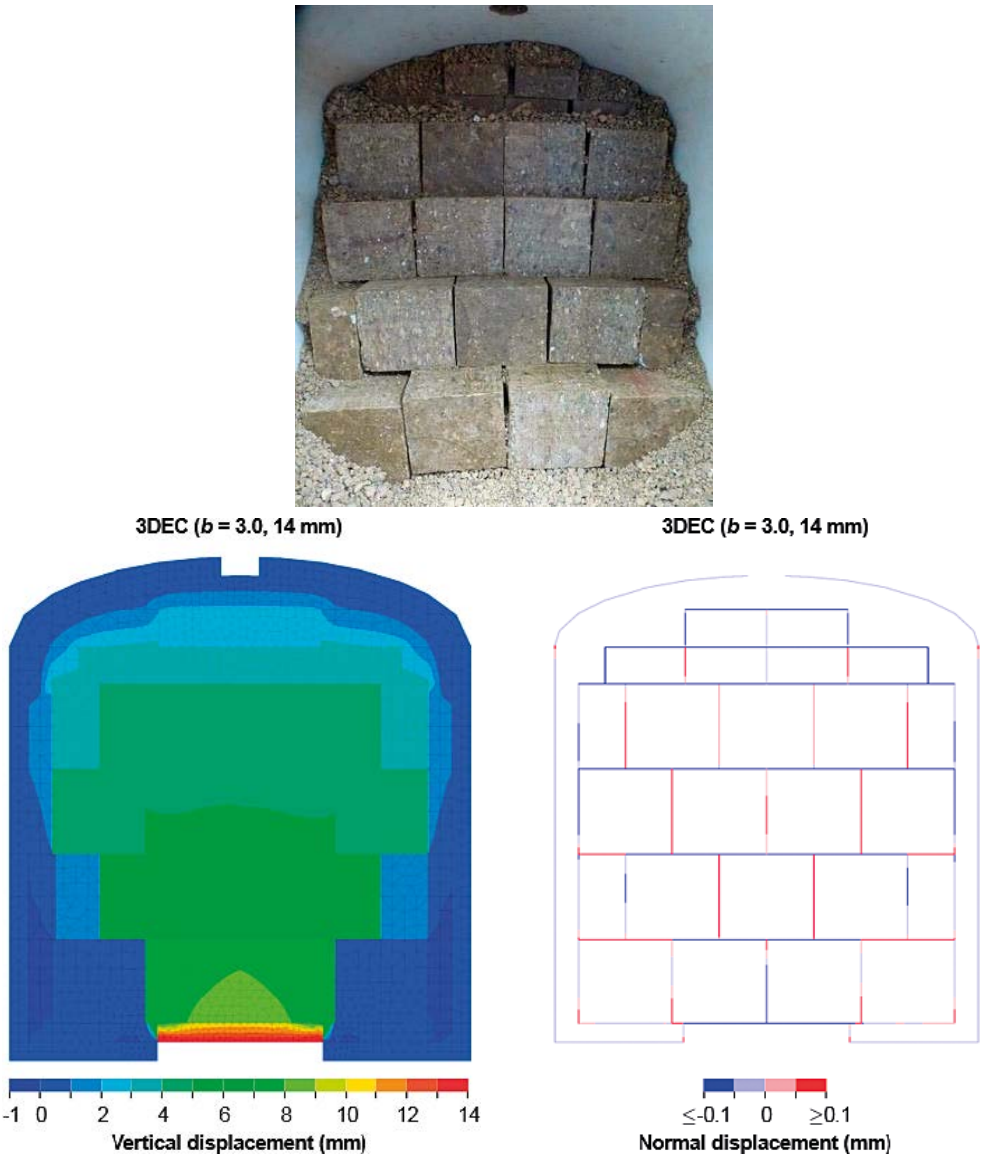

Figure 5-14. *Top: Photograph of the block stack in the dry test taken during the dismantling work (redrawn from Figure 3-11). Bottom left: Distribution of vertical displacements after 14 mm of deformation in a vertical cross-section through the centre of the model. Bottom right: Corresponding view of the normal displacements of the gaps between the blocks (red colours indicate an opening of the gaps).*

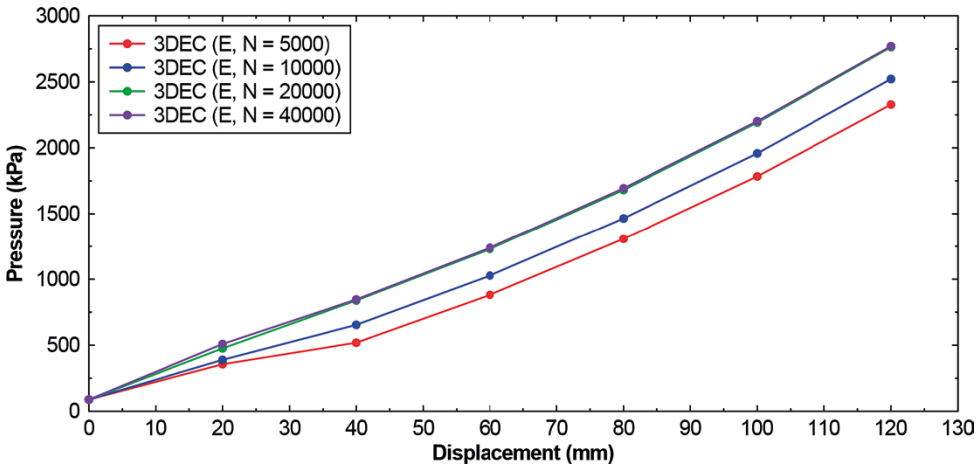

Figure 5-15. *Influence of the rate of compression on the stress in the Buffer swelling test.*

Influence of block strength

Figure 5-16 shows a comparison between the measured stress in the Buffer swelling test and corresponding results from 3DEC models with either linear elastic blocks (E) or linear elastic blocks with Mohr-Coulomb shear strength (MC). The deformations in the models appear to be primarily elastic until about 80 mm of deformation in agreement with the measurements. The onset of failure (after 80–100 mm of deformation) appears to be adequately captured by the MC-model. Note that the Mohr-Coulomb block material model in 3DEC is formulated such that the cohesion does not drop to a residual value after shear failure is initiated. This explains why the post-failure evolution does not agree with the measurements.

Comparison between modelled and measured deformations of blocks and gaps

Figure 5-17 shows a photograph of the block stack taken during the dismantling of the Äspö field test alongside modelling results of the vertical displacements in a vertical cross-section through the centre of the model and corresponding gap deformations after 80 mm of compression (the last modelling step where the linear elastic approximation of the blocks is valid, cf Figure 5-16). Note that the observations from the tests and the results from the model do not correspond to the same point in time during the loading sequence meaning that a clear correlation between observations and modelling results cannot be made. The comparison between observations and the 3DEC model is, therefore, mainly included here for completeness.

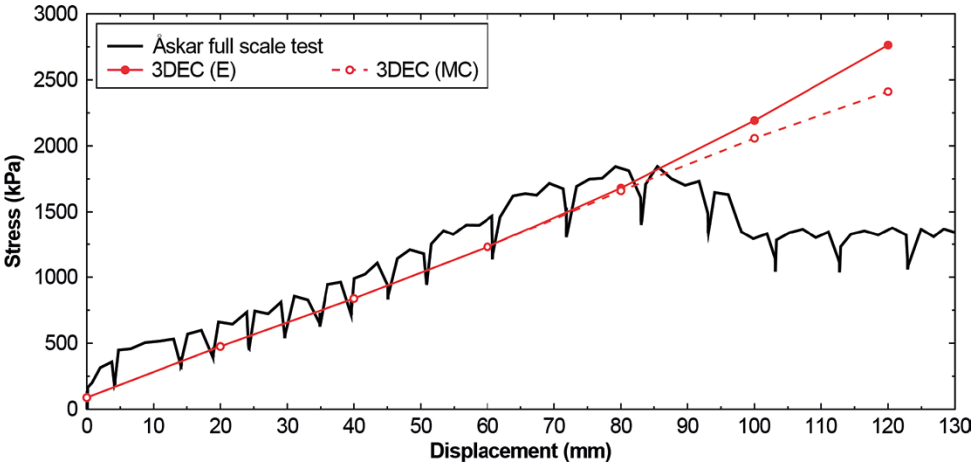

Figure 5-16. *Comparison between the measured stress in the Buffer swelling test at Äspö HRL (Åskar full scale test) and corresponding results obtained in the 3DEC models with either linear elastic blocks (E) or linear elastic blocks with Mohr-Coulomb shear strength (MC).*

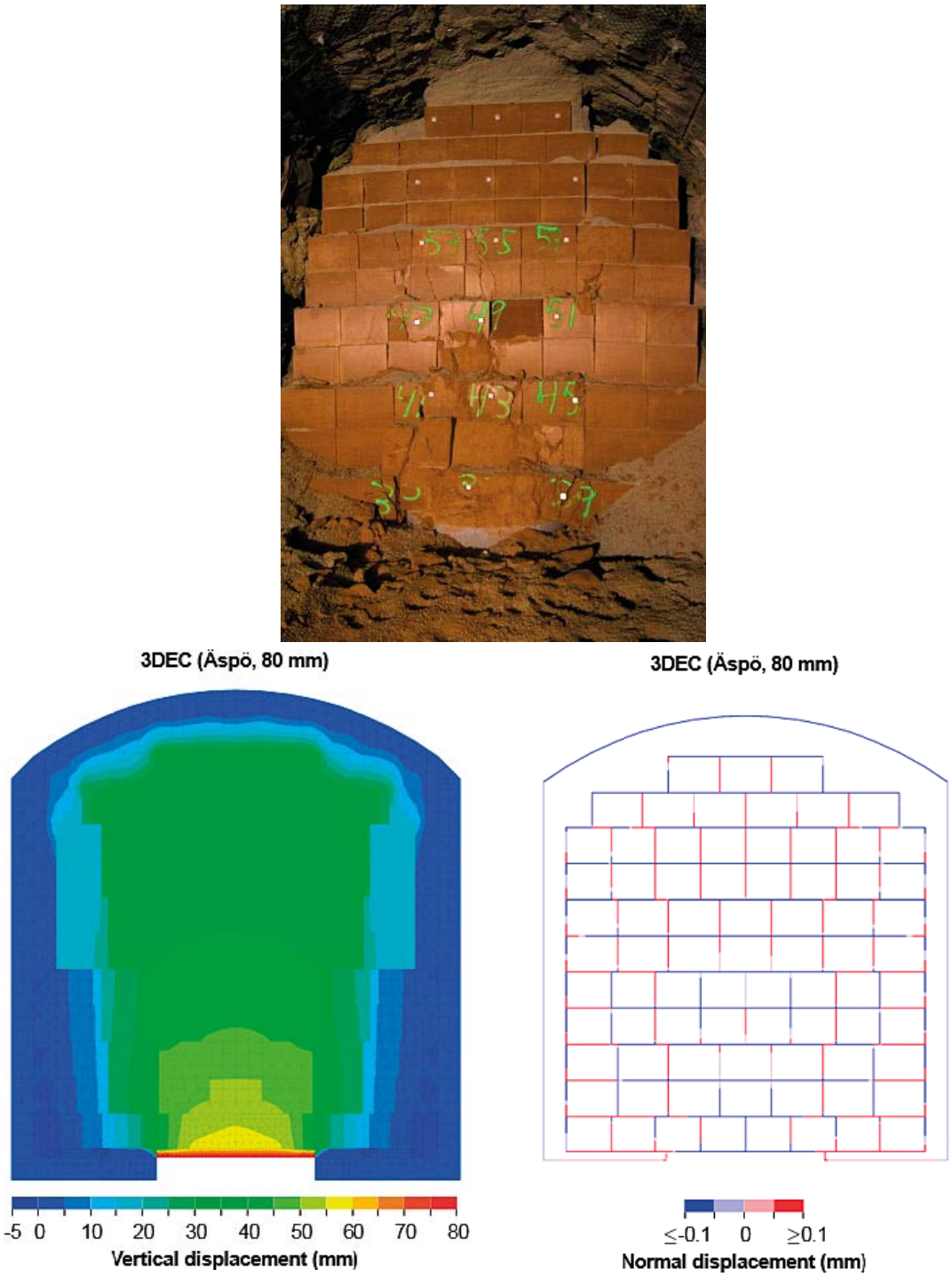

Figure 5-17. *Top: Photograph of the block stack taken during the dismantling of the Äspö field test (redrawn from Sandén et al. (2017, Figure 4-17)). Bottom left: Distribution of vertical displacements after 80 mm of deformation in a vertical cross-section through the centre of the model. Bottom right: Corresponding view of the normal displacements of the gaps between the blocks (red colours indicate an opening of the gaps).*

5.4 Potential for upscaling

The lab-scale test was made at a scale of 1:20 compared with the full scale. To test if the stress-displacement relation obtained in the lab-tests can be upscaled to full scale, the measurements and corresponding best-fit linear elastic model results from the lab-test (with displacements multiplied by 20; the stress results are not compensated for gravity) are compared with the measurements and corresponding model results of the Äspö field test. For completeness, a small-scale model was also analysed with the same property values as in the full-scale test. The results from the three models are presented in Figure 5-18.

The results from the full-scale experiment indicate that the resistance to upwards swelling is higher than in the upscaled lab-scale experiment despite having individual components (i.e., pellets, blocks and gaps) that are less stiff than in the lab-test. However, if the weight of the stack and the thickness of the pellet filling in the floor are considered, the agreement will be quite good (see also Section 3.6.5). The upscaled model with the same properties as in the full-scale test has the least resistance to upwards swelling of the three models. There are two main differences between the models with Äspö properties (lines with filled red or blue plot markers) that could explain the different response to loading: (1) the thickness of the pellets in the floor and (2) the size of the blocks and their stacking pattern (that would affect the effective compliance of the block stack).

To investigate if the difference in mechanical response to loading can be explained by differences in the deformation patterns, the vertical displacements after 80 mm of compression (4 mm upscaled to 80 mm in the lab-scale models) are presented in a vertical cross-section through the centre of the models, see Figure 5-19. There are large qualitative differences in the deformation patterns between the large-scale model and the two small-scale models. The large-scale model has a more uniform deformation pattern and it appear that the block stack is lifted to a larger extent than in the small-scale models. In the small-scale models, the deformations appear to be taken up by the pellets to a larger extent. Although the differences between the models primarily appear to be related to the thickness of the pellets in the floor, this should be investigated in future modelling work where the impact of the pellets geometry and block stacking patterns is studied in more detail.

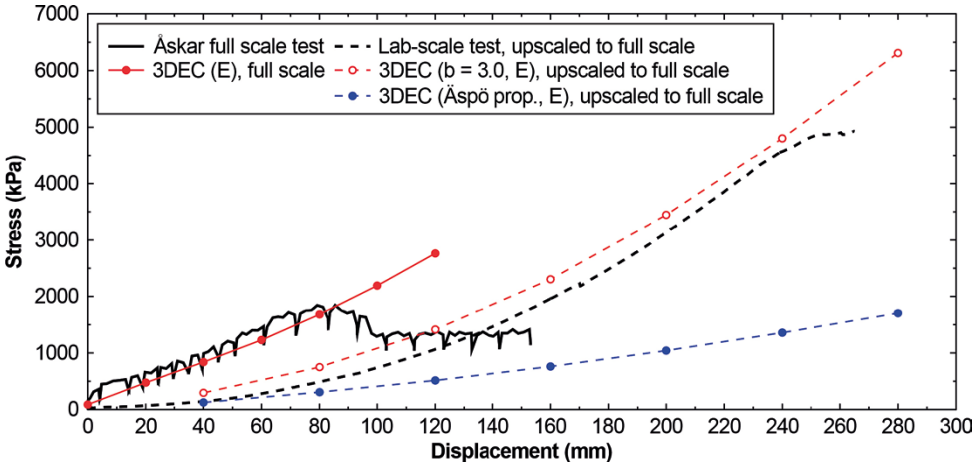

Figure 5-18. *Comparison between the Äspö field test (Åskar full scale test), the lab-scale test upscaled to full scale, and the lab-scale test analysed in 3DEC with Äspö properties and upscaled to full scale.*

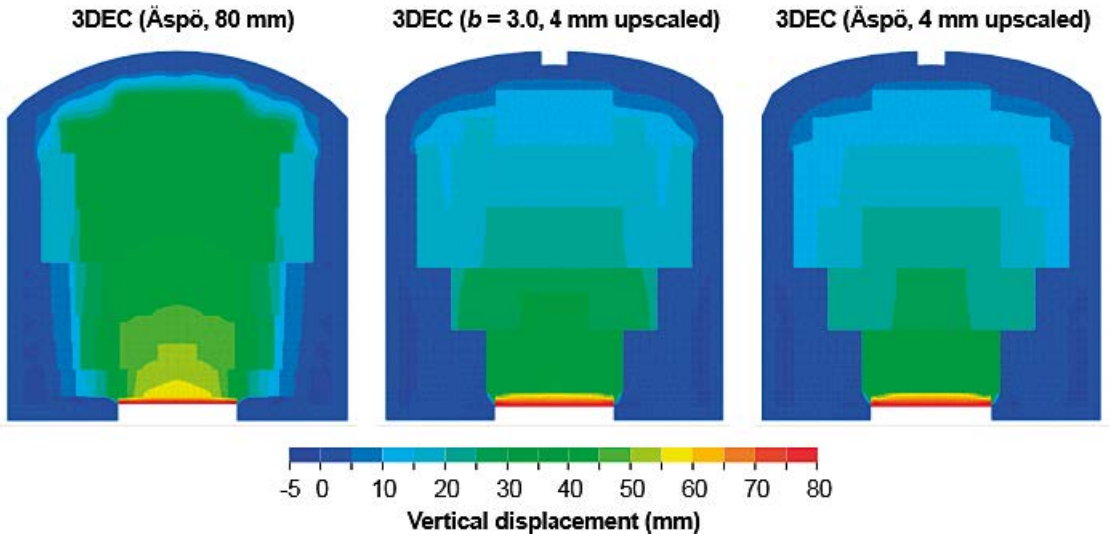

Figure 5-19. *Comparison between vertical deformations in a vertical cross-section through the centre of the model of the Äspö field test and two small-scale models with results upscaled to full scale: the dry lab-scale test and a model with the same property values as in the field test.*

5.5 Discussion and conclusions

In this study, the distinct element software 3DEC has been used to simulate (1) the dry tunnel test (small-scale) and (2) the Buffer swelling test in Äspö HRL (full-scale). Although the results from both experiments could be reproduced reasonably well numerically, there are a number of uncertainties regarding the small-strain approximation, boundary conditions (i.e., the compression speed), material models and parameter values. These uncertainties may need to be addressed in future studies:

- The small-strain approximation in 3DEC was used to avoid numerical problems in regions with very large strain such as the where the piston pushes against the pellets. The adequacy of this approximation for the type of problem considered in this study may need to be investigated in future work.
- The results were found to be sensitive to the rate at which the pellets material is compressed. Future work may include a systematic test to constrain the rate for different geometries and/or input data.
- The parameter values to the material model used to simulate the mechanical response of the pellets material should ideally be derived from isotropic triaxial compression tests (see Itasca 2016). It is unknown if the approach used here to determine the parameter values from oedometer tests over- or underestimates the actual values. More work can be done to constrain the input parameter values to the material model.
- The bentonite blocks were assumed to respond to loading as either linear elastic material or linear elastic material with Mohr-Coulomb shear failure. Note that the Mohr-Coulomb block material model in 3DEC is formulated such that the cohesion does not drop to a residual value after shear failure is initiated meaning that the post-failure evolution cannot be adequately captured by the models. In future studies, it may be necessary to develop the material model to account for such a drop in cohesion or to explore alternative material models e.g., the strain-hardening/-softening material model (Itasca 2016), in which the strength parameters can be set to vary with plastic strain.
- Stress-stiffness relations for the gaps between the blocks were derived for a normal stress up to about 1 MPa. To better constrain the input to the models, the block stack should be compressed to the full range of normal stress obtained in the experiment. For future studies, it also needs to be investigated if the gap-stiffness is the same between full-scale blocks and small-scale blocks considered in this study.

To conclude, the reasonable agreement obtained between modelling results and measurements in both the lab-scale test and the full-scale Buffer swelling test indicate that 3DEC is a suitable modelling tool for this type of problem. However, more work can be done to improve the general agreement between models and measurements and to test to what extent upscaling results from lab-scale to full scale is possible.

6 Deposition hole tests in scale 1:10

6.1 General

The buffer expansion/swelling upwards into the deposition tunnel has been investigated in tests performed in scale 1:10. In these tests, the resistance of the backfill against the buffer swelling has been simulated by springs, chosen to simulate the resistance determined in the full-scale test performed at Äspö HRL (Sandén et al. 2017). The influence of the buffer wetting situation on the upwards swelling has been an important parameter to investigate.

6.2 Test equipment

The simulated deposition hole consists of four tube sections that were bolted together, Figure 6-1. The access to water was made via filters placed on the deposition hole periphery. In order to simulate different wetting scenarios, two sets of the test equipment were manufactured:

1. Filter mats were placed along the whole deposition hole periphery (no filters were placed at the bottom of the deposition hole nor at the top).
2. Filters were placed at three different levels at the deposition hole periphery, see drawing provided in Figure 6-1. Each of the filter sections had their own inlet and outlet. It was thus possible to perform a test where only one of the filter sections was used. The bottom filter had a height of 50 mm while the other two had a height of 100 mm (note that in the performed test, only the bottom filter was used).

The filter mats were countersunk into the deposition hole walls which means that the inner diameter of the deposition hole always was 175 mm.

At the top of the buffer there was a piston that could be moved upwards. By making the resistance of the backfill as a function of the displacement upwards it was possible to simulate different backfill scenarios. The resistance against the buffer swelling was simulated by springs with a linear relationship between force and displacement. Above the springs, the total axial force and the axial displacement were registered by a loadcell and a strain gauge respectively.

The radial pressure was registered at three levels.

6.2.1 Scaling

The buffer expansion/swelling upwards into the deposition tunnel has been investigated in tests performed in scale 1:10. A compilation of data on the different components from the reference design and from the scale tests is provided in Table 6-1. As shown in the table, the height of the individual blocks was not exactly scaled. A schematic drawing of the test layout is provided in Figure 6-1. The two uppermost solid blocks are by definition part of the backfill but since they are judged to influence the results of this investigation, they have been included in the tests.

It should be noted that the bevel, located in uppermost part of the deposition hole in the reference design, has not been included in the scale tests.

Table 6-1. Compilation of data from the reference design and target data for the scale tests.

Component	Reference	Scale 1:10
Deposition hole		
Diameter, m	1.75	0.175
Area, m^2	2.405	0.024
Length, m	7 930	0.78
Canister		
Length, m	4.841	0.4835
Diameter, m	1.05	0.105
Ring shaped blocks		
Height, m	477.5	50
Outer diameter, m	1.65	0.165
Inner diameter, m	1.07	0.107
Bulk density, kg/m^3	2 057	2 057
Water content, %	17 ± 1	17 ± 1
Number	10	10
Solid blocks		
Height, m	540	50
Outer diameter, m	1.65	0.165
Bulk density, kg/m^3	1 987	1 987
Water content, %	17 ± 1	17 ± 1
Number	6	6
Pellets		
Bulk density, kg/m^3	970	970
Water content, %	15 ± 1	as delivered

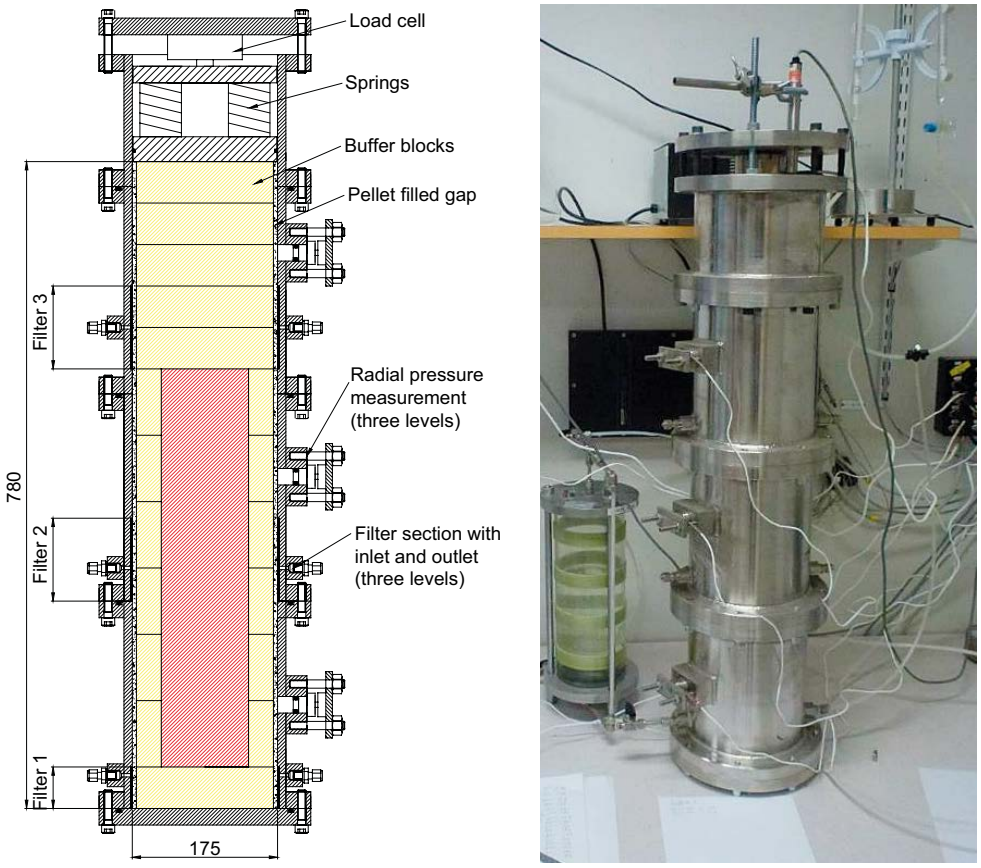

Figure 6-1. *Left: Schematic drawing of the test equipment. Right: Photo showing the complete test equipment after preparation.*

6.3 Material

6.3.1 Bentonite

The buffer blocks were manufactured using MX-80 bentonite from American Colloid Co. This material is one of SKB: s most studied bentonites.

6.3.2 Buffer block manufacturing

The water content of the raw material was adjusted to be 17 % before compaction. Two types of blocks were manufactured, see photo provided in Figure 6-2. The applied compaction pressure and the received average densities of the different block types are shown in Table 6-2.

Table 6-2. Applied compaction pressure and received average densities of the different block types.

	Comp. pressure, MPa	Test 1 (BU1_D)		Test 2 (BU5_E3)	
		Bulk density kg/m^3	Dry density kg/m^3	Bulk density kg/m^3	Dry density kg/m^3
Rings	40	2030	1721	2056	1742
Blocks	25	1991	1688	2007	1701

The blocks were manufactured in two different moulds. All block measurements were after compaction as intended except for the outer diameter that was turned from 175 to 165 mm.

6.3.3 Buffer pellets

The buffer pellets are difficult to scale, and it was therefore decided to crush pellets to a size between 1 to 4 mm. The water content of the simulated pellets was 10 %.

6.3.4 Water

The water used in the test had a salinity of 1 % by weight (50/50, Na/Ca).

Figure 6-2. *Photo showing the two types of buffer blocks.*

6.4 Test matrix

Two deposition hole tests in scale 1:10 were performed. In both tests, the resistance of the backfill against the buffer swelling was simulated by springs chosen to simulate the resistance determined in the full-scale test performed at Äspö HRL (Sandén et al. 2017). The difference between the two tests was the wetting scenarios:

- **Test 1 (BU1_D)**. In the first test the buffer had access to water via filters positioned along the entire deposition hole periphery (not the bottom of the deposition hole nor the top). The applied water pressure was 10 kPa during the first seventy days and was then increased to 100 kPa.
- **Test 2 (BU5_E3).** In the second test the buffer had access to water from a filter placed at the deposition hole periphery at the lowest 50 mm i.e., at the height of the bottom block, see drawing provided in Figure 6-1. No water pressure was applied during the first seventy days (the filter had access to water from a vessel with the surface at the same level as the filter). The water pressure was after seventy days increased to 10 kPa (one-meter water column).

The names of the two tests, BU1_D and BU5_E3, origins from a pilot study were several different wetting scenarios were considered.

6.5 Implementation

6.5.1 Preparation of the tests

The preparation of the test equipment consisted of the following steps (see drawing provided in Figure 6-1 and photos provided in Figure 6-3):

1. Installation of filter mats.
2. Mounting of the bottom lid on the bottom steel tube.
3. Installation of the bottom block and thereafter the pellets surrounding this block.
4. Installation of the first ring-shaped blocks. Pellets were installed after positioning of every single block.
5. Installation of the canister, which was made of stainless steel.
6. Mounting of the upper steel tubes.
7. Continued installation of ring-shaped blocks (10 pcs in total) together with pellets.
8. Installation of the cylindrical blocks (5 pcs).
9. Installation of piston on top of the bentonite.
10. Installation of springs and the uppermost steel plate.
11. Mounting of load-cells and displacement sensor (the displacement sensor is mounted through a hole in the uppermost steel plate, see right photo in Figure 6-1.

6.5.2 Water saturation phase

Tubes were connected to the water inlets, which in turn had connection to the filter mats. The tube ends were then connected to one tube feeding the whole test with water.

Test BU1_D: Water was filled up from the bottom of the deposition hole until coming out at the uppermost positioned water inlet/outlet. The inlet tube was thereafter connected to a burette. The applied water pressure was 10 kPa during the first seventy days and was then increased to 100 kPa.

Test BU5_E3: The buffer had access to water from a filter placed at the deposition hole periphery at the lowest 50 mm i.e., at the height of the bottom block. The filter had access to water from a vessel with the water surface at the same level as the top of the lower filter. The water pressure was after 125 days increased to 10 kPa (one-meter water column).

Figure 6-3. *Photos taken during the assembling of the deposition hole tests. Upper left: The bottom block and the first two ring-shaped blocks are installed together with the canister. Upper right: Close-up showing the pellet filling between block and test cell wall. Lower left: The last ring-shape block is installed. Lower right: The springs installed at the top of the deposition hole. The springs simulate the resistance from the backfill during the buffer swelling.*

6.6 Results

6.6.1 Preparation

The measured average installed density for both tests is presented in Table 6-3 together with the calculated amount of water needed to reach full saturation and the calculated final density at saturation.

Table 6-3. Table showing the average installed dry density in the deposition hole, the water needed to reach saturation and the calculated average density at saturation.

Test	Installation	Test phase	
	Average dry density kg/m^3	Water for saturation liters	Density at saturation kg/m^3
BU1 D	1 556	2.68	1 998
BU5 E3	1 593	2.43	2 022

6.6.2 Water uptake

The two deposition hole tests in scale 1:10 were running for 349 (BU1_D) and 405 (BU5_E3) days respectively. The water uptake was regularly registered for both tests during the test time, see graphs provided in Figure 6-4.

Test BU1_D has taken up in total 2.75 liters, see the upper graph in Figure 6-4. The main part of the water uptake occurred during the first three months and after that the water uptake rate was very low. The calculated amount of water needed for complete saturation of the test was 2.68 liters. Considering the axial swelling of the buffer in this test, see data provided in Section 8.6.3, 2.97 liters should be needed for complete saturation. There is a clear increase of the water uptake after about seventy days. This depends on an increase of the applied water pressure from 10 to 100 kPa.

Test BU5_E3 has taken up in total 0.76 liters, see lower graph in Figure 6-4. About half of this amount was taken up during the first month and after that the water uptake rate has been almost constant. The small jump in the curve on day 50 is believed to depend on trapped air that suddenly had been released from the filter. The calculated amount of water needed for complete saturation of the test was 2.46 liters. Considering the axial swelling of the buffer in this test, see data provided in Section 8.6.3, 2.59 liters should be needed for complete saturation. The applied water pressure was increased to 10 kPa after 125 days test.

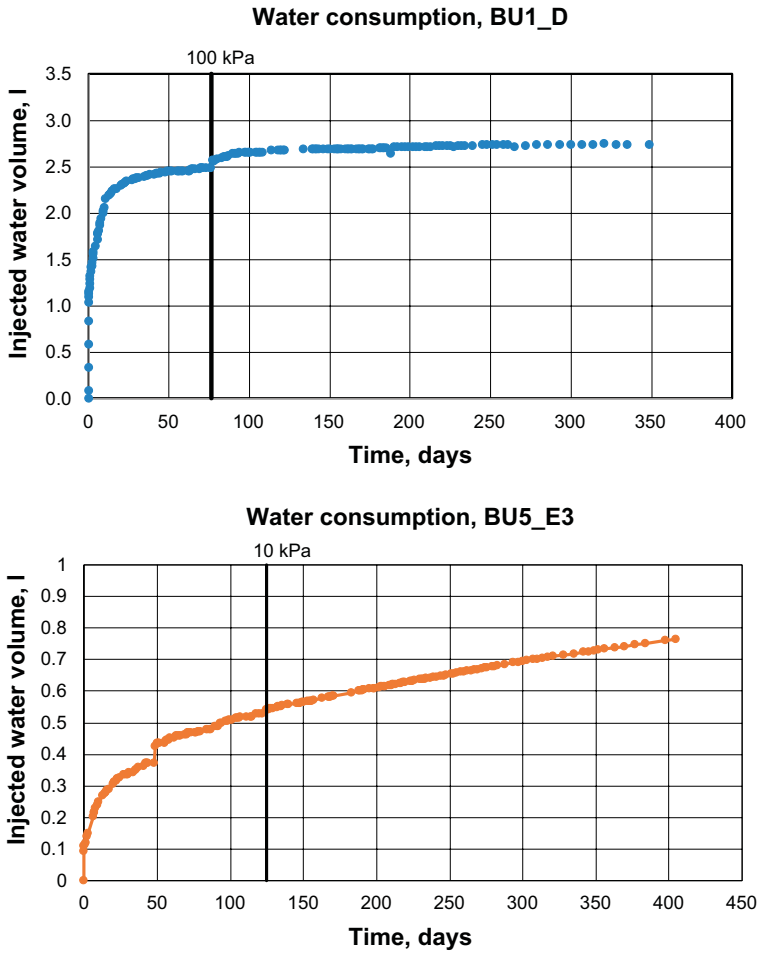

Figure 6-4. *Upper: Water consumption plotted versus time for Test BU1_D. Lower: Water consumption plotted versus time for Test BU2_E3.*

6.6.3 Buffer swelling and displacement

The following was measured and registered for both tests:

- Axial swelling pressure at the top of the deposition hole.
- Axial displacement at the top of the deposition hole.
- Radial pressure was registered at three different heights, see Figure 6-1.

The results from these measurements are presented in graphs provided in Figure 6-5.

The axial displacement for Test BU1_D was in total 11.7 mm during the test time (350 days). At the time for dismantling, there was still a small increase in axial swelling with time. The axial pressure had at the time for termination reached a pressure of about 2.5 MPa. The radial pressure was similar at all three levels, between 3.5 to 4 MPa.

The axial displacement for Test BU5_E3 was in total 5.7 mm during the test time (410 days). At the time for dismantling, the main part of the buffer was still unsaturated, which means that both axial and radial swelling pressure together with the axial displacement was still increasing with time. The axial pressure had at the time for termination reached a pressure of almost 1 MPa. The radial pressure was about 800 kPa at the lowest level (closest to the water inflow) and below 100 kPa at the other two levels.

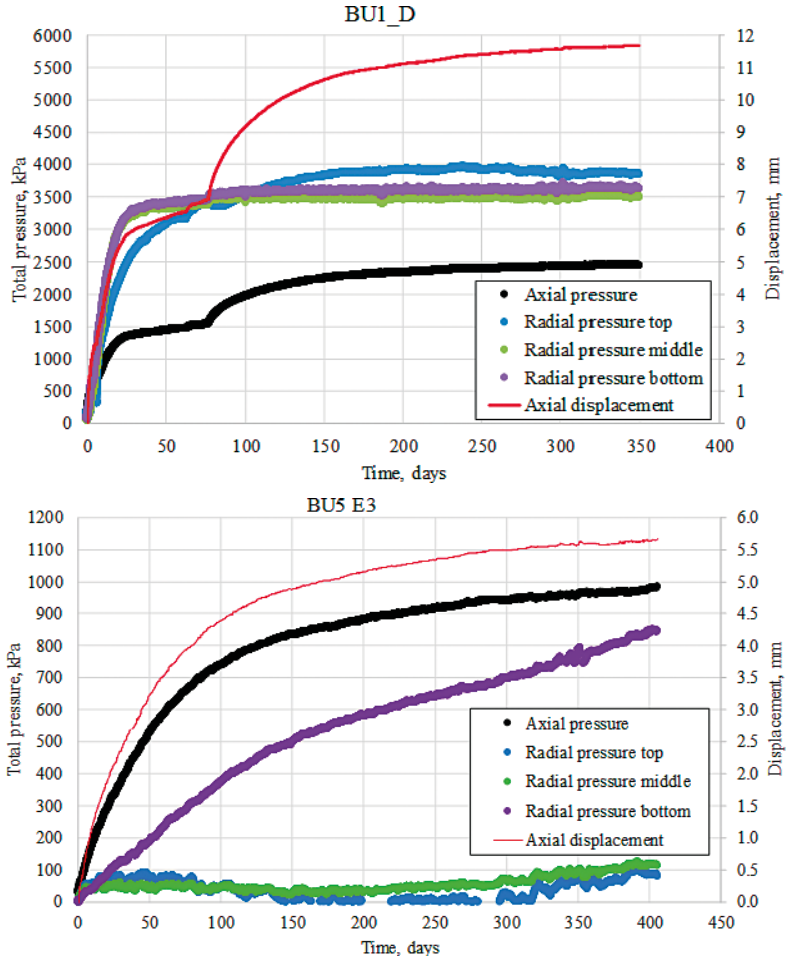

Figure 6-5. *Upper: Radial swelling pressure, axial pressure and axial displacement for Test BU1_D plotted versus time. Lower: Radial swelling pressure, axial pressure and axial displacement for Test BU2_E3 plotted versus time.*

6.6.4 Comparison with full scale

In the deposition hole tests, springs were used to simulate the resistance from the backfill, see description in Section 6.1 and photo provided in Figure 6-3. The springs were chosen so that the resistance should be scaled down from the results of the Buffer swelling test performed at Äspö HRL (Sandén et al. 2017). The theoretical relationship between pressure and displacement obtained from the full scale test and then adapted to the current scale of the deposition hole tests (1:10) is provided in Figure 6-6 together with the registered data from the two tests. The inclination is similar for all three lines which indicates that the test conditions have been similar although the scales have been different.

6.6.5 Dismantling and sampling

Planning

The two tests were terminated after 349 (BU1_D) and 406 (BU5_3) days respectively. In conjunction with the dismantling a comprehensive sampling of the bentonite was performed. Samples were cut or sawed out at in total 228 positions in each of the tests, see sampling plan provided in Figure 6-7. The water content and the density were determined at every position.

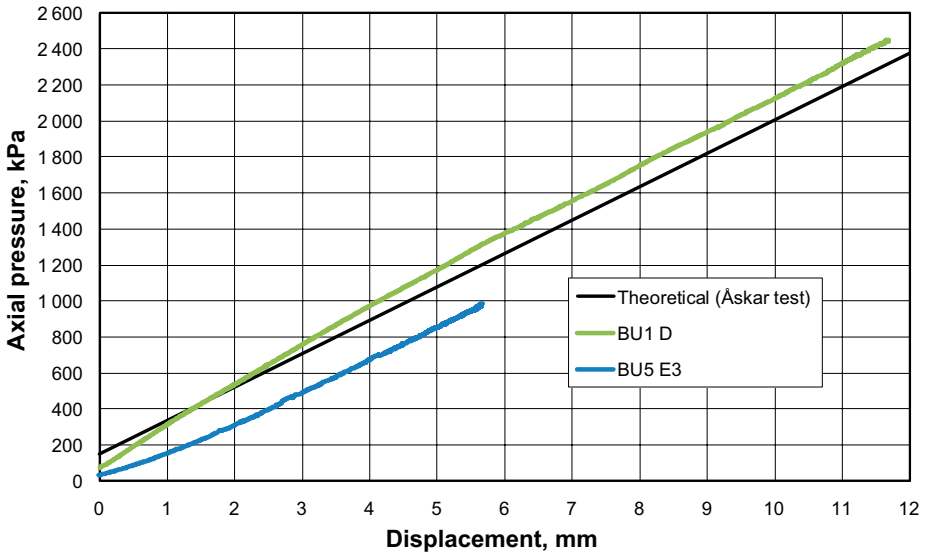

Figure 6-6. *Axial pressure plotted versus displacement for the two performed tests and for the theoretical scaled relationship obtained from the full scale test performed at Äspö HRL.*

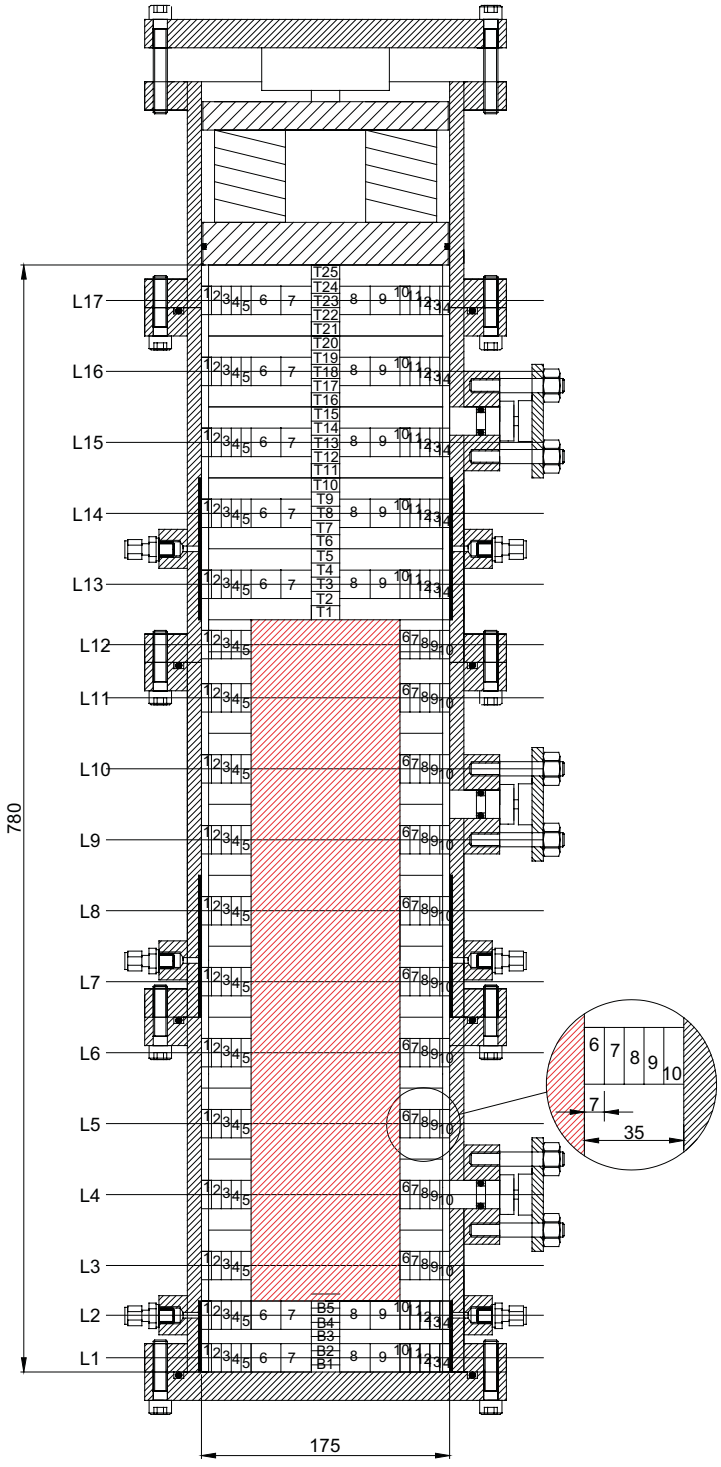

Figure 6-7. *Schematic drawing showing the positions where samples were taken.*

Technique

The test equipment consists of four tube sections simulating the deposition hole, see Figure 6-1. The dismantling started from the top of the "deposition hole" with removal of the uppermost tube section. The bentonite in each steel tube section was pushed out from the steel tube using a hydraulic piston, Figure 6-8. It was for both tests possible to detect the block boundaries between the different blocks, which facilitated the sampling.

After having performed a rough division of every single block by hammer and chisel, a band saw was used to cut the block into small pieces, Figure 6-9.

Figure 6-8. *A hydraulic press was used to push out the bentonite from the test tubes.*

Figure 6-9. *Samples were cut out from each of the sampling sections using a band saw.*

Dismantling of Test BU1_D

Photos taken during dismantling of the test are provided in Figure 6-10. One photo (upper left) shows the inside of the tube section above the canister. The upper photo to the right shows the removal of the filer surrounding the blocks in a steel tube section. Note the hole in the filter located where the piston from one of the radial pressure measurements has been placed. As mentioned earlier it was for both tests possible to detect the former block boundaries between the different blocks, which facilitated the sampling, see photo in Figure 6-10, lower left. The lower photo to the right shows that at some locations there was like a shell consisting of the former pellet filling. At some positions this shell had separated from the blocks.

An interesting observation was that the cylindrical blocks above the canister were all slightly bended, see photos provided in Figure 6-11. The difference in height between the outer periphery and the center of the block was about 2 mm.

Figure 6-10. *Photos taken during dismantling of BU1_D.*

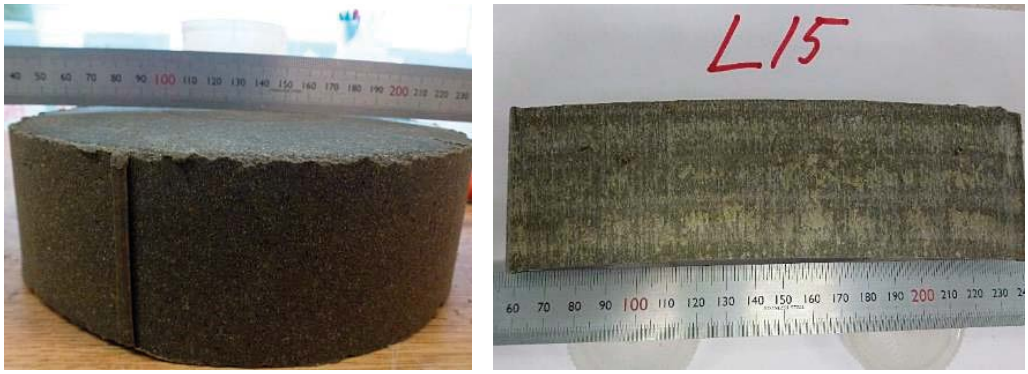

Figure 6-11. *The cylindrical blocks above the canister were clearly bended. The photo shows block the third block above the canister. The left photo shows the complete block and the left photo shows a cross section that has been sawed out.*

Dismantling of Test BU5_E3

The dismantling of this test was much easier since large parts of the bentonite were more or less unaffected of water (this test had only access to water from a filter placed at the bottom block periphery) and it was therefore easy to remove most blocks manually. The photos provided in Figure 6-12 show the first cylindrical block above the canister (left) and the last ring-shaped block (right). Both these blocks and the surrounding pellet filling were visually unaffected of water.

The photos provided in Figure 6-13 show the second ring-shaped block from bottom (left). The pellet filling at this level is clearly affected by some water uptake, but it is still possible to rather easily remove the pellets from the block surface. The right photo shows the first ring-shaped block from bottom. The pellets surrounding this block have taken up water and are "glued" to the block surface.

The bottom block was visually completely saturated. The height of this block was measured with a digital caliper to 56 mm i.e., all axial swelling that was registered during the test time, Figure 6-5, seems to had taken place in this block.

Figure 6-12. *Left: The first cylindrical block above the canister, and the surrounding pellets, were visually unaffected of the wetting from the bottom of the deposition hole. Right: Photo showing the uppermost ring-shaped block. This block was also visually unaffected.*

Figure 6-13. *Left: Photo showing the second ring-shaped block from bottom. Right: The first ring-shaped block from bottom.*

6.6.6 Results from sampling

The results from the measurements of water content and density of Test BU1_D are presented as contour plots in Figure 6-14. The water content varies between 27 and 38 %. The parts with lowest water content are located at the center of the bottom block below the canister and the parts with highest water content are located at the periphery in the former pellet filled slot. This corresponds well with the density determinations, see the right plot in Figure 6-14. The highest density can be found in the bottom block while the lowest are found in the former pellet filled slot. The registered axial swelling/displacement 11.8 mm, see Figure 6-5, seems to have taken place almost evenly along the canister and at the cylindrical shaped blocks above the canister while the bottom block only has swelled in radial direction.

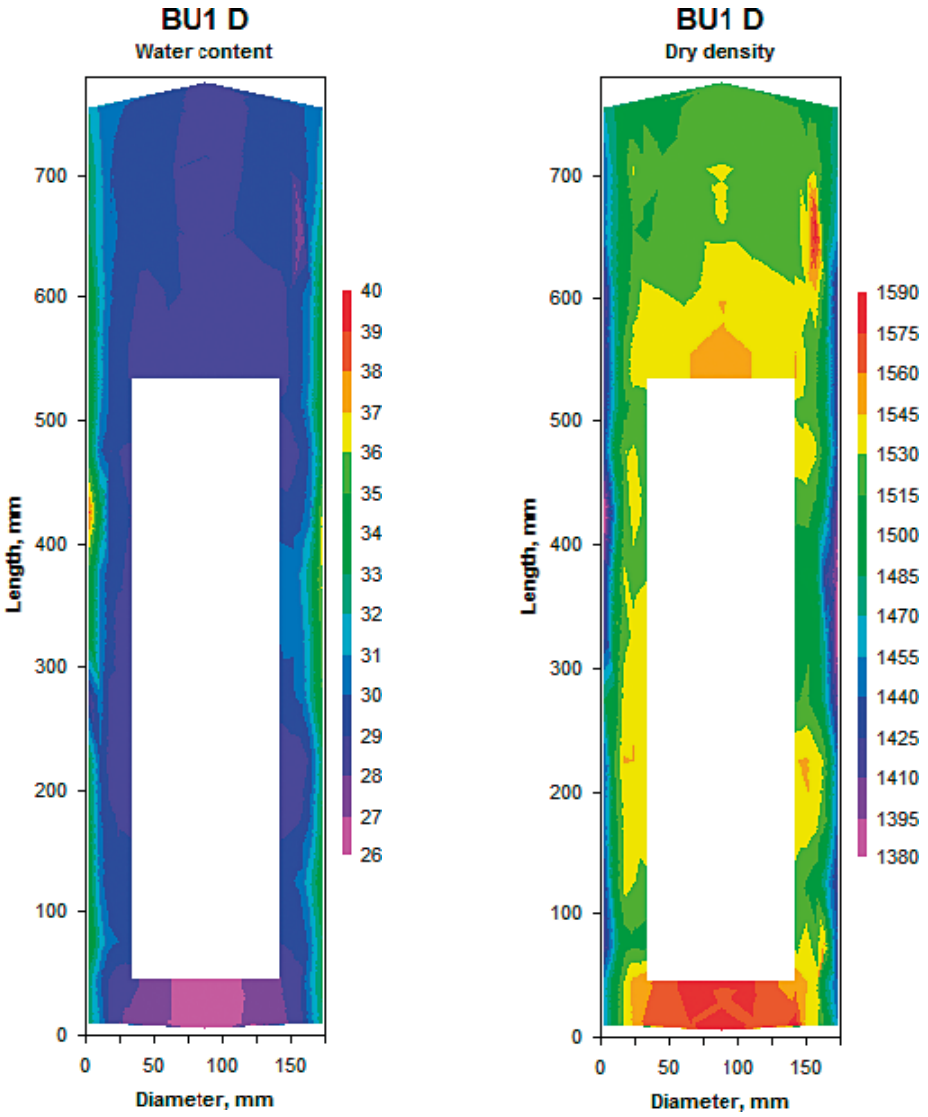

Figure 6-14. *Results from sampling of Test BU1 D. Left: Water content distribution in a cross-section of the deposition hole. Right: Dry density distribution in a cross-section of the deposition hole.*

The results from the measurements of water content and density of Test BU5_E3 are presented as contour plots in Figure 6-15. The water content varies between 16 and 36 %. Since the bentonite in this test only had access to water from the periphery of the bottom block below the canister, large parts of the bentonite along the canister and above the canister are more or less unaffected of water. As shown in Figure 6-15 (right), the main swelling has taken part in the bottom block where the dry density has decreased from 1 715 kg/m^3 at the time for installation to between 1 400 to 1 500 kg/m^3. It can also be seen in the figure that the blocks from about mid-height of the canister and up to the top are completely unaffected and thus have the same density as they had at installation. The registered axial swelling/ displacement was about 5.7 mm, see Figure 6-5, and seems to has taken place only by swelling of the bottom block.

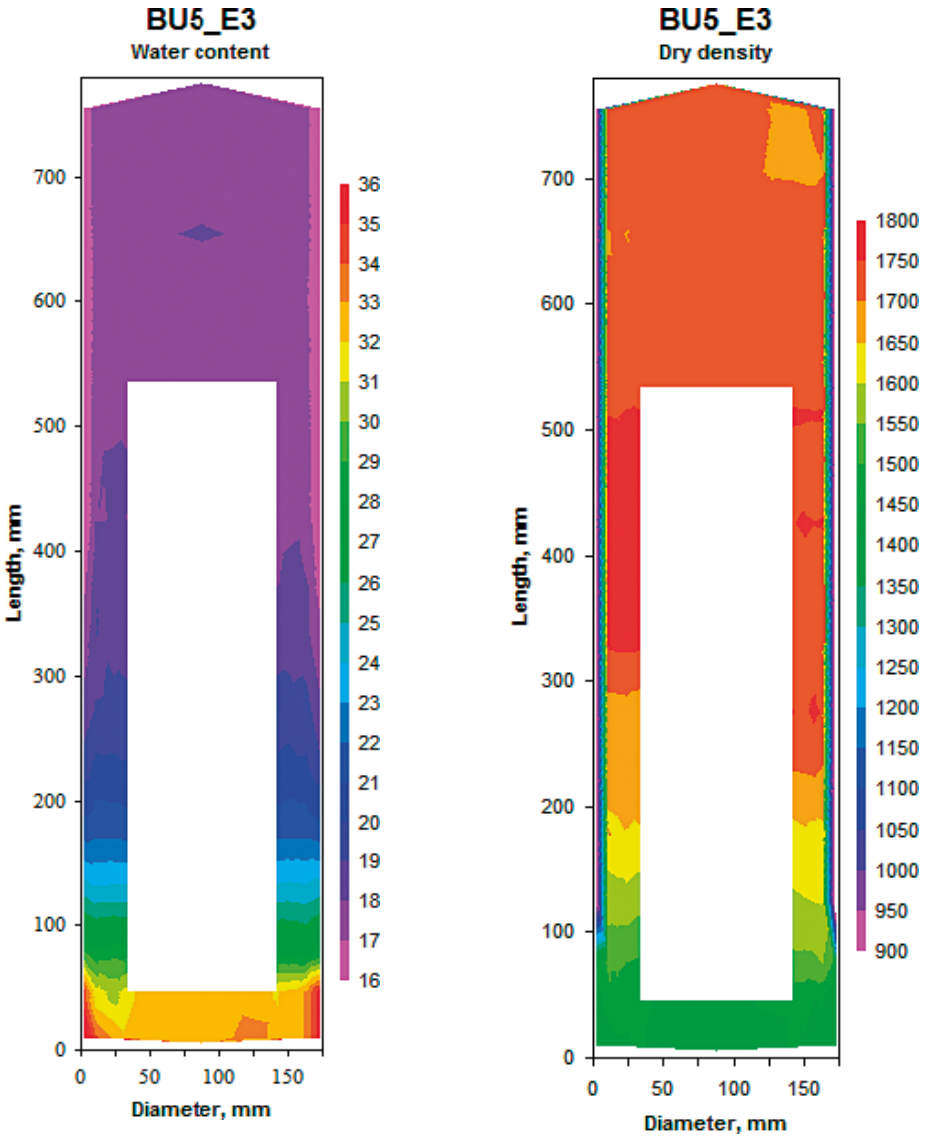

Figure 6-15. *Results from sampling of Test BU5_E3. Left: Water content distribution in a cross-section of the deposition hole. Right: Dry density distribution in a cross-section of the deposition hole.*

The results from the determinations of the dry density are also presented in two graphs provided in Figure 6-16. Here, the dry density distribution across the deposition hole diameter is presented for several different levels in the deposition hole, the bottom block, along the canister and above the canister. Logically, block 13 above the canister has lower density than the block below the canister and block 17 (uppermost block) has the lowest density and has thus swelled more than the other ones.

The graphs show that the saturation and homogenization has proceeded far in the BU1_D test while there are still large differences in both water uptake and the following swelling/homogenization in the BU5_E3 test.

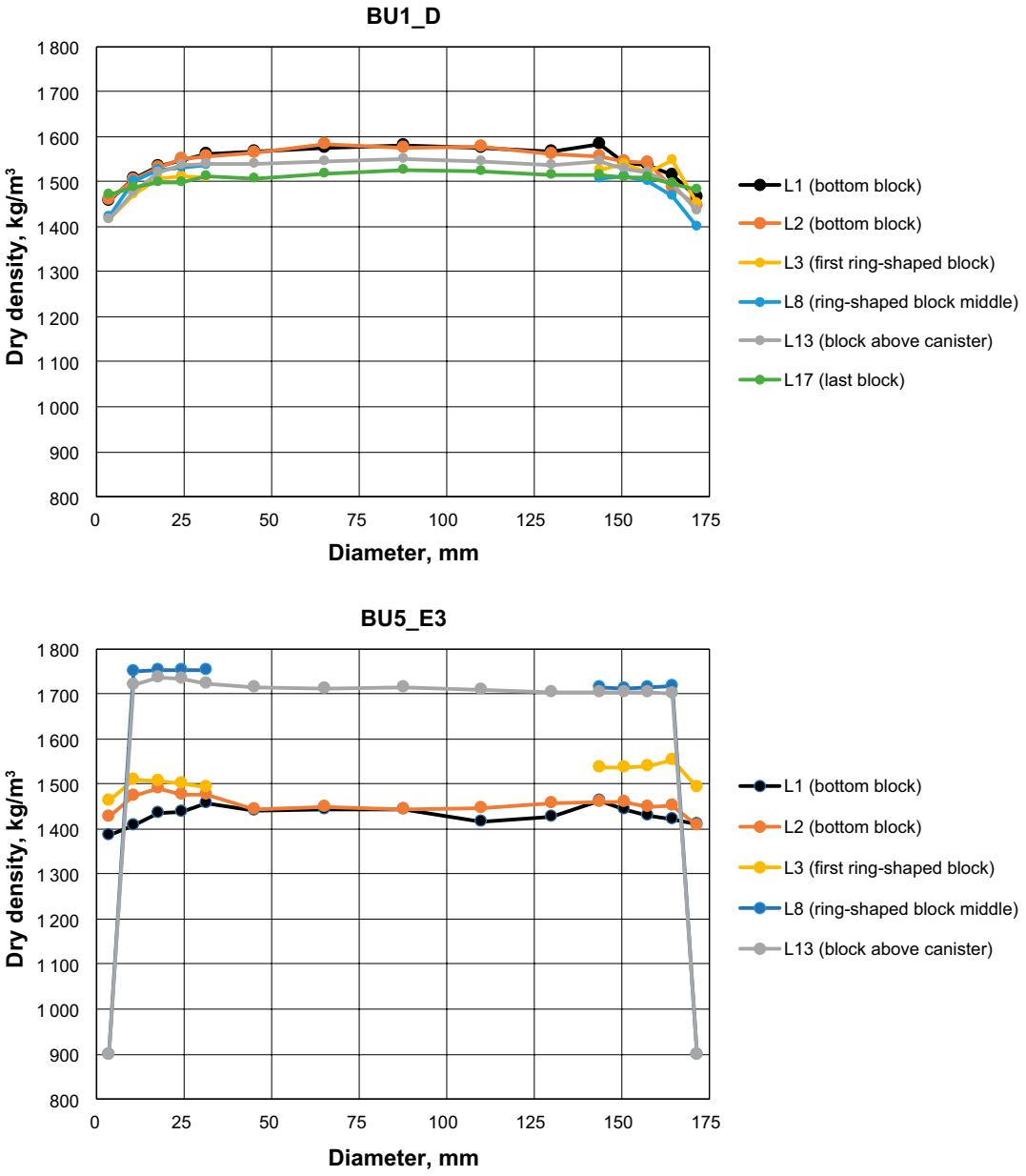

Figure 6-16. *Graphs showing the dry density distribution over the deposition hole diameter for the two tests. Data is presented for different levels: L1 and L2 (bottom block), L3 (first ring-shaped block), L8 (ring-shaped block middle), L13 (block above canister) and L17 (top block).*

6.6.7 Evaluation

A superficial evaluation will be done here. The large amount of information can be used for deeper analyses.

Test BU1_D

The degree of saturation calculated for each sampling position in BU1_D is presented in Figure 6-17 (left). As shown in the graph, the degree of saturation is very close to 100 % at all positions. The small variations depend probably on the fact that the water content and the density at each measuring point is not determined on the same sample, but on neighbouring samples. The scatter is therefore considered to be largely due to experimental uncertainties rather than indicating real variations in the degree of saturation. It is concluded that all bentonite in this test is saturated.

The swelling pressure potential corresponding to the determined dry density has been calculated for each sampling position according to the relation between dry density and measured swelling pressure at volume constancy given by Åkesson et al. (2010). The results are presented as a contour plot in Figure 6-17 (right). The lowest swelling pressures, 1.5 to 3 MPa can be found in the former pellet filled slot between blocks and deposition hole walls. The swelling pressures in the buffer block positions along the canister and in the cylindrical shaped blocks above the canister are mainly between 4 and 5 MPa, while the swelling pressure in the bottom block has been calculated to between 5 and 6 MPa. These figures should be compared with the registered swelling pressure at the time for dismantling, see graphs provided in Figure 6-5. The registered axial pressure was about 2.5 MPa which is considerably lower than the calculated 4 MPa. This depends probably on friction between the bentonite and the deposition hole walls and that the swelling pressure after swelling is lower than at constant pressure, which decreases the axial pressure. The registered radial pressure was between 3.5 to 4 MPa at all three levels. The calculated pressure is 4 to 5 MPa in the main part of the blocks and between 1.5 to 2.5 in the former pellet filled slot. During saturation/homogenization the pellet filled slot is compressed by the swelling buffer blocks and the pressure that is registered on the deposition hole walls is closer to what is calculated for the density in the blocks. This also reflects the difference in swelling pressure between swelling and compression and the influence of the direction of the swelling.

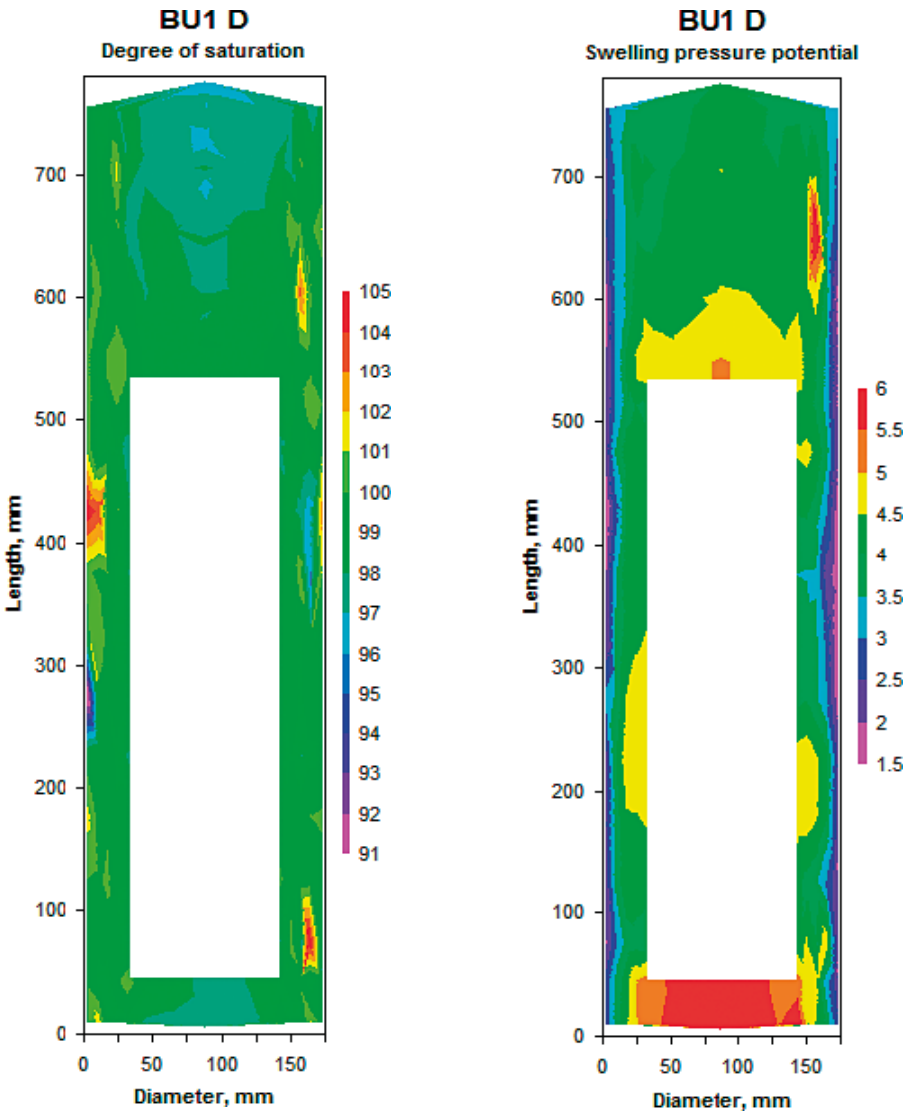

Figure 6-17. *Left: Degree of saturation distribution in a cross section of Test BU1_D. Right: Calculated swelling pressure distribution in a cross section of Test BU1_D.*

Test BU5_E3

The degree of saturation calculated for each sampling position in BU5_E3 is presented in Figure 6-18. As shown in the graph, the degree of saturation varies strongly. Full saturation is reached only in the bottom block below the canister. The first five ring shaped blocks are, however, also somewhat affected of the inflowing water. The water content in the first ring shaped block is about 28–29 % corresponding to a degree of saturation of 90–98 %, while the fifth ring shaped block has a water content between 18.4 % (pellets) and 19.5 % corresponding to a degree of saturation of 24–92 % (the low degree of saturation 24 % is a consequence of the low water content and low density of the pellet filling in the dry parts).

As for Test BU1_D, the swelling pressure potential corresponding to the determined dry density has been calculated for each sampling position in Test BU5_E3. The results are presented as a contour plot in Figure 6-18 (right). These swelling pressures are fictive since they correspond to the swelling pressure at full water saturation and most parts are dry. The swelling pressure, 1.5 to 3 MPa is noted in the bottom block. The axial swelling pressure recalculated from the measured force at time for dismantling, see graphs provided in Figure 6-5, was about 1 MPa which agrees fairly well with the calculated swelling pressure of the bottom block, 1.5 to 3 MPa. The canister and the blocks around and above are obviously pushed upwards and since there will be friction between buffer and deposition hole walls it seems reasonable with a somewhat lower axial pressure. The main reason is however judged to be the swelling pressure is measured at swelling and in the swelling direction as mentioned earlier. The registered radial pressure was 800 kPa at the lowest level and below 100 kPa at the two other levels. These measurements are all well in compliance with the corresponding calculated swelling pressures.

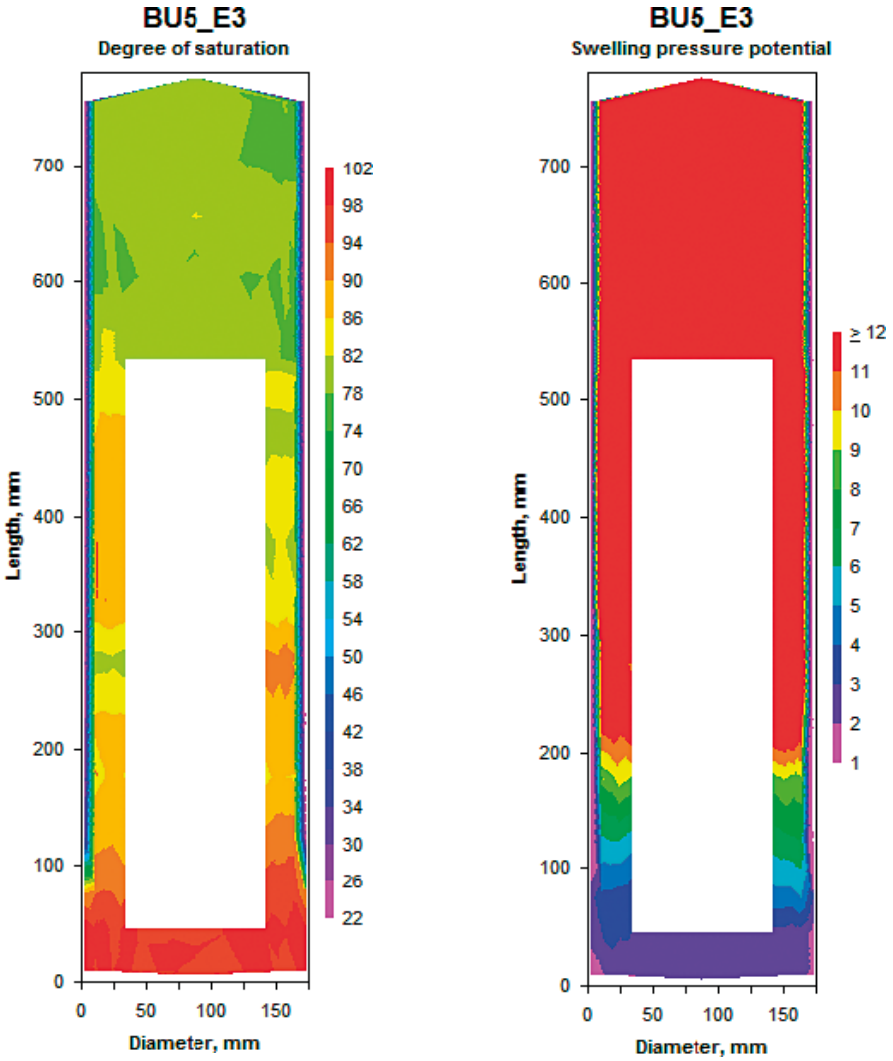

Figure 6-18. *Left: Degree of saturation distribution in a cross section of Test BU5_E3. Right: Calculated swelling pressure distribution in a cross section of Test BU5_E3.*

Density and swelling pressure in different sections

In addition to the local variation of the density and swelling pressure as shown in Figure 6-17 and 6-18, calculations have been made to determine average densities, both as average for the entire buffer volume up to and including the block above the canister according to the requirements, but also at different horizontal sections.

A compilation of the calculated test data is provided in Table 6-4:

- Column 1 and 2. Test no. and Section no.
- Column 3. Installed dry density of the different components (block and pellets). The density of the blocks and rings are taken as the average of all blocks and all rings.
- Column 4. The average dry density of the buffer volume (on which there are requirements, see Section 1.3) and of some sections of high interest at *installation*. These figures are weighted regarding volume at installation i.e., every block is measured and weighed, the pellets are weighed and the volumes of each component after installation are known.
- Column 5. The average dry density of the buffer volume (on which there are requirements, see Section 1.3) and of some sections of high interest at *excavation*. These values are derived as the average of each measured density weighed according to the volume that it represents in the block (a function of the radius of the location of the sample).
- Column 6. The calculated swelling pressure corresponding to the average weighted density at excavation. The data is presented for both the buffer volume (on which there are requirements) and for the different cross-sections in the two tests. The calculations are made according to Åkesson et al. (2010).

The average dry density at installation is 1 530 kg/m^3 for test BU1_D and 1 576 kg/m^3 for test BU5_E3 respectively. Corresponding figures determined after termination of the test are 1 505 kg/m^3 and 1 510 kg/m^3. The buffer in test BU1_D has thus decreased its density with only 25 kg/m^3 while the buffer in test BU5_E3 has decreased its density with 66 kg/m^3. The reason is of course that most of the swelling in test BU1_D has taken place in the upper blocks outside the requirement volume while the entire swelling in test BU5E_3 has taken place in the bottom block inside the requirement volume.

Table 6-4. Table showing the calculated average dry density for different sections of the two deposition hole scale tests.

Test	Section	Installed dry density (block/pellets) kg/m^3	Average dry density** (installation)	Average dry density** (excavation) kg/m^3	Swelling pressure*** (expansion) MPa
BU1_D	Buffer volume*	na	**1 530**	**1 505**	3.65
BU1_D	L1, bottom block	1 700/575	1 575	1 538	4.56
BU1_D	L2, bottom block	1 700/575	1 575	1 533	4.41
BU1_D	L3, first ring-shaped block	1 712/575	1 515	1 496	3.44
BU1_D	L8, ring-shaped block middle	1 712/575	1 515	1 485	3.19
BU1_D	L13, block above canister	1 700/575	1 575	1 512	3.83
BU1_D	L17, top block	1 700/575	1 575	1 503	3.60
BU5_E3	Buffer volume*	na	**1 576**	**1 510**	3.78
BU5_E3	L1, bottom block	1 700/778	1 598	1 429	2.18
BU5_E3	L2, bottom block	1 700/778	1 598	1 453	2.57
BU5_E3	L3, first ring-shaped block	1 734/778	1 568	1 512	3.83
BU5_E3	L8, ring-shaped block middle	1 734/778	1 568	1 534	4.44
BU5_E3	L13, block above canister	1 700/778	1 598	1 588	6.36

* These figures refer to the buffer volume on which there are requirements, see Section 1.3.
** The calculated average dry density is weighted regarding volume for the block/pellets density (installation) and for the density determined for each sample (excavation).
*** Calculated swelling pressure for the average dry density at excavation (Åkesson et al. 2010).

7 Modelling of the deposition hole tests

The main purposes of modelling the deposition hole tests were to:

- Develop models and investigate if the HM-processes and final state could be simulated properly for the deposition hole tests carried out in this project.
- Investigate the effect from using different water inflow locations and try to gain understanding about the underlying mechanisms.
- Show how the models can be utilized to investigate if certain safety criteria are fulfilled.

Much effort was spent setting up the material models properly, especially the mechanical material models of the buffer components where special interest has been directed towards the shearing properties.

7.1 Theory

The following description of the hydro-mechanical theory, on which Code_Bright is based, is a brief and less general version of what is given in Alcoverro and Alonso (2001). Constant temperature (T = 20 °C) and gas pore pressure (p_g = 0.1 MPa) have been used in the current simulations and no air was allowed to be dissolved into the liquid phase. Wherever these two variables appear in the formulation they should be considered constant.

The theory used in Code_Bright has its roots in a traditional geomechanical porous formulation, based on considering the material as a mixture of the constituents:

minerals,
liquid water,
dissolved air,
water vapor, and
dry air.

The constituents are divided in three *components* (i): minerals (m), water (w), and air (a) (the component belonging of entities is indicated by a superscript) and an assumption of three *immiscible phases* (α): solid (s), liquid (l), and gas (g) (the phase belonging of entities is indicated by a subscript) are made. The solid phase only consists of the mineral component, so the component superscript index (m) will not be written in the following.

From considering the structural assumptions of the mixture, following primitives may be defined:

mixture volume element (dv),
solid phase volume (dv_s),
liquid phase volume (dv_l),
gas phase volume ($dv_g = dv - dv_s - dv_l$), and
pore volume ($dv_p = dv - dv_s$).

Further primitives, regarding mass and energy are introduced for the constituents:

solid mass (dm_s),
water mass in liquid (dm_l^w),
water mass in gas (i.e., water vapor mass) (dm_g^w),
dry air mass in gas (dm_g^a).

With use of the primitives above the definitions below may be formulated:

porosity ($\phi = dv_p/dv$),
solid density ($\rho_s = dm_s/dv_s$),
liquid water mass per liquid phase volume ($\theta_l^w = dm_l^w/dv_l$),
water vapor mass per gas phase volume ($\theta_g^w = dm_g^w/dv_g$),
dry air mass per gas phase volume ($\theta_g^a = dm_g^a/dv_g$),
degree of liquid saturation ($S_l = dv_l/dv_p$), and
degree of gas saturation ($S_g = dv_g/dv_p$).

Below, e.g. when describing commonly used constitutive laws, functions that give values of variables are indicated with ~above the variable name.

7.1.1 Balance relations

The solid mass per mixture volume element can be expressed,

$$\frac{dm_s}{dv} = \frac{dm_s}{dv_s}\frac{dv - dv_p}{dv} = \rho_s(1-\phi)$$

and by using this as a basis, the balance equation,

$$\frac{\partial}{\partial t}\left(\rho_s(1-\phi)\right) + \nabla \cdot \rho_s(1-\phi)\frac{d\boldsymbol{u}}{dt} = 0\,,$$

can be derived. If the above is integrated, an updating scheme for the porosity is obtained,

$$J_s\rho_s(1-\phi) = {\rho_s}^0(1-\phi^0)\,,$$

where J_s is the determinant of the of the deformation gradient of the solid skeleton, $J_s = \det\left(\frac{\partial \boldsymbol{u}}{\partial \boldsymbol{X}}\right) + 1$, and the superscript ^{0} denotes initial values of variables.

The water mass per mixture volume element can be expressed as,

$$\frac{dm^w}{dv} = \frac{dm_l^w + dm_g^w}{dv} = \theta_l^w S_l\phi + \theta_g^w S_g\phi.$$

If introducing a source term f^w and fluxes of water in the liquid and gas phase, $\boldsymbol{j}_l^w$ and $\boldsymbol{j}_g^w$, the continuity equation,

$$\frac{\partial}{\partial t}\left(\theta_l^w S_l\phi + \theta_g^w S_g\phi\right) + \nabla \cdot \left(\boldsymbol{j}_l^w + \boldsymbol{j}_g^w\right) = f^w\,,$$

can be derived.

The used quasi-static formulation of the balance of momentum for the porous media reads,

$\nabla \cdot \sigma + \boldsymbol{b} = \boldsymbol{0}$,

in terms of total stress, σ, and body force, $\boldsymbol{b}$. As can be seen (from the absent inertia term), a mechanical equilibrium condition assuming an insignificant effect from inertia (i.e., quasi-static conditions), has been used. In the present formulation ordinary continuum mechanics sign conventions are used, i.e., stress components are positive for tensile conditions.

In addition to the balance equations, two equilibrium restrictions have been used. The mechanical and phase change equilibrium restriction are described in the next section.

In order to close the formulation, variables are selected as independent or dependent and material specific constitutive relations are specified where dependent variables are given by expressions of independent variables. The independent variables in Code_Bright are p_l and $\boldsymbol{u}$, the liquid pore pressure and displacement vector. Initial and boundary conditions are finally selected as completely specify the problem formulation.

It should here be mentioned that the liquid pore pressure loses its ordinary physical meaning for a bentonite type of material where the chemical potential governs the processes. For such materials the pore pressure could be considered an entity describing the material's water absorption potential.

7.1.2 Equilibrium restrictions

For the present systems accelerations are assumed insignificant. This *mechanical equilibrium condition* makes its appearance in the used quasi-static form of the balance of momentum.

The *phase change equilibrium* may be taken as manifested through the equality between chemical potentials of a constituent in different phases. Assuming phase change equilibrium for water and that the gas phase is a mixture of two ideal gases (air and water vapor) give the phase change equilibrium for water,

$$\tilde{\theta}_g^w(p_l, T) = \frac{\tilde{p}_g^w(T) M_w}{R(273.15 + T)} \exp\left(\frac{-(p_g - p_l) M_w}{R(273.15 + T)\tilde{\rho}_l(p_l, T)}\right).$$

In the expression above, the physical parameters molar mass of water, M_w, and the constant of gases, R, appear.

7.1.3 Constitutive relations

As mentioned earlier, to close the formulation, variables are selected as independent or dependent and material specific constitutive relations are specified where dependent variables are given by expressions of independent variables; in Code_Bright liquid pore pressure and displacement. Thus, liquid pore pressure and displacement become the unknowns to be solved for.

Porous medium relations

These constitutive relations describe interactions between constituents in various phases.

The degree of liquid saturation of the porous medium is related to the liquid pore pressure by use of a *retention law*,

$S_l = \widetilde{S}_l(p_l)$.

The degree of gas saturation is given by,

$\widetilde{S}_g(p_l) = 1 - \widetilde{S}_l(p_l)$.

The mass fluxes are additively decomposed in terms of a non-advective (diffusive), $\boldsymbol{i}_\alpha^i$, and an advective, $\theta_\alpha^i \boldsymbol{q}_\alpha$, contribution, according to,

$\boldsymbol{j}_\alpha^i = \boldsymbol{i}_\alpha^i + \theta_\alpha^i \boldsymbol{q}_\alpha$, $\alpha = l, g$ $\quad i = w, a$ without the combination $\alpha, i = l, \alpha$.

The *advective* mass fluxes include the phase velocity, $\boldsymbol{q}_\alpha$, which for the liquid typically is given by Darcy's law, schematically given by,

$\boldsymbol{q}_l = \widetilde{\boldsymbol{q}}_l(p_l)$.

and which for the gas phase becomes zero since the pressure is taken to be constant in the present work. Darcy's law is obtained from a combination of balance of momentum of the fluid phases together with constitutive assumptions of momentum exchange with other phases.

Diffusive (or non-advective) mass fluxes are usually described by Fick's law, schematically given by:

$\boldsymbol{i}_g^w = \widetilde{\boldsymbol{i}}_g^w(\theta_g^w)$,

in the case of the water vapor. Fick's law is obtained by consideration of: the constituent balance of momentum, the phase balance of momentum and the exchange of momentum with the other constituents.

The remaining diffusive (non-advective) mass fluxes are specified by the relations:

$\sum_i = w, a \; \boldsymbol{i}_\alpha^i = \boldsymbol{0}$, $\alpha = l, g$.

Solid phase relations

In Code_Bright the *solid phase density* is given by

$\rho_s = \widetilde{\rho}_s\,(T)$

The mechanical constitutive relation for the solid phase is not explicitly given in terms of the *solid phase stress*. Instead, the mechanical relation incorporating the solid phase is formulated in terms of *total stress*, $\boldsymbol{\sigma}$, of the porous medium and the constitutive relations of the stress tensors of the fluid phases (pressures, p_α).

A rate form of a schematic mechanical material model for unsaturated conditions can be expressed,

$\frac{d}{dt}\left(\boldsymbol{\sigma} + p_g\boldsymbol{I}\right) = \boldsymbol{D}\frac{d\boldsymbol{\varepsilon}}{dt} + \boldsymbol{h}\frac{d(p_g - p_l)}{dt}$

$\boldsymbol{D} = \widetilde{\boldsymbol{D}}\,(\boldsymbol{\sigma} + p_g\boldsymbol{I}, p_g - p_l)$, $\boldsymbol{h} = \widetilde{\boldsymbol{h}}\,(\boldsymbol{\sigma} + p_g\boldsymbol{I}, p_g - p_l)$,

where the material time derivative is given by,

$\frac{d}{dt}(\cdot) = \frac{\partial}{\partial t}(\cdot) + \frac{d\boldsymbol{u}}{dt}\cdot\nabla(\cdot).$

The small strain tensor $\boldsymbol{\varepsilon}$ is given by the displacements according to,

$\boldsymbol{\varepsilon} \equiv \frac{1}{2}\left(\frac{\partial \boldsymbol{u}}{\partial \boldsymbol{X}} + \left(\frac{\partial \boldsymbol{u}}{\partial \boldsymbol{X}}\right)^T\right)$

The unsaturated formulation is given in terms of $\boldsymbol{\sigma'} = \boldsymbol{\sigma} + p_g\boldsymbol{I}$ and $p_g - p_l$, often denoted net stress and suction, respectively.

When saturated states are considered, i.e., $p_g - p_l \le 0$, the schematic mechanical material model is given by,

$\frac{d}{dt}(\boldsymbol{\sigma} + p_l\boldsymbol{I}) = \boldsymbol{D}\frac{d\boldsymbol{\varepsilon}}{dt}$

$\boldsymbol{D} = \widetilde{\boldsymbol{D}}(\boldsymbol{\sigma} + p_l\boldsymbol{I})$,

now in terms of $\boldsymbol{\sigma''} = \boldsymbol{\sigma} + p_l\boldsymbol{I}$, often denoted effective stress tensor.

Liquid phase relations

The liquid phase is considered an ideal solution of air in liquid water. The *liquid phase density* and *liquid phase viscosity*, both considered mixture properties, are given by specified functions,

$\rho_l = \widetilde{\rho}_l\,(\rho_l,\, T)$

and

$\mu_l = \widetilde{\mu}_l\,(T)$,

respectively.

Gas phase relations

Regarding the gas it should be remembered that a constant gas pore pressure, $p_g = 0.1$ MPa, has been used in the present simulations. The gas phase is considered an ideal gas mixture, thus *Dalton's law* is adopted

$p_g = p_g^a + p_g^w$.

The *water gas pore pressure* is described by,

$p_g^w = \widetilde{p}_g^w(T)$,

and the *air gas pore pressure* p_g^a is related to the density variable θ_g^a making it possible to write

$\theta_g^a + \theta'^a_g\,(T, p_g - p_g^w(T)) = \widetilde{\theta}_g^a\,(T, p_g)$,

using Dalton's law.

7.2 Model description

Here two models simulate Hydraulic and Mechanical (HM) processes in the two KBS-3V deposition hole scale tests identified as BU1_D and BU5_E3. In the tests, water was supplied to the buffer through filter mats installed at the "deposition hole wall" in two different layouts. In layout D (used in the BU1_D test) the filter mat covered the entire surface, and in layout E3 (used in the BU5_E3 test) the filter mat only covered the surface below the canister. Besides the water supply layout, the initial dry density of the pellet slot (PS) filling also differed between the two tests and this was considered when setting up the BU1_D and BU5_E3 models as well. A "wall" friction sensitivity analysis was performed for the BU1_D model.

In order to simplify direct comparisons between models using the two different water supply layouts, two additional models (KBS_D and KBS_E3) using an equal initial PS dry density of 1 000 kg/m^3 were developed. The initial PS dry density in these models was chosen as to be better aligned with the KBS design.

Thus, the four different models are denoted **BU1_D** (or D in short), **BU5_E3** (or E3 in short), **KBS_D** and **KBS_E3**, respectively. When both KBS_D and KBS_E3 are addressed the notation KBS is used for the set.

Below follows a description of the geometry, initial/boundary conditions and finally the material models. For archive purposes a model identification is presented in Appendix 3.

7.2.1 Geometry and constituents

The geometry and constituents of the axisymmetric representation are shown in Figure 7-1 were also the discretization (mesh) is described. A mesh dependency test was performed, and the results are given in Appendix 4.

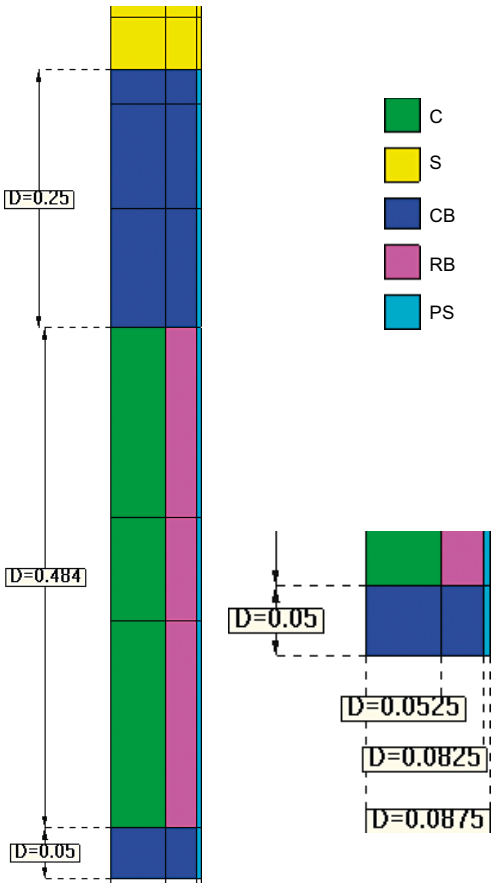

Constituent	
Name	Description
S	Spring retaining system
C	Canister
CB	Cylinder-shaped Blocks
RB	Ring-shaped Blocks
PS	Pellet-filled Slot

Discretization	
Name	No. elements: r-dir × a-dir
S	18 × 26
C	10 × 100
CB	Top: 16 × 48 Bottom: 16 × 10
RB	6 × 100
PS	2 × 158

Coordinates	
r	Radial
a	Axial
t	Tangential

Figure 7-1. *Geometry and constituents.*

7.2.2 Initial and boundary conditions

The initial conditions are given in Table 7-1. The difference in initial dry density in the PS between the two tests and the additional KBS setup is manifested through use of different values of initial porosity when representing the different tests. The porosity of the spring and canister materials was set low as not to affect the solution.

Table 7-1. Initial conditions.

Constituent	p_l [MPa]	σ_{ij}, $i = j$ [MPa]	ϕ [-]		
			D	E3	KBS
S				0.1	
C				0.1	
CB	−47.174	−0.101		0.385	
RB				0.376	
PS			0.793	0.719	0.640

No-flow hydraulic boundary conditions were prescribed at all boundaries other than along the vertical PS boundary. In the models using the D layout water supply the conditions given in Table 7-2 were prescribed all along the vertical PS boundary and in the models using the E3 layout the conditions were prescribed along the lower 0.05 m of the same boundary.

Table 7-2. Hydraulic boundary conditions at the vertical PS boundary.

Time interval [days]	Condition [MPa]	Comment
0–1	$p_l = p_{l0} - (p_{l0} + 0.1)t$	Linear ramping from the initial unsaturated state to full access of water at atmospheric conditions.
1–	$p_l = 0.1$	Full access of water at atmospheric conditions.

Two different mechanical boundary conditions were used in the models. Roller boundary conditions (no displacements in the normal direction and no change in traction in the tangential direction) were prescribed at all boundaries other than along the vertical PS boundary. No displacements were prescribed along the vertical PS boundary with an exception at the very top where roller boundary conditions were used. This was done so in order to try to decrease the simultaneous disturbance from the material interface and shift in boundary condition at the PS/Spring material interface.

7.2.3 Material representations

Constitutive relations and parameter values are given in this section. A brief description of how the parameter sets were obtained is given in the listing below, for a more detailed description see Section 7.3.

- **Hydraulic properties**
  - *Canister & Spring material*: “Inert” (should not affect the result).
  - *Buffer*: Retention according to laboratory data.
  - *Buffer*: Permeability dependence on dry density according to laboratory data.
  - *Buffer*: Intrinsic & relative permeability from moisture diffusivity comparisons.
- **Mechanical properties**
  - *Canister*: Stiff as compared to the other materials.
  - *Spring material*: According to spring stiffness in experiments.
  - *Buffer*: Using setup obtained from 1D-model calibrations.

Porous media

The retention is given by Classical van Genuchten (vG),

$$\widetilde{S}_l(p_l) = \left(1 + \left(\frac{p_g - p_l}{P_0}\right)^{\frac{1}{1-\lambda}}\right)^{-\lambda}.$$

Values for parameters P_0 [MPa] and λ [-] are given in Table 7-3.

Table 7-3. Retention parameters of porous media.

Constituent	P_0 [MPa]	λ [-]
C	5.415	0.18
S	5.415	0.18
CB	15.93	0.18
RB	19.99	0.18
PS	D: 0.0389 E3: 0.1305 KBS: 0.3891	D:0.25 E3:0.25 KBS:0.25

The advective mass flux, is given by Darcy's law

$$\boldsymbol{q}_l = -\frac{\boldsymbol{k} k_{rl}}{\mu_l}(\nabla p_l - \rho_l \boldsymbol{g})$$
$$\boldsymbol{k} = k_{in}\boldsymbol{I}$$
$$k_{rl} = {S_l}^n$$

The intrinsic permeability's and exponents for the relative permeability are given in Table 7-4.

Table 7-4. Intrinsic permeability's and exponent in the law for the relative permeability of porous media.

Constituent	k_{in} [m^2]	n [-]
C	4.9×10^{-24}	4
S	4.9×10^{-24}	4
CB	$0.6\times10^{-20}\exp(21.764(\phi - 0.5))$	5
RB	$0.6\times10^{-20}\exp(21.764(\phi - 0.5))$	5
PS	$2\times10^{-20}\exp(21.764(\phi - 0.5))$	1

Solid phase

The **solid phase density** is given by a constant,

$\rho_s = \rho_{s0}$,

and for the present models all materials are given the same value according to Table 7-5.

Table 7-5. Solid phase density.

Constituent	ρ_{s0} [kg/m^3]
C	2780
S	2780
CB	2780
RB	2780
PS	2780

Table 7-6 shows an overview of the **mechanical material models** used for the solid phase in all materials. As mentioned in Table 7-6, an existing model of the Canister Retrieval Test (CRT), see Börgesson and Hernelind (2017), was used as the basis when designing a suitable setting for the buffer materials. In the following tables, Table 7-7 and Table 7-8, the different mechanical material models are described, and the parameter values are given. More information about the buffer block and PS mechanical representation can be found in Section 7.3.2.

Table 7-6. Overview of the solid phase mechanical material models.

Constituent	Model	Comment
C	Linear elastic	Stiff as compared to the other materials.
S	Linear elastic	Calculated from the spring stiffness used in the scale tests.
CB	Modified BBM	The CRT model setting was the basis. Plastic shear properties and swelling properties were slightly changed.
RB	Modified BBM	The CRT model setting was the basis. Plastic shear properties and swelling properties were slightly changed.
PS	Modified BBM	The CRT model setting was the basis. This had to be changed significantly. The plastic shear properties were changed. Then the setup was calibrated using axisymmetric 1D models of the RB-PS system and comparing the mechanical response with "typical" swelling pressure curves. Different parameter sets had to be used for the D, E3 and KBS models due to the different initial dry densities.

Table 7-7. Linear elastic model and parameter values.

Total strain increment	$d\boldsymbol{\varepsilon} = d\boldsymbol{\varepsilon}^e$	Parameter	C	S
Elastic strain increment	$d\boldsymbol{\varepsilon}^e = -\frac{1}{3}d\varepsilon_v^e\mathbf{1} + d\boldsymbol{e}^e$ $d\varepsilon_v^e = \frac{dp\prime}{K}$, $K = \frac{E}{3(1-2\upsilon)}$ $d\boldsymbol{e}^e = \frac{d\boldsymbol{s}}{2G}$, $2G = \frac{E}{1+\upsilon}$	E [MPa]	5 000	190.5
		υ	0.2	0.0001

Table 7-8. Modified BBM model and parameter values.

Total strain increment	$d\boldsymbol{\varepsilon} = d\boldsymbol{\varepsilon}^e + d\boldsymbol{\varepsilon}^p + d\boldsymbol{\varepsilon}^h$	Parameter	CB & RB	PS (D/E3/KBS)
	$e_0 = \phi_0/(1-\phi_0)$ [(a)]	e_0	0.626 0.604	3.8/2.56/1.78
Elastic strain increment	$d\boldsymbol{\varepsilon}^e = -\frac{1}{3}d\varepsilon_v^e\mathbf{1} + d\boldsymbol{e}^e$ $d\varepsilon_v^e = \frac{dp\prime}{K}$, $K = \max\left\{\frac{(1+e)p\prime}{\tilde{\kappa}_i(s)}, K_{min}\right\}$ $\tilde{\kappa}_i(s) = \kappa_i(1+\alpha_i s)$ $d\boldsymbol{e}^e = \frac{d\boldsymbol{s}}{2G}$, $2G = \frac{3(1-\upsilon 2)}{(1+\upsilon)}K$	κ_{i0} α_i υ K_{min} [MPa]	0.13 −0.021 0.2 20	0.3/0.25/0.15 0 0.2 1e−4/0.5/2
Plastic strain increment	$d\boldsymbol{\varepsilon}^p = d\Lambda\frac{\partial g}{\partial \boldsymbol{\sigma}}$ $f = q^2 - M^2(p\prime + p_s)(p_0 - p\prime)$ $g = \alpha q^2 - M^2(p\prime + p_s)(p_0 - p\prime)$ [(b)] $M = 0.5\left(\frac{p_0+p_s}{2}\right)^{-0.23}$ or [(c)] $M = M_0$ $p_s = p_{s0} + ks$ $p_0 = p^c\left(\frac{p_0^*}{p^c}\right)^{\frac{\lambda_0-\kappa_{i0}}{\lambda(s)-\kappa_{i0}}}$ $dp_0^* = \frac{1+e}{\lambda_0-\kappa_{i0}}p_0^* d\varepsilon_v^p$	α p_0^* [MPa] p_c [MPa] λ_0 p_{s0} [MPa] k M	0.5 16.9 1 0.184 0 0.053 [(b)]	0.5 0.011/0.06/0.242 1 0.4/0.34/0.243 0.05 0 [(c)] 0.273

Hydraulic strain increment	$d\boldsymbol{\varepsilon}^h = -\frac{1}{3} d\varepsilon_v^h \mathbf{1}$ $d\varepsilon_v^h = \frac{\kappa_s}{(1+e)(s+p_{atm})} ds$ $\kappa_s = \kappa_{s0} f^m(p', e)$ [(b)] $f^m(p', e) =$ $\begin{cases} 1 & \text{if } p' < p_{ref} \\ 10^{-20} & \text{if } p' > p_{swell}(e) \\ 1 - \frac{\ln p' - \ln p_{ref}}{\ln(\tilde{p}_{swell}(e)) - \ln p_{ref}} & \text{otherwise} \end{cases}$ $\log(\tilde{p}_{swell}(e)) = -4.741 + 4.117 \cdot 10^{-3} \frac{\rho_s}{1+e} - 3.94 \cdot 10^{-7} \left(\frac{\rho_s}{1+e}\right)^2$	κ_{s0}	0.34	0.05/0.05/0.2
		p_{ref} [MPa]	0.1	0.1

[(a)] The initial void ratio is used as an input parameter to the modified BBM model. It should be set as to match the initial condition porosity.
[(b)] The functions $M(p_0, p_s)$ and $f^m(p', e)$ are features developed at Clay Technology.

Liquid phase

The liquid **phase density** is given by,

$$\tilde{\rho}_l(\rho_l, T) = 1002.6\exp(4.5\times10^{-4}(\rho_l - 0.1) + 3.4\times10^{-4}T),$$

and the **liquid phase viscosity** is given by,

$$\tilde{\mu}_l(T) = 2.1 \cdot 10^{-12}\exp\left(\frac{1808.5}{273.15+T}\right).$$

Gas phase

The models for **water gas pore pressure** and the **air gas pore pressure** are given by,

$$\tilde{p}_g^w(T) = 13607\exp\left(\frac{-5239.7}{273.15+T}\right),$$

and

$$\tilde{\theta}_g^a(T, p_g - p_g^w) = \frac{M_a}{R}\frac{1}{273.15+T}(p_g - p_g^w),$$

respectively.

7.3 Comments regarding the model setup

7.3.1 Differences between models and scale tests

In the experiments the water supplied to the test rig have had a pressure at or above atmospheric. In BU1_D 10 kPa above atmospheric was used from start up to day 76 when 100 kPa was used instead. In BU5_E3 atmospheric pressure was used up to day 125 when a pressure of 10 kPa above atmospheric was used instead. In the models, water has been assumed to be supplied under atmospheric conditions only.

When studying the accumulated water inflow to BU1_D the evolution shows an evident stagnation after an initial rapid water uptake. Then, beginning at day 76, when the pressurization of the supplied water was increased, the evolution resembles the initial with a rapid water uptake. The mechanism leading to the stagnation of water inflow during the low-pressure phase is thought to come from air trapped inside the filter which could not escape or dissolve. This type of mechanism has not been incorporated to the model and the water inflow stagnation can therefore not be expected being captured.

The small gap between rings and canister (about 1 mm) has not been handled explicitly in the models. It has been incorporated implicitly by adjusting the density of the ring-shaped buffer blocks assuming perfect radial homogenization of the inner gap and the ring-shaped blocks.

In the models, perfect adhesion was adopted between the block materials and canister. Thus, slip or gap opening have not been considered along this interface. Perfect adhesion, no slip or gap opening, has also been adopted at the outer boundary of the buffer, along the PS/steel container interface in the experimental setup. In order to represent slip/friction along this interface in the model, the PS material has been specially designed as to account for this by its shear properties.

7.3.2 Mechanical representation of buffer materials

When discussing the mechanical representation of the buffer materials, blocks (CB and RB) and PS, a brief outline of the hydro-mechanical process taking place in the system under study might be a god starting point. When taking up water the bentonite buffer materials swell and/or pressurize the confinement. In the present system the bottom and side walls of the steel tube act as fixed confinements, whereas the upper spring-loaded plug only retains the swelling buffer to a certain degree. The inner steel cylinder, simulating the canister, is an "inner confinement" with fixed dimensions, but which may change location when acted upon by the buffer.

The mechanical process may be discussed in terms of coupled radial and axial processes. In the axial direction there is heave of the plug (upper buffer surface) and displacement of the canister. The swelling of the buffer material, shear properties of the buffer and friction against the axial confinement wall may be identified as important parts of the model governing the process in this direction. As mentioned above, the friction at the confinement wall has not been addressed explicitly in the models but has been taken care of by adopting certain shear properties of the PS material.

The radial mechanical process within a horizontal cross-section during water uptake consists of swelling of the high-density buffer blocks, to a lower density, and compression of the low-density PS constituent, to a higher density. It should be noted that, in general, the density field over the cross-section is not expected to be fully homogenized when full water saturation has been achieved. In the model the swelling properties of the buffer components plays a main role and the high- and low-density components properties have to "match" well as to obtain reasonable final dry density profiles.

The material model setting used in an existing model of the Canister Retrieval Test (CRT) was the basis for the present models. In the end, the setting of the buffer block materials did not have to be changed very much from the CRT setting and was unchanged between the models within this study. The PS material properties on the other hand had to be adjusted significantly from the CRT setting and had to be adjusted for each case (D, E3 and KBS) due to the large difference in initial dry density.

In order to evaluate calculated dry density fields and density dependent properties, initial and radially fully homogenized dry densities are useful reference values. In Table 7-9 and Table 7-10 dry densities are given for cross-sections with ring-shaped and cylinder-shaped blocks, respectively.

Table 7-9. Dry densities (kg/m^3) for cross-sections with ring-shaped blocks.

Constituent	Case		
	BU1_D	BU5_E3	KBS
RB	1735*	1735*	1735*
PS	575	781	1000
HOM	1534	1569	1607

* Adjusted for a 1 mm slot between the canister and inner surface of the ring-shaped block.

Table 7-10. Dry densities (kg/m^3) for cross-sections with cylinder-shaped blocks.

Constituent	Case		
	BU1_D	BU5_E3	KBS
CB	1710	1710	1710
PS	575	781	1000
HOM	1584	1607	1631

Shearing properties of the buffer components

In the discussion above the possible importance of the shearing properties of both the buffer blocks and PS material was mentioned. In order to get convinced that the models were representative and up for the current task, formulations and experimental data were reviewed.

The shearing properties ("internal friction") of the block materials was modified by making one of the parameters, the "cohesion pressure" p_s, dependent on suction,

$p_s(s) = ks$

The parameter k was set as to obtain the formerly used value p_{s0} at the initial suction s_0, i.e.,

$$p_s(s) = \frac{p_{s0}}{s_0} s.$$

Thus, at zero suction, see Figure 7-2, the material was made cohesionless, which is in line with experimental findings, and at the initial suction, see Figure 7-3, the material had the same cohesion as used previously.

The internal friction angle is again, as for the CRT model, variable according to a p-q relation obtained from experimental findings, see Figure 7-2 and Figure 7-3. It should be noted that the p-q relation is obtained from considering data for saturated conditions, but it has here been assumed that this relation is also relevant when going into the unsaturated regime.

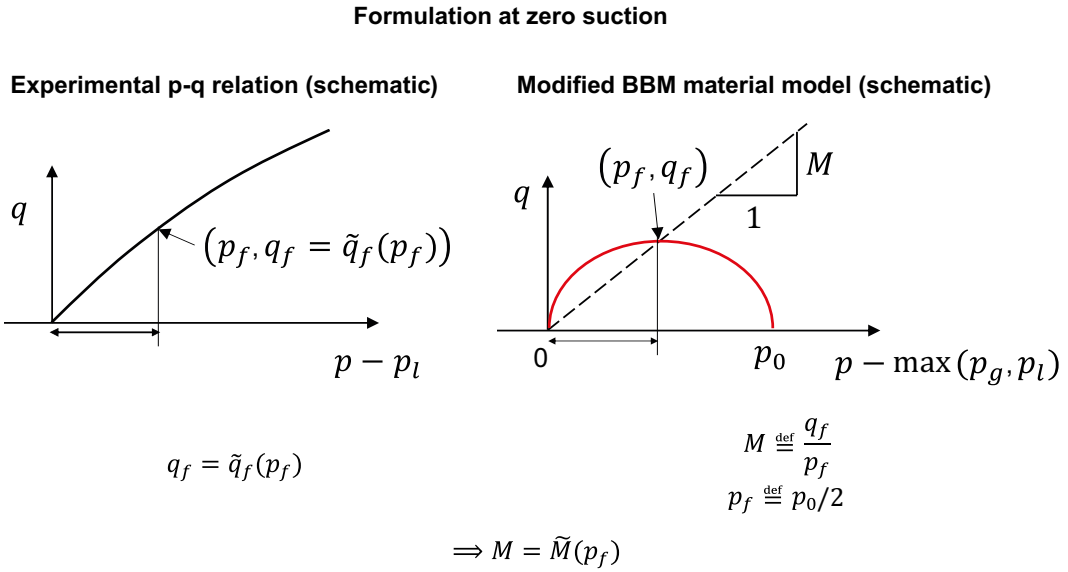

Figure 7-2. *Formulation at zero-suction conditions. Connection between an experimentally motivated p-q relation and the pressure dependent shearing properties of the modified BBM material model.*

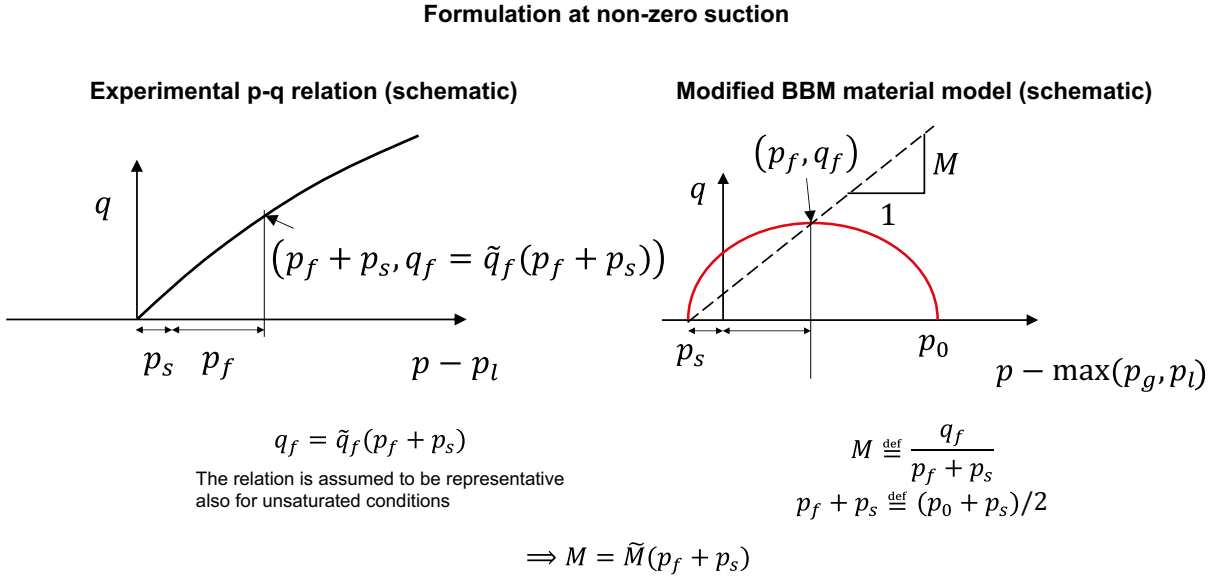

Figure 7-3. *Non-zero suction conditions. Connection between an experimentally motivated p-q relation (assumed to be valid also at unsaturated conditions) and the pressure dependent shearing properties of the modified BBM material model.*

The resulting representation was then compared with experimental data in terms of friction angles using the relation

$$\sin\theta = \frac{3M}{6+M},$$

to translate between the BBM parameter M and friction angle θ. Figure 7-4, containing an altered version of a diagram from TR-16-04, shows experimental data and model data in one diagram. The relevant experimental data for this comparison, where internal friction is addressed, is the one obtained using grooves. It should be noted that in Figure 7-4 the model behaviour is for simplicity shown using three different constant values of p_s, thus for constant values of suction.

In order to incorporate the representation of the friction between the confinement wall and the PS material, thus "external friction", and simplify/making the model more robust, the formulation was changed as to obtain a constant friction angle, using a constant M. When studying experimental data 7.5° (M = 0.273) was adopted for the base case setting and 5° (M = 0.180) and 10° (M = 0.369) were chosen for investigating the sensitivity. The experimental data and adopted values of friction angle are shown in Figure 7-5, where the experimental data relevant for external friction is indicated by "steel", i.e., a smooth steel surface was in contact with the clay. The basis for Figure 7-5 is again a diagram from TR-16-04.

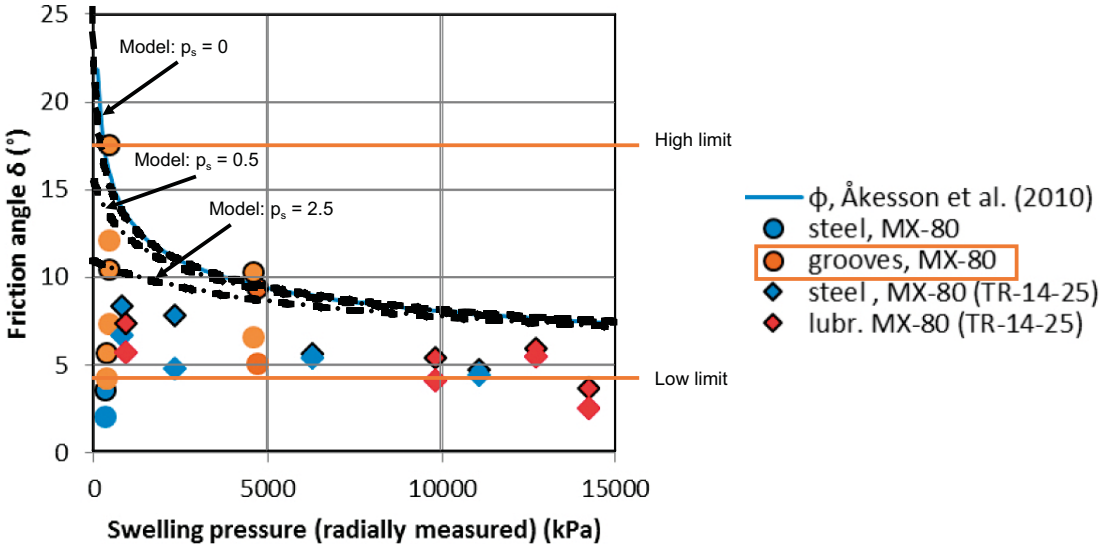

Figure 7-4. *Comparison between experimental data and representation of the block material model for three different constant values of p_s (suction). Here, where internal friction is addressed, the experimental data indicated by "grooves" is most relevant. All results from tests on friction between MX-80 and steel, lubricated steel and grooves are shown. Results from the report TR-14-25 are shown with diamonds. From each test both the peak value (with marker line) and the residual value (without marker line) are shown.*

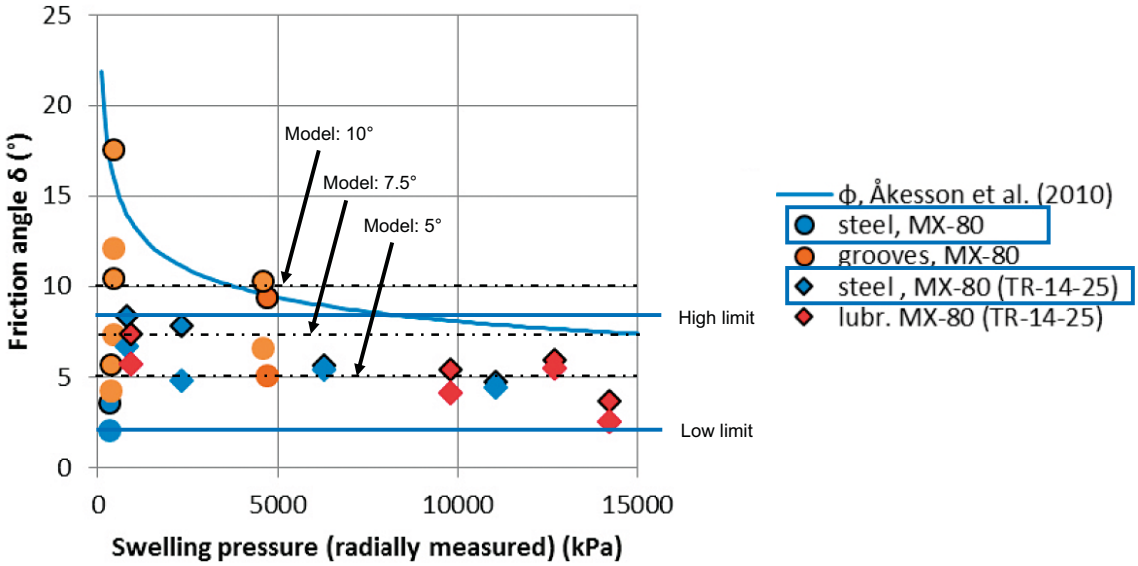

Figure 7-5. *Comparison between experimental data and representation of the pellet filled slot material model. 7.5° was used in the "Base Case" and the other two (5° and 10°) in the sensitivity analysis. Here, where external friction is addressed, the experimental data indicated by "steel" is most relevant. All results from tests on friction between MX-80 and steel, lubricated steel and grooves are shown. Results from the report TR-14-25 are shown with diamonds. From each test both the peak value (with marker line) and the residual value (without marker line) are shown.*

Evaluating/matching the buffer components parameter sets

The combined performance of the ring-shaped block and PS-material parameter sets was evaluated by comparing the mechanical evolution for the system, shown in Figure 7-6, against typical (experimentally motivated) swelling pressure curves, see Figure 7-7. The lower black curve in Figure 7-7 is representative for water uptake/swelling conditions and the upper black curve is representative for drying/consolidation, see Åkesson et al. (2010).

As mentioned above, when modelling BU1_D, BU5_E3 and the fictive KBS-case, different PS-setups were necessary in order to obtain relevant results. This comes from the different initial state (dry density/porosity/void ratio) of the PS constituent together with the, according to our experience, "lack of generality" of the material model. By that it is meant that it has not been successful to equip the material model with one set of parameters and then being capable to obtain proper responses when starting from as different initial states as in the three present cases. In Figure 7-7 the initial void ratio of the PS constituent for BU1_D, BU5_E3, and CRT (which equals that of KBS) are indicated at the vertical axis.

Another shortage of the material model when trying to represent large changes in dry density for our type of material can be seen in Figure 7-7 as well. The present formulation of the mechanical material model is linear in e-ln(p'). The curved appearance of the swelling pressure curves, however, shows that these are not linear in e-ln(p'). They actually agree rather well with linear curves in ln(e)–ln(p'). Due to this mismatch in the formulations, if large changes in the mechanical state take place during the homogenization process, as in the case when modelling BU1_D shown in Figure 7-7, the state for points within the PS constituent will not always be within the range as defined by the experimentally motivated swelling pressure curves.

In addition to study the mechanical evolution, the parameter set performance was assessed by studying the appearance of the radial profile of dry density (porosity) at full water saturation. The block and PS materials are expected to interact as to generate a relatively smooth dry density profile over the material interface, without significant steps or humps. When trying to achieve this, it was found beneficial to set the referential pressure, p_{ref}, present in the expression of the "hydraulic strain increment" (a strain increment generated by an increment in suction, see Table 7-8), to a lower value of 0.1 MPa (from 1 MPa) for the block representations.

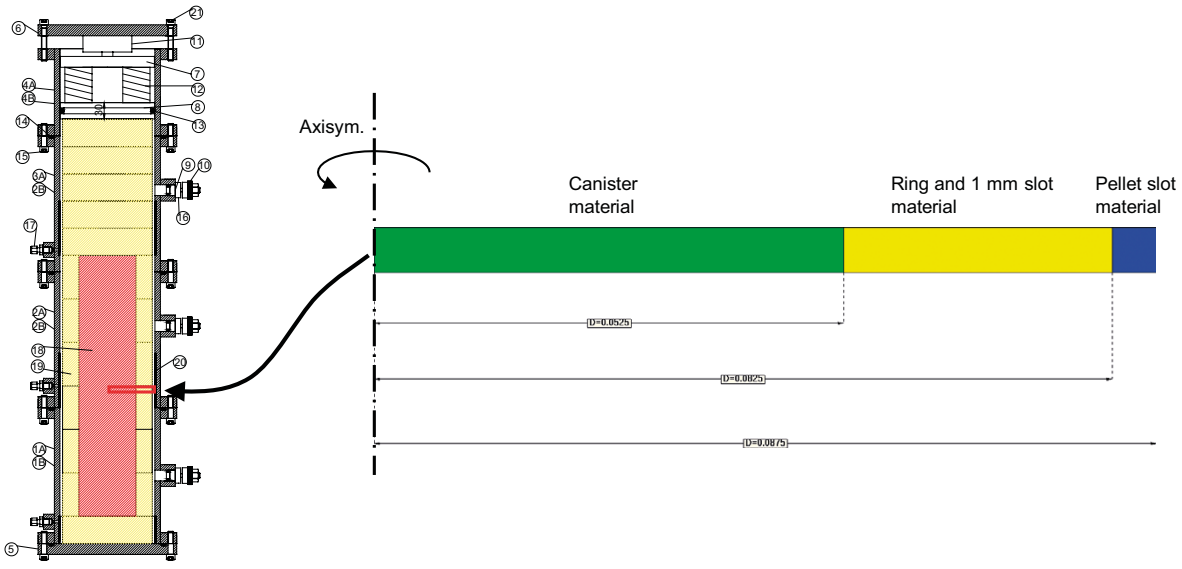

Figure 7-6. *Geometry of the 1D model of an axisymmetric disc at canister mid height used when evaluating the PS material parameter setup.*

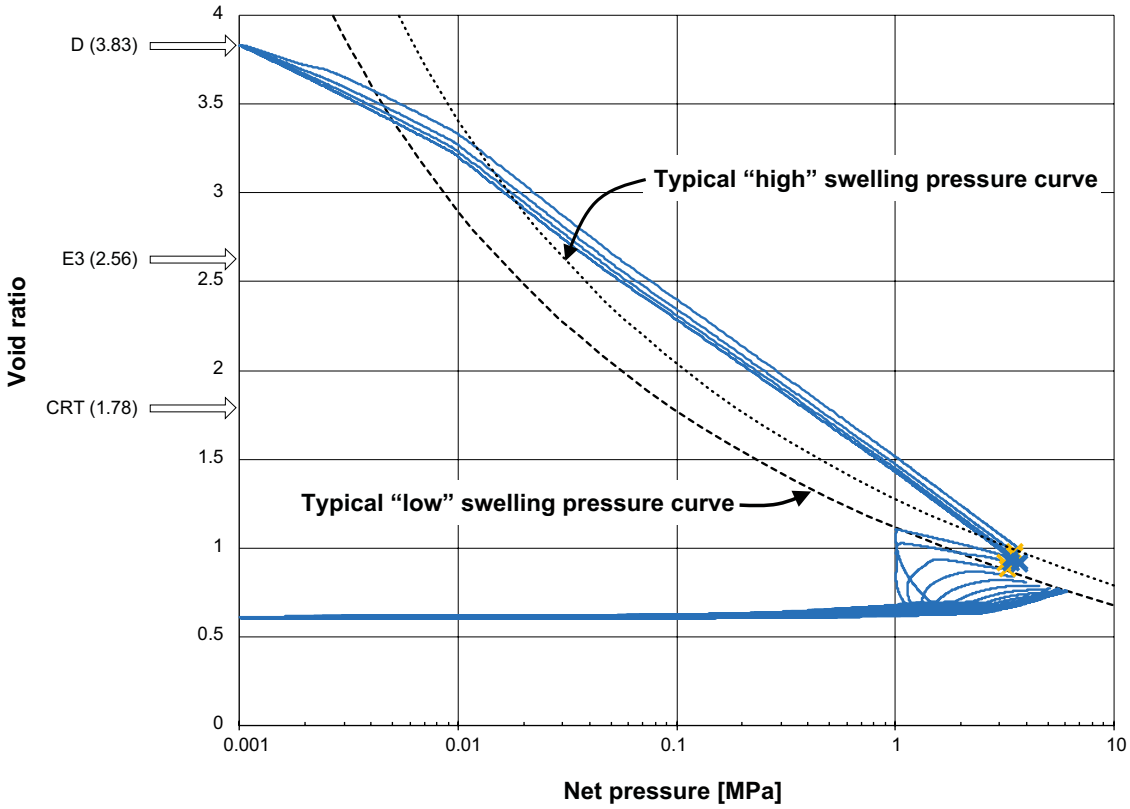

Figure 7-7. *Mechanical evolution in terms of e-ln(p') during water uptake in a 1D disc model of the BU1_D experiment. Blue curves indicate the evolution in different points, the lower cluster belong to points within the block and the upper to points within the PS material. Typical (experimentally motivated) swelling pressure curves are indicated by the black lines. Initial states for BU1_D, BU5_E3, and KBS = CRT are indicated on the vertical axis.*

7.3.3 Hydraulic representation of buffer materials

Retention

The van Genuchten retention curves, given by,

$$\widetilde{S_l}(p_l) = \left(1 + \left(\frac{p_g - p_l}{P_0}\right)^{\frac{1}{1-\lambda}}\right)^{-\lambda},$$

were calibrated using the initial state water ratio together with, for each material, individually designed "target curves" of suction as a function of degree of water saturation. The target curves were designed using experimental data for unconfined conditions and an assumption of linear swelling pressure build-up under confined conditions. One of the parameters (λ) in the van Genuchten retention was used as a fitting parameter as to get a curve matching the target curve shape. The second parameter (P_0) was then given by the initial state and the selected lambda value.

The used target curves (denoted by “Help curve” in the figures) and calibrated retention curves are shown in Figure 7-8 and Figure 7-9. As can be seen the initial state (suction) for the PS materials equals that of the blocks (47.274 MPa). In the experiment however, the initial suction was about 100 MPa, but in order to simplify the model it was assumed that the PS material was equilibrated with the blocks from start.

For the block materials the target curves were obtained by using experimental RH-water ratio data for free conditions and then calculate a target curve adopting the relation: target = suction at free conditions − swelling pressure. The swelling pressure was assumed to be linearly increasing from zero at the initial unsaturated state to the fully saturated state where it’s magnitude equals the suction at the water ratio corresponding to fully saturated conditions. For the PS materials the target curves were fictive and considered being just below the experimental data points.

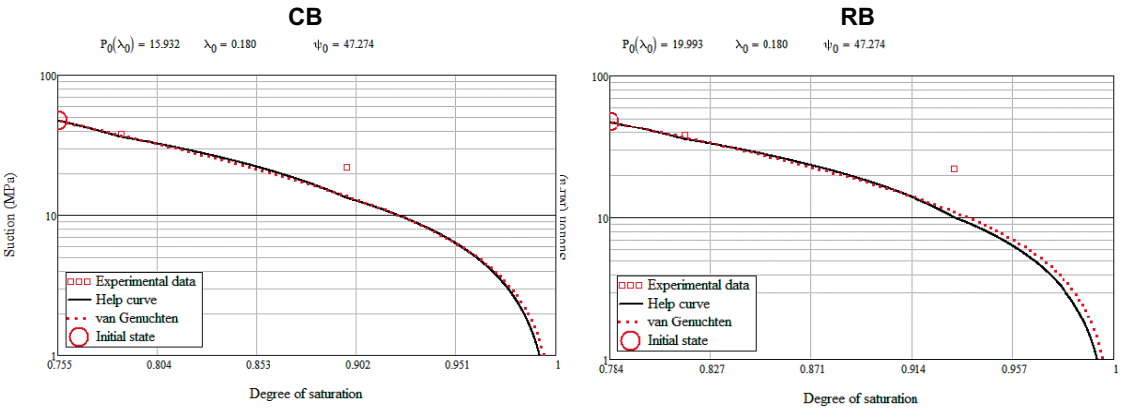

Figure 7-8. *Block (CB and RB) retention curves. The van Genuchten functions (red dotted line) were calibrated as to match the initial state (red circle) and follow the target/help curves (black solid line).*

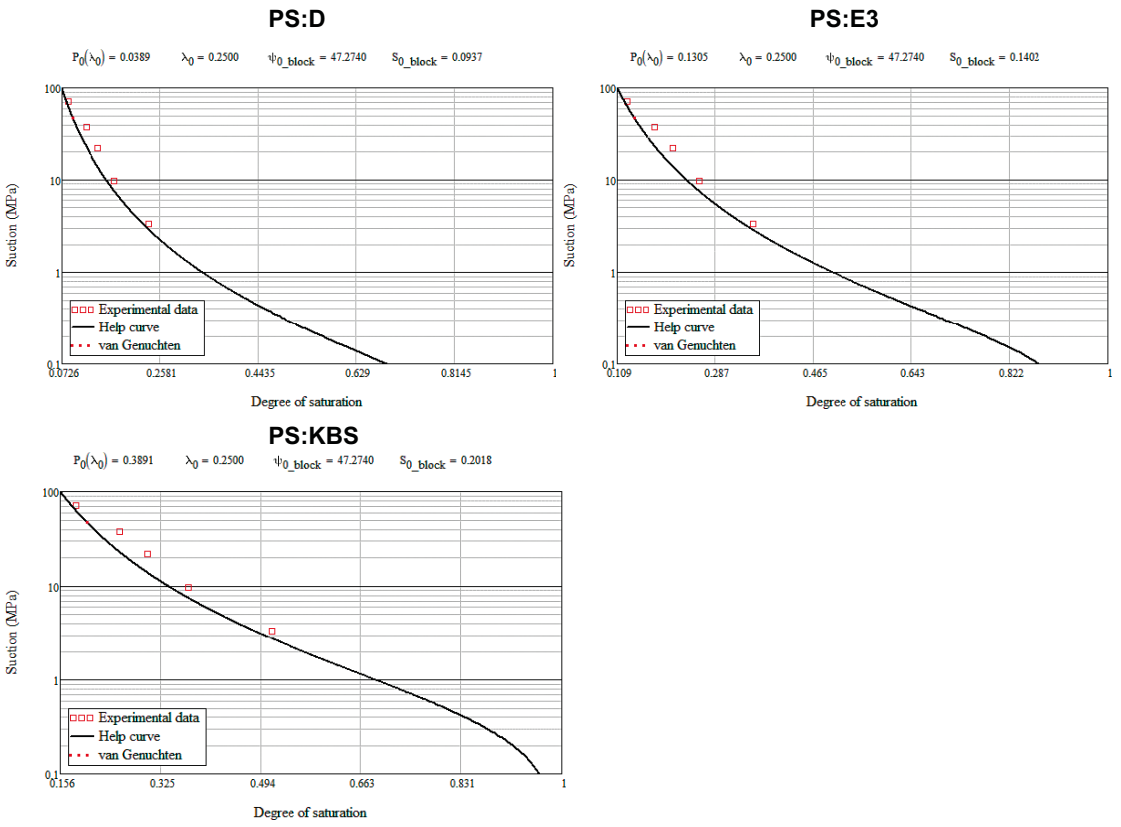

Figure 7-9. *PS retention curves. The van Genuchten functions (red dotted line) were calibrated as to match the initial state (red circle) and follow the target/help curves (black solid line).*

It should be noted that the described procedure and thus the obtained van Genuchten retention curves, assumes confined conditions. Code_Bright actually contains a possibility to use a porosity dependent van Genuchten model (enabling unconfined conditions) which could be considered in future studies to obtain greater generality. The porosity dependent model has proven to be successful in the past, but it was not used here in order to keep the complexity down.

Initial setting of the porosity dependent permeability

Experiments show that the permeability (or hydraulic conductivity) of Bentonite clay is dependent on dry density, see Figure 7-10. For reference the initial dry densities for the pellet filled slot, cylinder-shaped and ring-shaped blocks are indicated in Figure 7-10 as well as the fully homogenized (averaged) initial dry density. The experimental data indicated by the symbols can be fitted using different expressions, and in Åkesson et al. (2010) the expression,

$$k(e) = k_{ref}\left(\frac{e}{e_{ref}}\right)^{\eta},$$

given as a function of void ratio, was suggested. The parameter set $\{k_{ref} = 2.4 \times 10^{-20}$ m/s, $e_{ref} = 1$, $\eta = 5.33\}$ was found suitable, and the resulting curve is indicated by 'Reference curve' (the hatched red line) in Figure 7-10.

The function given above was used as a "target function" when evaluating a suitable value of the parameter b in the function,

$$\tilde{k}_{in}(e) = k_{ref}\exp\left(b\left(\frac{e}{1+e} - \frac{e_{ref}}{1+e_{ref}}\right)\right),$$

available in Code_Bright. It was found that $b = 21.764$ gave a good agreement between the target function and Code_Bright expression.

As can be seen, there is quite a bit of scatter in the data and therefore Åkesson et al. (2010) recommended to use more than one realisation, with different values of k_{ref}, and consider the differences between the responses as uncertainties.

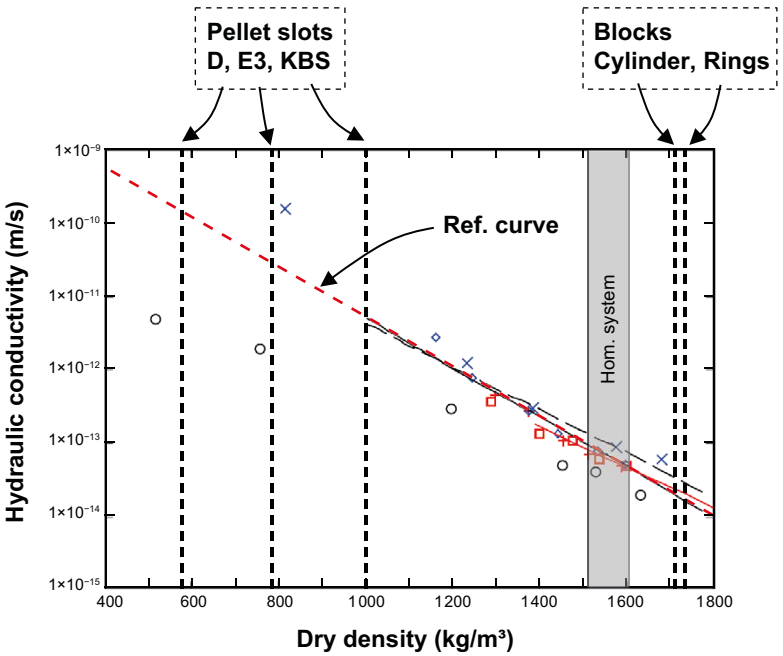

Figure 7-10. *Hydraulic conductivity data and fitted expressions.*

Diffusivity analysis, updated porosity dependent permeability

The applicability of the parameter setting of the hydraulic description can be evaluated by calculating a moisture diffusivity, using the parameter values, and compare this with the result obtained from fitment against water uptake tests, see Sellin et al. (2017). Results obtained from fitment against water uptake tests for compacted bentonite samples are shown in Figure 7-11 and as can be seen, the MX-80 data for the lower void ratio ($e = 0.7$) ends up at about 4×10^{-10} m^2/s.

The moisture diffusivity can be calculated from the expression,

$$\tilde{D}(\phi, S_l) = \frac{\tilde{k}_0(\phi)\tilde{k}_{rl}(S_l)}{\phi\mu}\frac{d\tilde{S}_l}{dp}^{-1}(S_l)$$

where dependencies on both porosity and liquid degree of saturation are present. To the left in Figure 7-12, graphs generated by using the relation above are shown. The graphs were obtained by using two porosities, the initial (solid lines) and the one obtained for a fully radially homogenized section (dotted lines) and letting the degree of liquid saturation vary. The selected parameter values are $k_{ref} = 0.6 \times 10^{-20}$ m^2 and $n = 5$.

To the right in Figure 7-12 the diagram in Figure 7-10 is given together with the values obtained for the adopted value of k_{ref}. The resulting hydraulic conductivities (red crosses) ends up below the reference curve. This could reflect that the adopted retention curves overestimate the suction at a given degree of saturation of the materials. The effect of this could be the topic of a following study.

Using the relatively high value of $n = 5$, is motivated from trying to diminish the decreasing trend of the moisture diffusivity with degree of liquid saturation, since the opposite trend have been found in experiments.

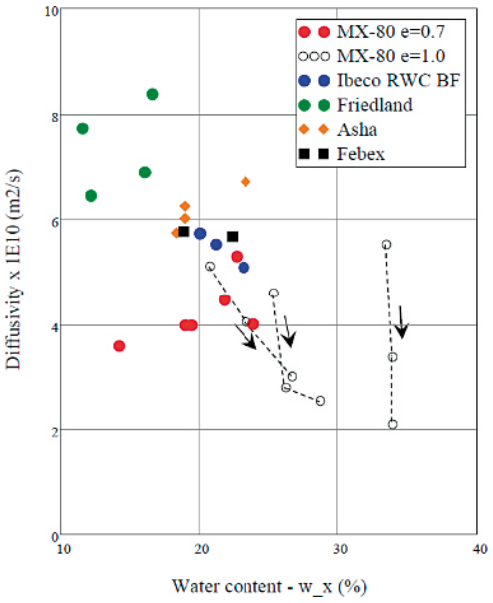

Figure 7-11. *Part of "Figure 7-1. Water-uptake tests (left); evaluated diffusivity values (right)." (Sellin et al. 2017).*

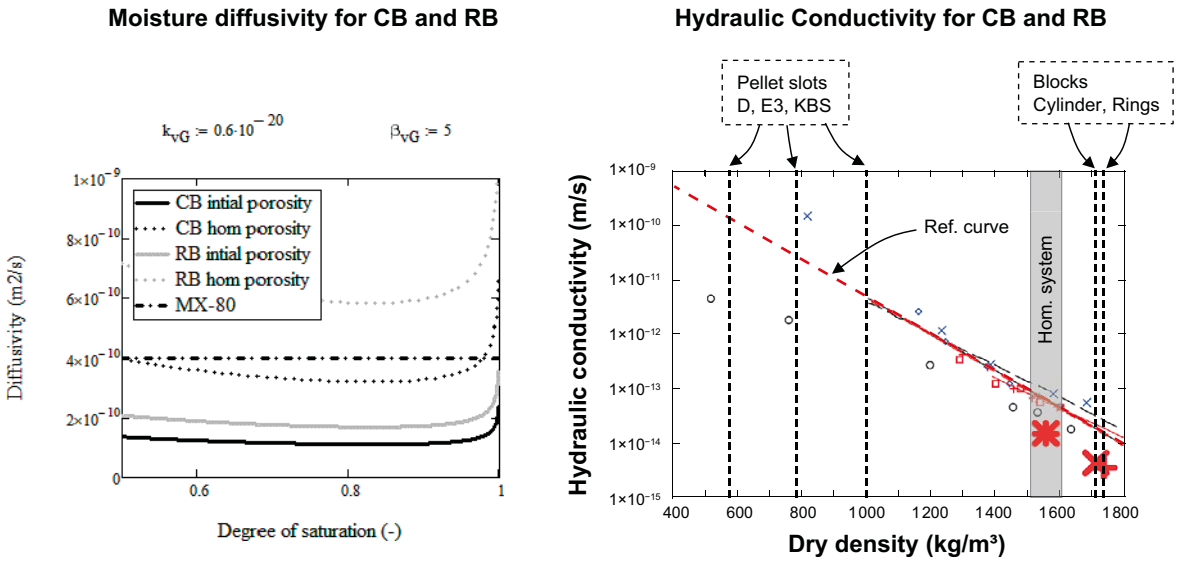

Figure 7-12. *Moisture diffusivity and hydraulic conductivity for block (CB and RB) materials. The red crosses indicate the resulting conductivities at the initial state and a homogenized system.*

When evaluating a moisture diffusivity for a water uptake test containing a pellet filled volume a value of 3×10^{-10} m^2/s was obtained. Using the same procedure as for the compacted buffer components above results in the graphs shown in Figure 7-13. The selected parameter values are $k_{ref} = 2 \times 10^{-20}$ m^2 and $n = 1$. The evaluation gave that there was no need to use different parameter values for the D, E3 and KBS cases.

Since the change of k_{ref} from the reference curve setting was small the hydraulic conductivity ends up very close to the reference curve. The selected low value for the exponent, n, could be considered a "trick" as to obtain a more representative initial water uptake for the present material structure. The resulting low flow resistance at low degrees of saturation is expected to be relevant for a material with large macro voids, which is the case for a pellet filled slot at dry conditions.

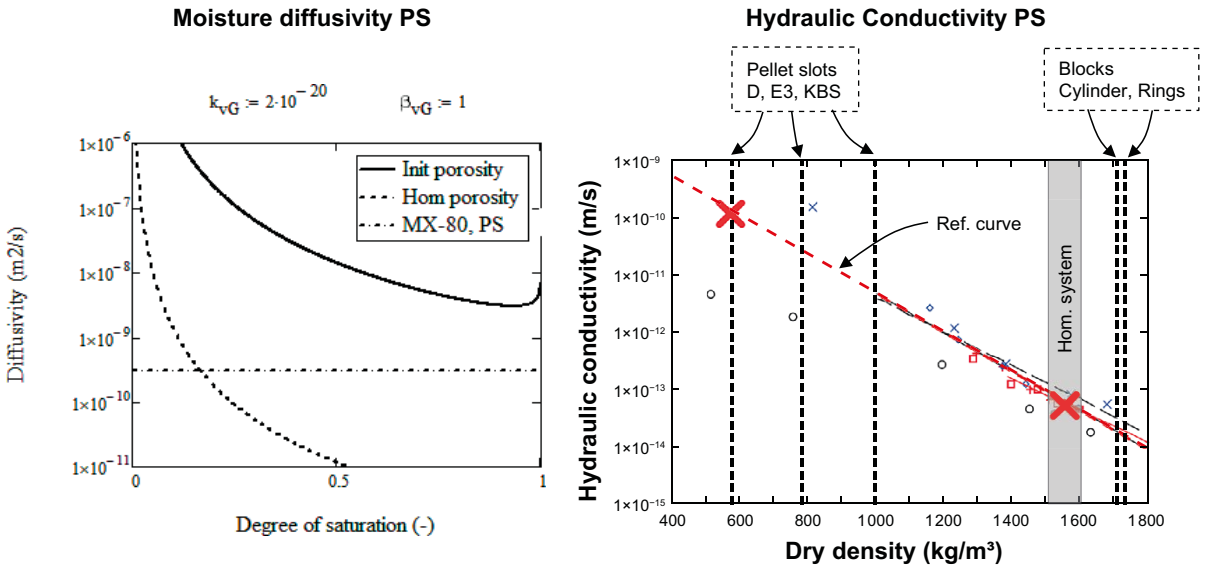

Figure 7-13. *Moisture diffusivity and hydraulic conductivity for PS material. The red crosses indicate the resulting conductivities at the initial state and a homogenized system.*

7.3.4 Retaining system representation

In the experiment the retaining system, consisting of 8 parallel coupled springs with a spring stiffness of 572.9 N/mm, simulated the mechanical reaction from the tunnel backfill when acted upon by the swelling deposition hole buffer.

To represent this in the model a retaining system material, with the same diameter as the DH and a height of 1 m, was given a Young's modulus of 190.5 MPa and a Poisson's ratio of 0.001. The response of the modelled retaining system agreed well with what was measured in the experiment, see Figure 7-14.

7.4 Results and discussion

The results from the simulations are presented in three subchapters containing the output from models BU1_D, BU5_E3 and KBS_(D/E3), respectively.

7.4.1 Simulation of BU1_D

Here results following from solving the problem formulation as described by the BU1_D model are shown and discussed. Just as a reminder, the D filter layout meant that water was introduced along the entire vertical boundary. First comes a comparison with operational data, then follows a prediction of the state after 359 days of operation (the estimated time when dismantling) which is compared to excavation data, and finally a sensitivity analysis regarding the friction angle of the pellet filled slot is given.

Comparisons with operational data

Accumulated water uptake

The accumulated water uptake was obtained by performing a post-process numerical integration of the boundary node fluxes given for different times in a solver output-file. Given the relatively crude way to obtain this result, the (numerical) accuracy of the curve given in Figure 7-15 should not be considered as high as compared to the results.

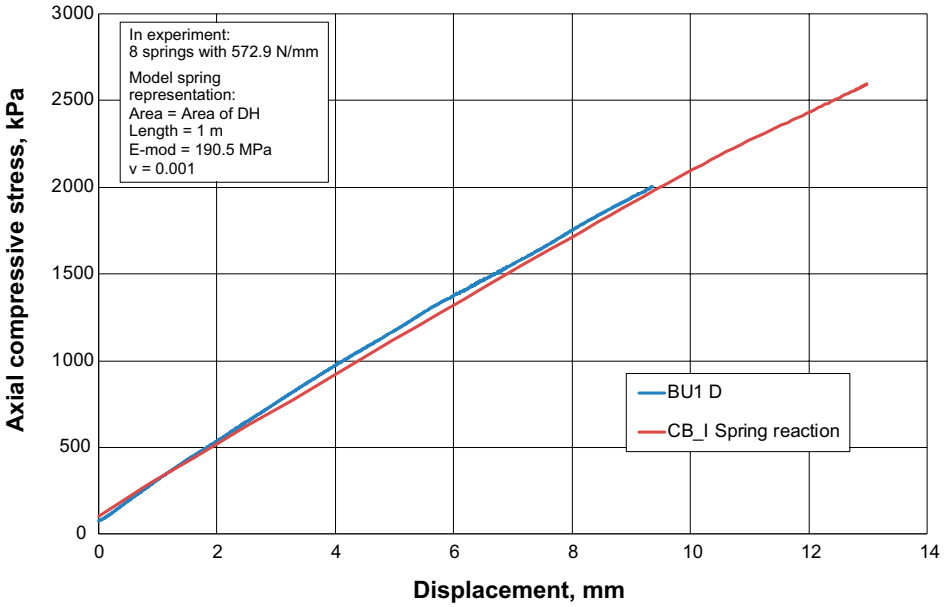

Figure 7-14. *Mechanical response in the experimental and modelled retaining system.*

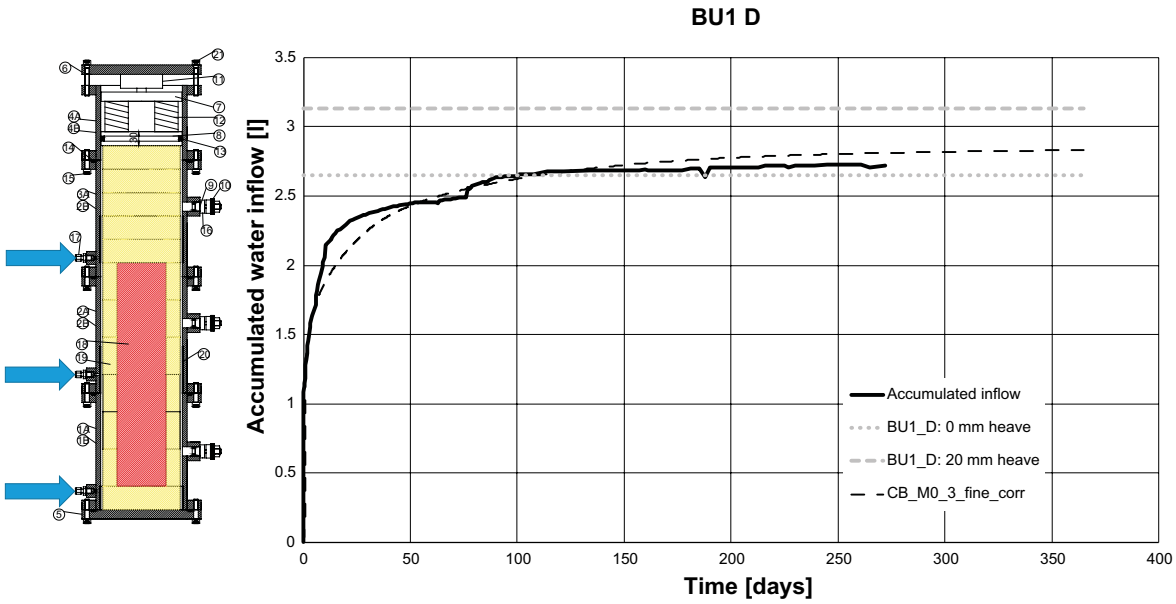

Figure 7-15. *Accumulated water inflow. Solid line: experimental data, hatched black line: model output, dotted/hatched grey lines: available volume for water at 0 mm/20 mm heave, respectively.*

Even though the limited accuracy of this result should be kept in mind, the nice agreement between the experimental curve and calculated curve indicates that the model setup is capable of producing relevant responses of the water uptake process. The effect from increasing the filter water pressure about day 76 in the experiment can be seen as a step in the experimental curve. As mentioned above, in the model the water was fed at atmospheric pressure during the entire simulation which gives a smooth accumulated water inflow curve without sudden steps.

Plug displacement and plug pressure

When looking at the experimental data of plug displacement and plug pressure the effect from changing the inlet water pressure at day 76 is obvious. Again, this effect will not be seen in the simulation due to use of a constant water pressure. If disregarding this effect, the agreement between the experimental data and solution is good. Since both the "global" displacement and "global" force responses are well captured (as well as the "global" water inflow), the soundness of the overall model setup is considered to be validated.

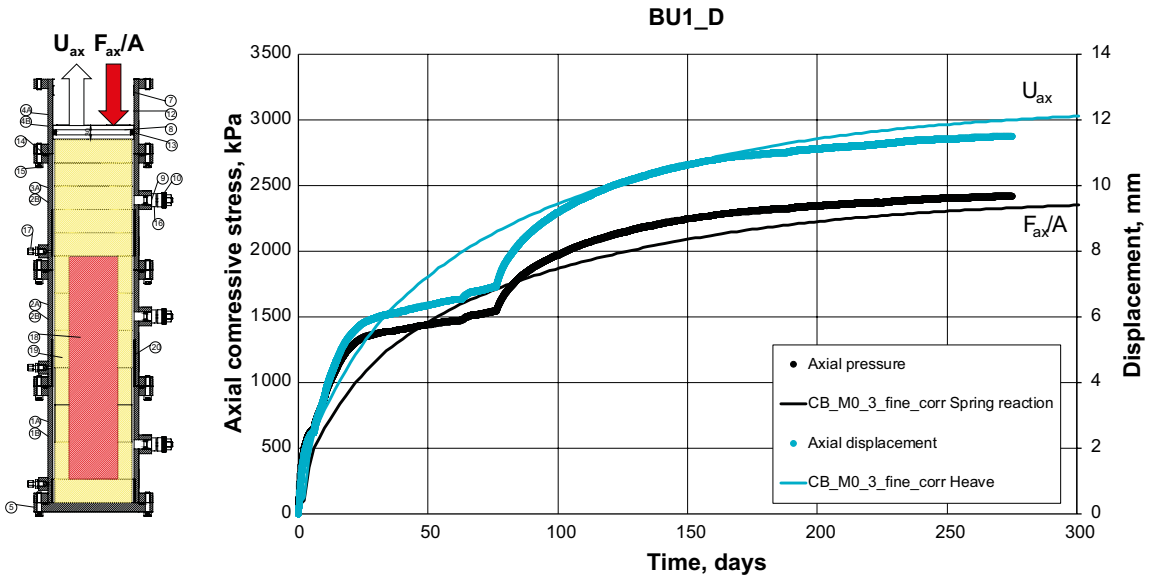

Figure 7-16. *Axial plug displacement and pressure. Thick lines: experimental data, thin lines: model output.*

Radial total stresses

The radial stresses in the experiment and model have good agreement. The magnitudes of radial stresses at the last experimental data points are higher for the simulation, but if considering the overall evolution/relations in the comparison, the model in large show the same behaviour as was recorded in the experiment:

- the rate of the stress build-up,
- the responses for the lower two points being almost the same,
- the upper point response having a slower build-up,
- the upper point response eventually catching up and overshooting the others.

The agreement in the "local" responses is an indication of that the material models have been set up as to represent the materials in the experiment properly.

Predicted state at dismantling

At the time when performing the simulation, the test was still in operation. The duration of the test was estimated to be 359 days, from 2018-08-21 to 2019-08-15. It turned out to be 349 days in the end, but the difference of 10 days should not affect the solution to a large degree.

It should be mentioned that the solutions about the top right corner are affected by an artefact of the models. In order to avoid unnecessary complexity, spring, block and PS materials were assumed to be perfectly bonded at their interface. This in turn introduced an unrepresentative high stiffness of the system about the interface. The solution about this point should therefore not be relied upon to the same degree as for the rest of the model.

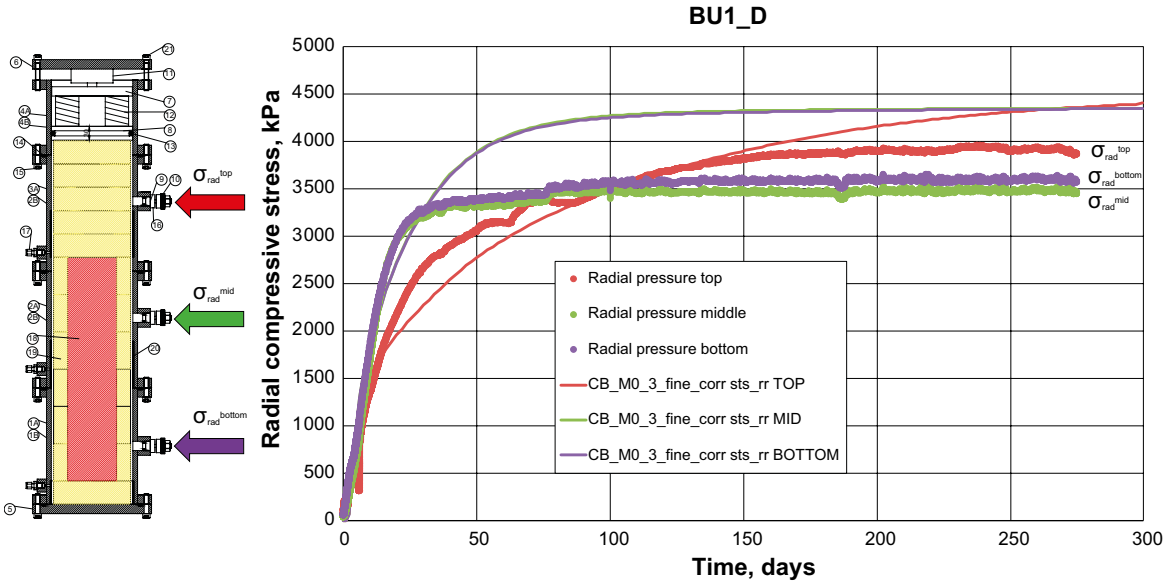

Figure 7-17. *Radial total stresses. Thick lines: experimental data, Thin lines: model output.*

The predicted state at day 359 is compared to what was obtained at the actual excavation at day 349 in terms of contour plots of degree of saturation Figure 7-18, contour plots of dry density Figure 7-19, and profiles of dry density at different heights Figure 7-20.

The maps of degree of water saturation shown in Figure 7-18 agree well. The simulation might seem to be saturated to a larger degree, but the uncertainty when determining the degree of saturation of the samples is relatively large. The major part of the excavation data indicates a fully saturated state. The simulation indicates that the central part of the cylinder-shaped blocks is the last to be saturated and this can in fact also be noticed in the excavation data below the canister and at the top of the buffer.

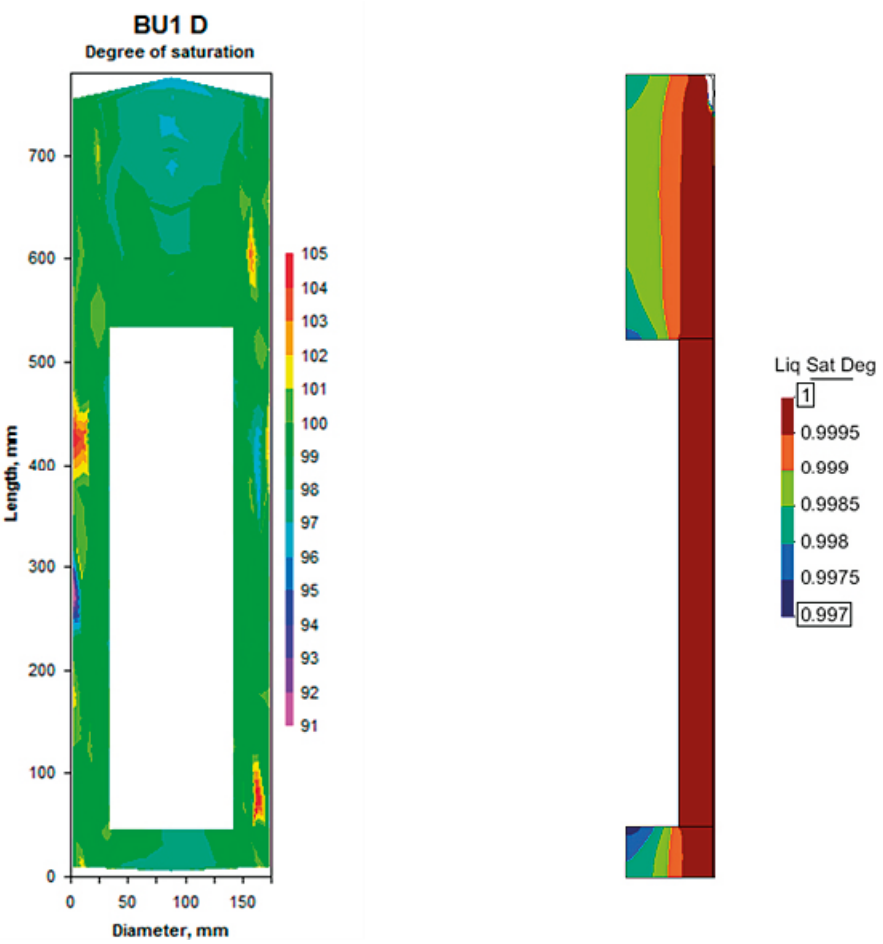

Figure 7-18. *Maps of degree of saturation obtained from analysing excavated samples (left) and the simulation (right).*

When studying the maps of dry density, shown in Figure 7-19, the overall appearance of the maps will be focused on rather than comparing values since this information is better studied using the profiles of dry density at different heights shown in Figure 7-20. The agreement between the maps regarding overall appearance seems rather satisfying. The highest dry density appears below the canister. There are high dry density volumes on top of and at the side of the canister. Lower dry density is found along the periphery of the buffer.

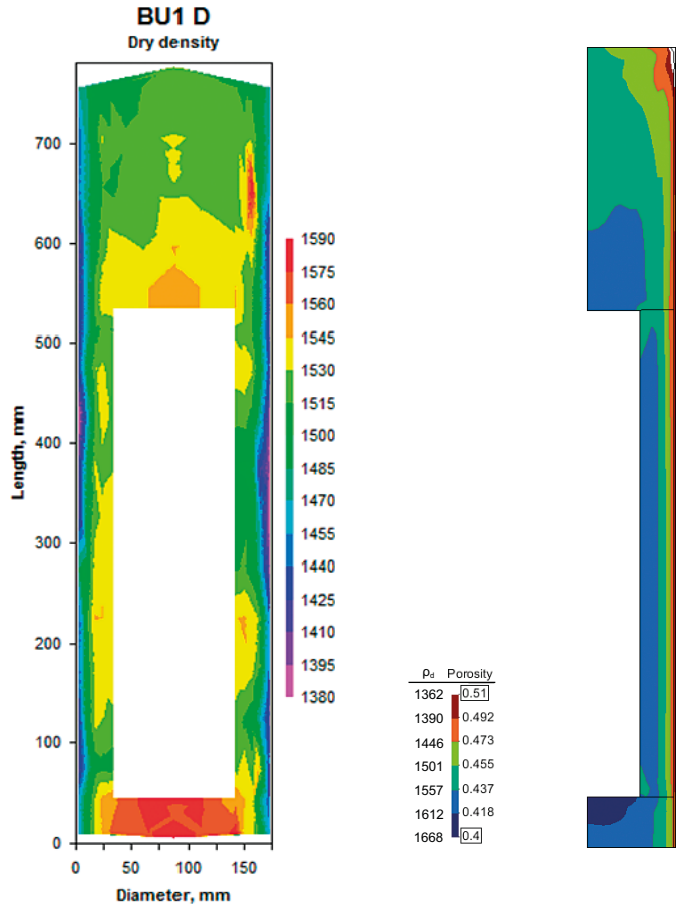

Figure 7-19. *Maps of dry density obtained from analysing excavated samples (left) and the simulation (right).*

As mentioned above, when comparing values of dry density between the excavation data and simulation, profiles of dry density at different heights, shown in Figure 7-20, are used. The larger diagram contains results from the simulation and the inserted smaller diagram contains the excavation data. The model response at outer positions for section L17 is not expected to be representative due to the artefact mentioned earlier. The density profiles can be compared to 1 560 kg/m^3, the calculated average dry density obtained at installation. In the model the radially homogenized dry density was 1 534 kg/m^3 and 1 584 kg/m^3, for ring-shaped and cylinder-shaped block sections, respectively.

The overall agreement between the results is good. The positions of the profiles relative to each other within the two sets are alike except at the outer positions of L17. The profiles from the experiment are centred just above 1 550 kg/m^3 in the central part of the buffer (25–150 mm) whereas the simulation profiles end up slightly higher, just below 1 600 kg/m^3. For the outer positions (< 25 mm and > 150 mm) the experimental data decrease down to 1 400 kg/m^3 and the same pass for the simulation if the L17 result is disregarded.

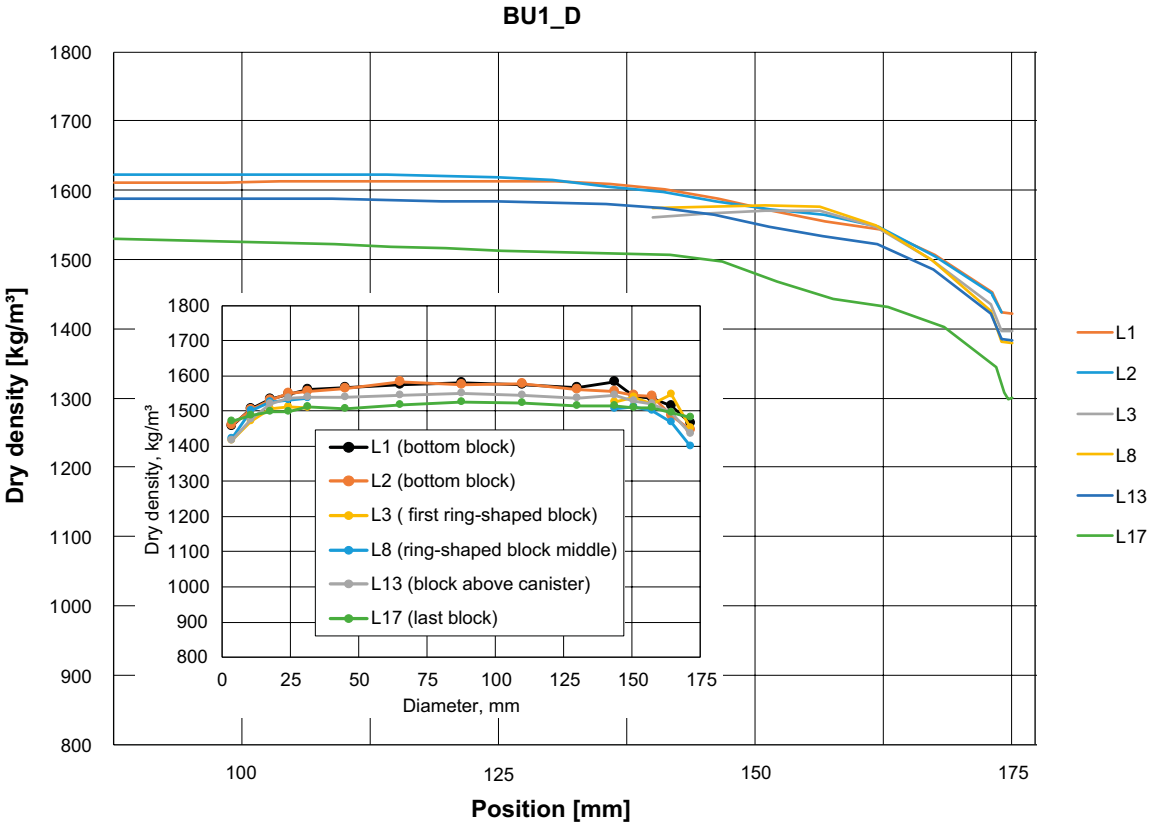

Figure 7-20. *Predicted dry density profiles of the buffer after 359 days of operation (large diagram) and excavation data after 349 days (small diagram).*

Studying influence from using different friction angles in PS

As mentioned above, friction against the axial confinement wall may be one important part of the model governing the mechanical process. Therefore, two additional models, (indirectly) equipped with different magnitudes of wall friction, have been developed and their solutions have been compared with respect to the base case solution. In the additional models the PS material has been set up as to have friction angles of 5° or 10° as compared to 7.5° used in the base case model. Figure 7-21, Figure 7-22 and Figure 7-23 show accumulated water inflow, plug mechanics, and radial stresses for the experiment and all three models, respectively.

The accumulated water inflow does not show a significant change when changing the friction angle. The plug mechanics agrees with what is expected, the lower friction angle (which means less retaining friction force) the higher axial pressure and heave. When comparing with the experimental data the adopted base case setting of 7.5° seems adequate.

The radial stresses comply with the former results, the lower the friction angle the lower the radial stress. This can be thought of as following from the logic: lower friction => more heave => lower density => lower pressure/stress. The difference resulting from using different friction angles is small in terms of radial stresses, especially so at the lower positions where swelling is limited.

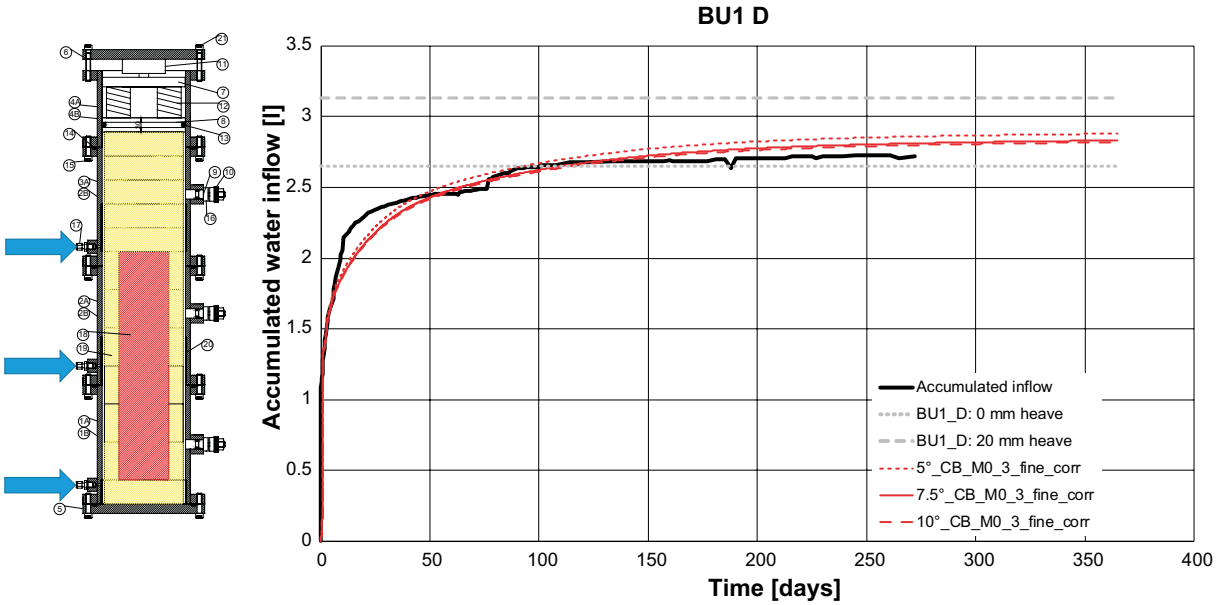

Figure 7-21. *Accumulated water inflow using different PS friction angles. Black solid line: experimental data, red lines: model data, black hatched line: available volume for water at 11 mm heave.*

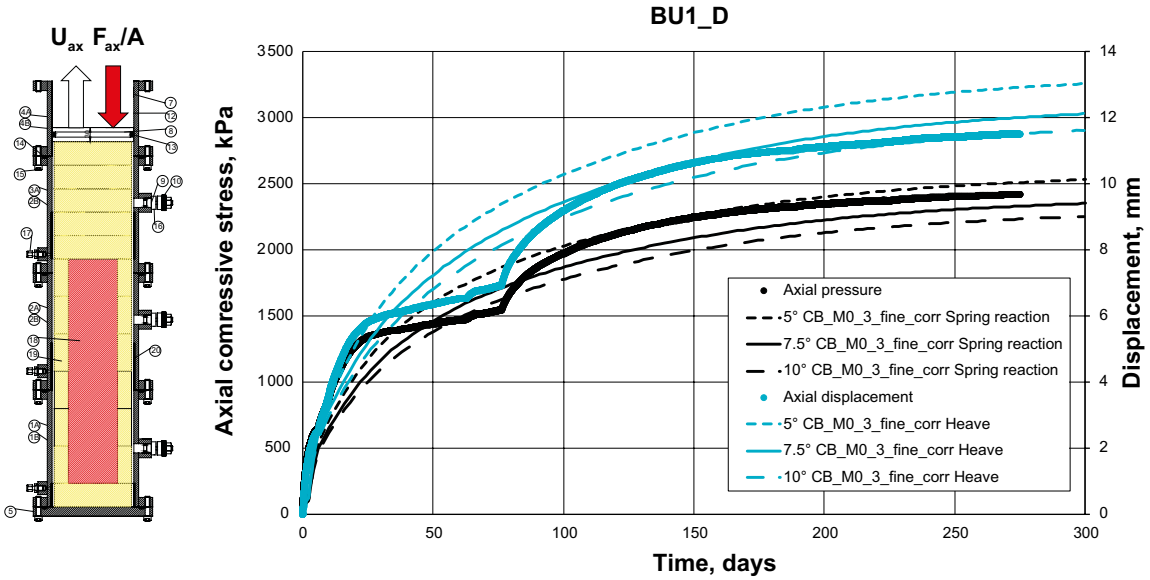

Figure 7-22. *Axial plug displacement and pressure. Thick lines: experimental data, thin lines: model data.*

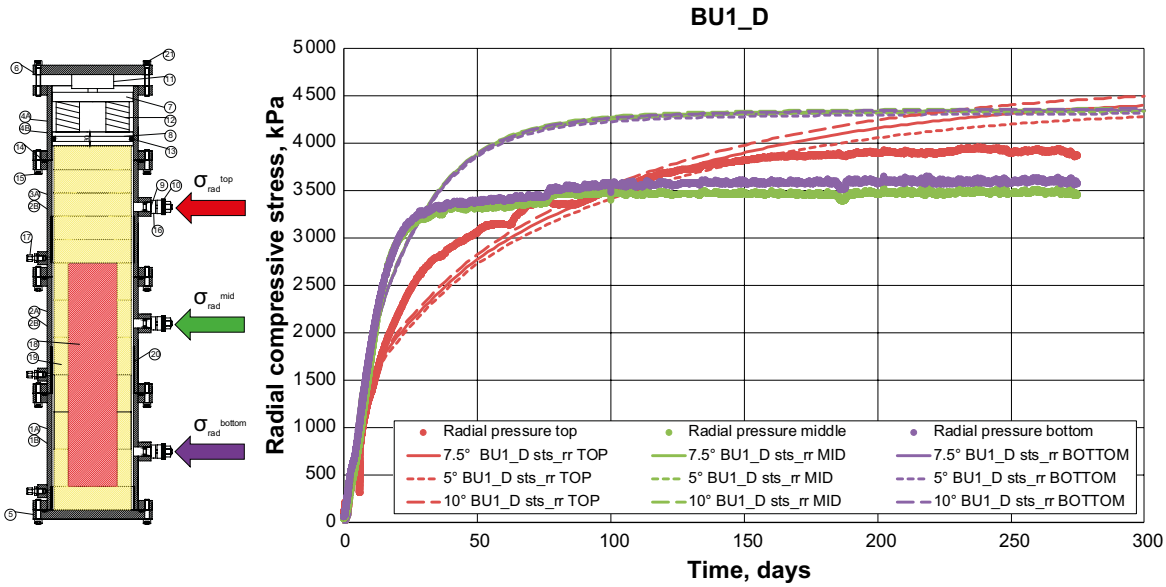

Figure 7-23. *Radial total stresses. Thick lines: experimental data, thin lines: model data.*

7.4.2 Simulation of BU5_E3

In this chapter, results following from solving the problem formulation as described by the BU5_E3 model are shown and discussed. Just as a reminder, the E3 filter layout meant that water was introduced along the lower 5 cm of the vertical boundary. First out is a comparison with operational data, then follows a prediction of the state after 411 days of operation (the estimated time until dismantling) which is compared to excavation data.

Comparisons with operational data

Accumulated water uptake

It should again be remembered that the method used when calculating the accumulated water inflow (post-process integration of the fluxes from an output-file) make this result less accurate as compared to other. The trend of the model output agrees well with the experimental data, but the magnitude is overestimated.

Plug displacement and plug pressure

The agreement between the model and experiment for both mechanical entities suggests that the overall mechanical setup of the model is reasonable. The combination of overestimated water inflow together with the nice agreement in mechanical responses, however, indicates that the HM-coupling could be somewhat deficient for this case.

Radial total stresses

Calculated radial stresses agree well with experimental data. The relative relation of the curves within the set is well captured. The trend of the stress evolution at the bottom position is not exactly correct, but the overall magnitude agrees well with sensor data.

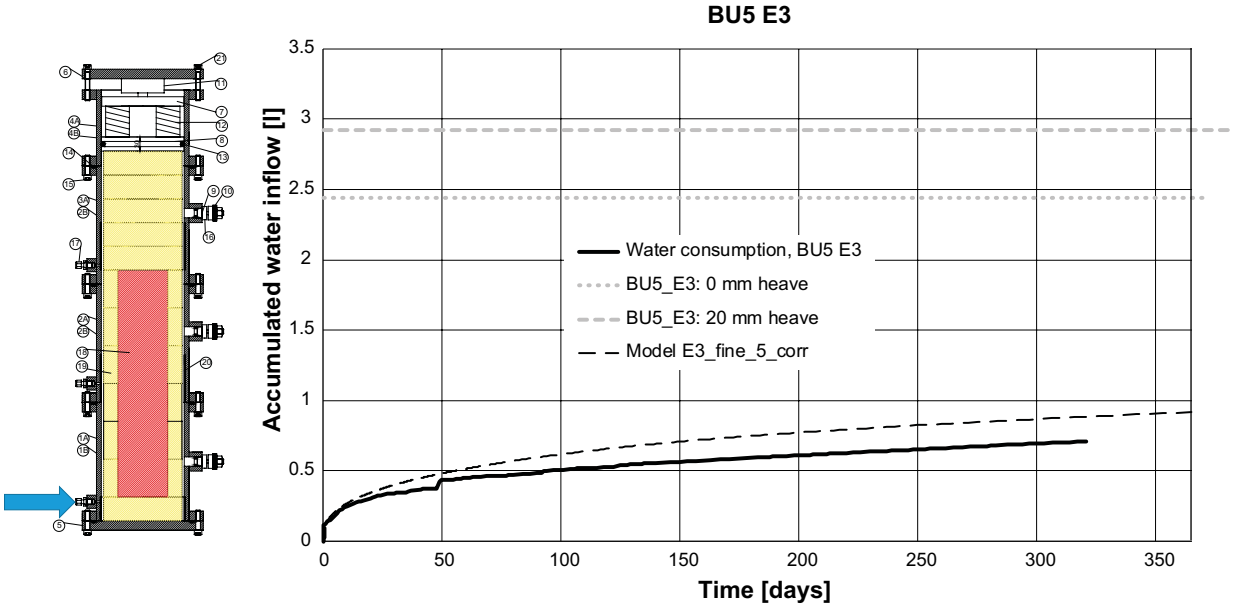

Figure 7-24. *Accumulated water inflow. Solid line: experimental data, hatched black line: model output, dotted/hatched grey lines: available volume for water at 0 mm/20 mm heave, respectively.*

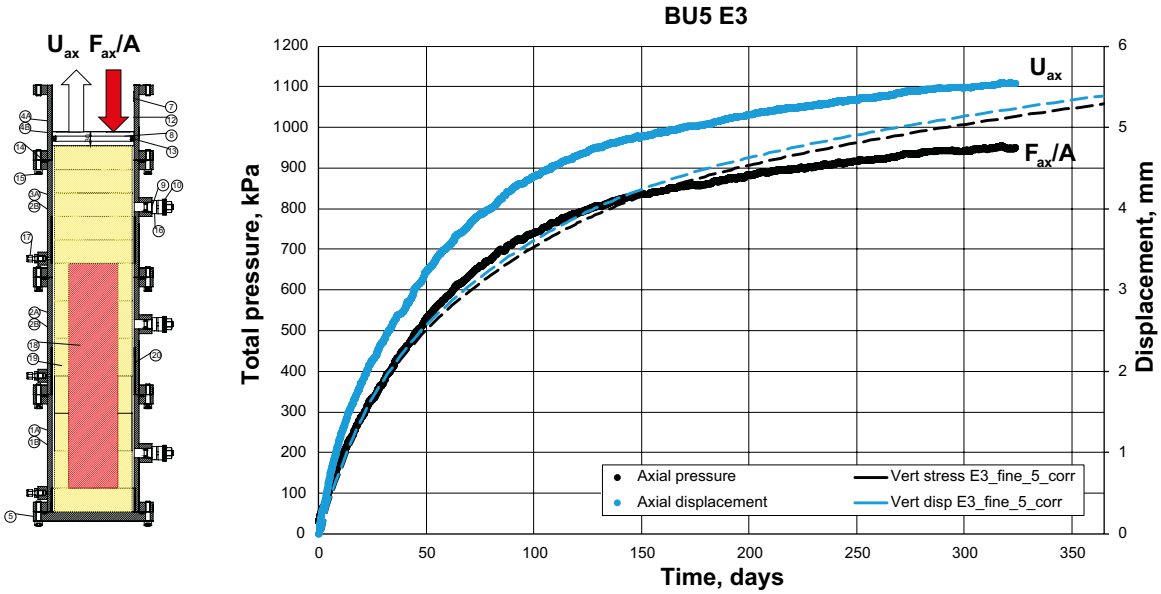

Figure 7-25. *Axial plug displacement and pressure. Thick lines: experimental data, thin lines: model output.*

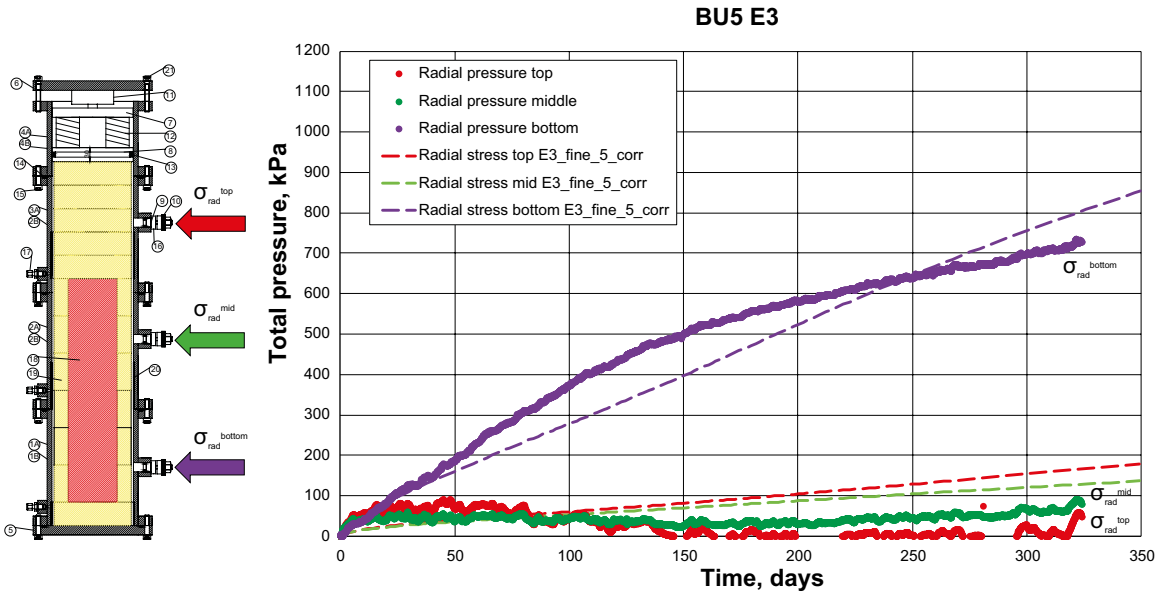

Figure 7-26. *Radial total stresses. Thick lines: experimental data, thin lines: model output.*

Predicted state at dismantling

At the time when performing the simulation, the test was still in operation. The duration of the test was estimated to be from 2018-07-03 to 2019-08-18, thus for 411 days. It turned out to be 405 days in the end, but the difference of 6 days should not affect the solution to a large degree.

The unrepresentative high stiffness about the top right corner, due to the artefact present in the model, should again be remembered. The solution about this point should therefore not be relied upon to the same degree as for the rest of the model.

The predicted state at day 411 is compared to what was obtained at the actual excavation at day 405 in terms of contour plots of degree of saturation Figure 7-27, contour plots of dry density Figure 7-28, and profiles of dry density at different heights Figure 7-29.

The maps of degree of water saturation shown in Figure 7-27 have a nice agreement. The hatched lines divide the map into "block" sections (the outer pellet slot is not included) with the ranges indicated. As can be seen, the position of the lines and the ranges agree well between the simulation and excavation data.

Again as for BU1_D, when studying the maps of dry density, shown in Figure 7-28, the overall appearance of the maps will be focused on rather than comparing values since this information is better studied using the profiles of dry density at different heights shown in Figure 7-29.

The agreement between the dry density maps regarding overall appearance is satisfying. At the bottom of the canister the buffer has homogenized radially and has swollen axially as to obtain a low dry density. Iso-lines of comparable values have been indicated to facilitate comparison. Otherwise the dry density has not changed much from the state at the installation.

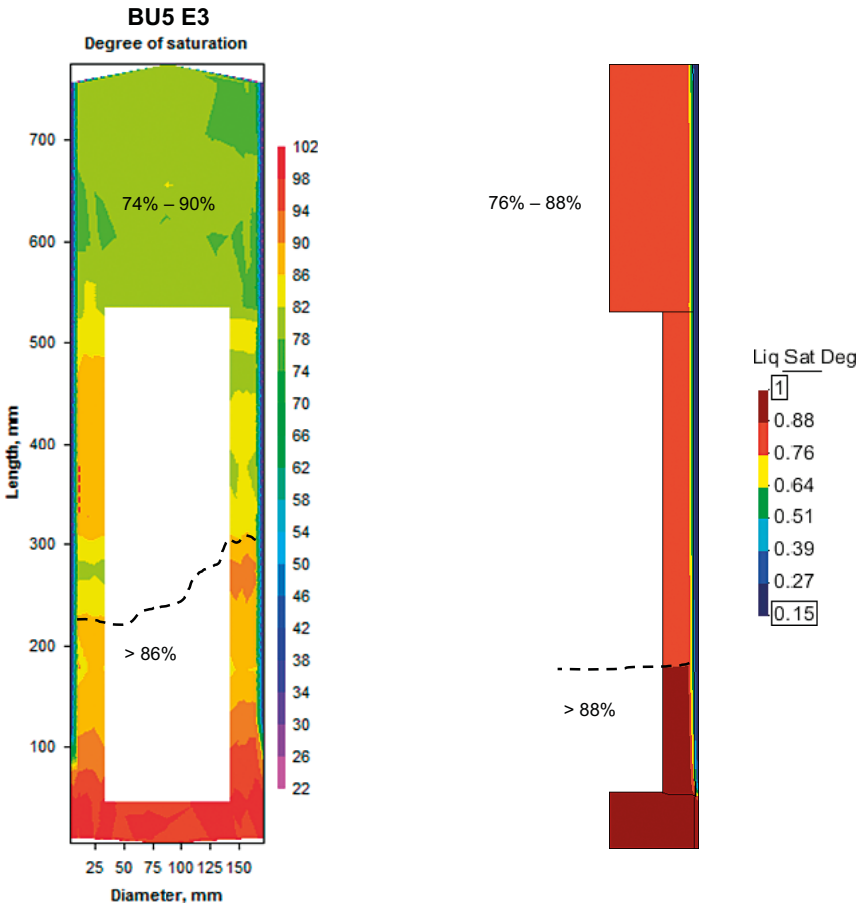

Figure 7-27. *Maps of degree of saturation obtained from analysing excavated samples (left) and the simulation (right).*

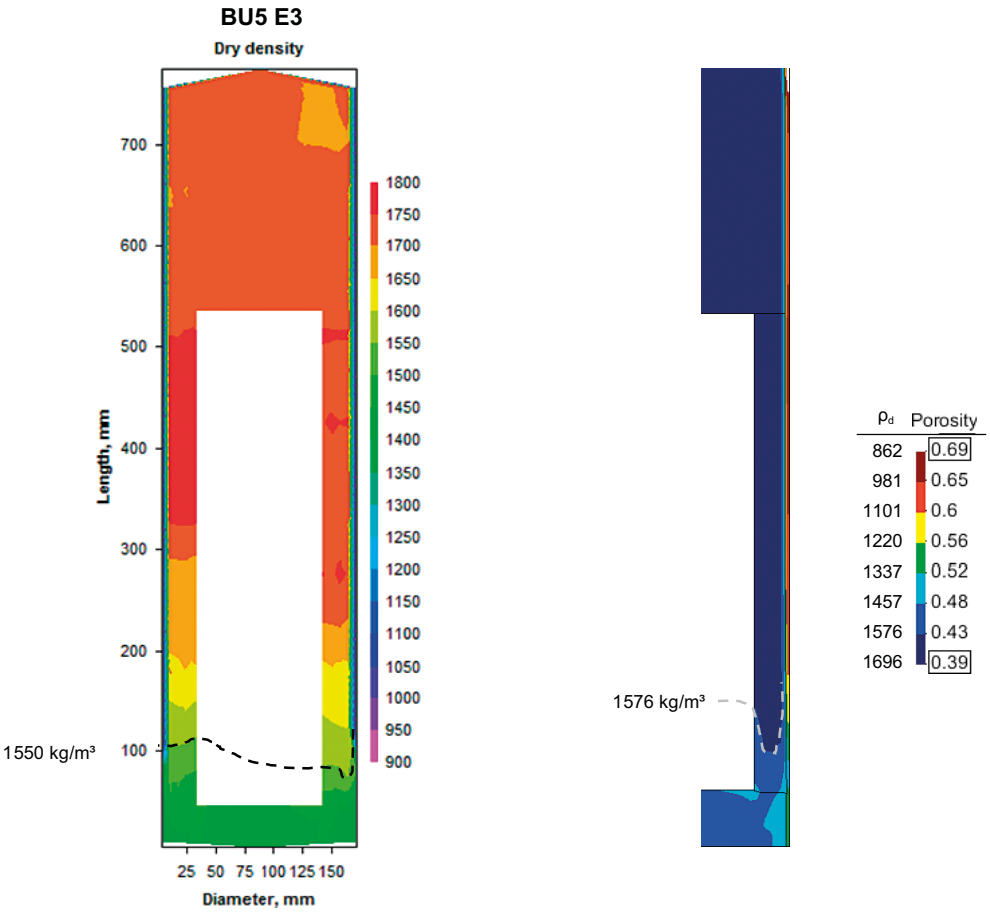

Figure 7-28. *Maps of dry density obtained from analysing excavated samples (left) and the simulation (right).*

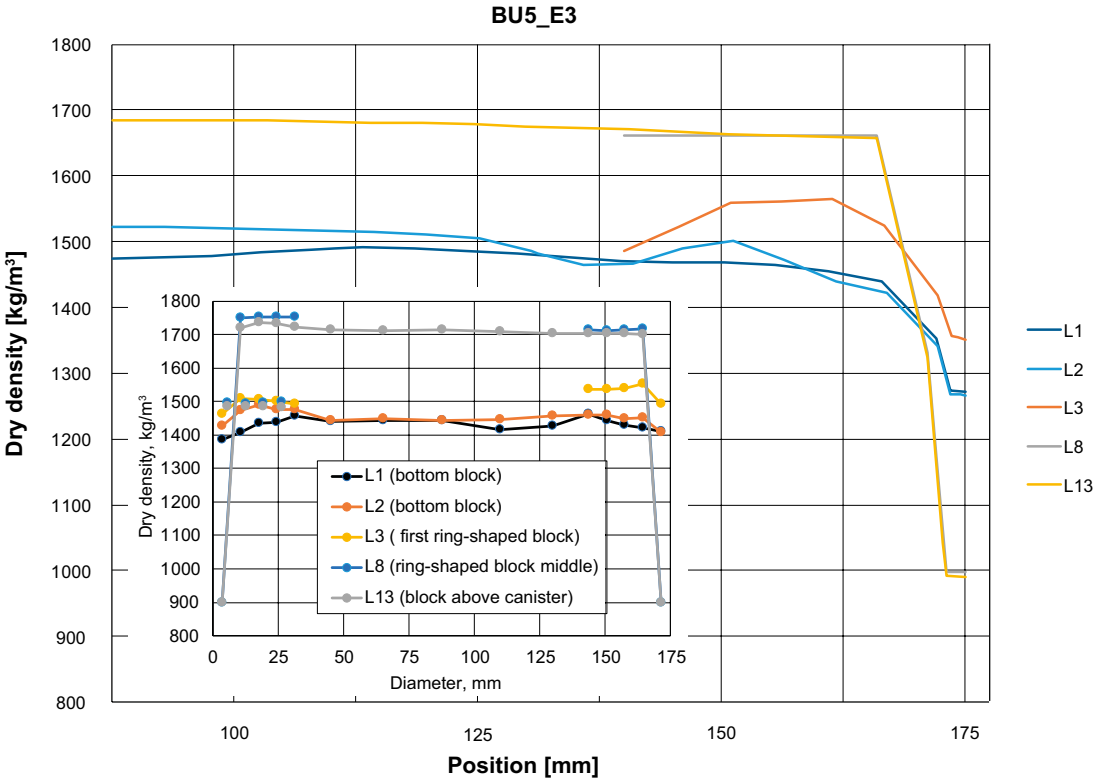

Figure 7-29. *Predicted dry density profiles of the buffer after 411 days of operation (large diagram) and excavation data after 405 days (small diagram).*

As mentioned above, when comparing values of dry density between the excavation data and simulation, profiles of dry density at different heights are used, see Figure 7-29. The larger diagram contains results from the simulation and the inserted smaller diagram contains the excavation data. The density profiles can be compared to 1 590 kg/m^3, the calculated average dry density obtained at installation. In the model the radially homogenized dry density was 1 569 kg/m^3 and 1 607 kg/m^3, for ring-shaped and cylinder-shaped block sections, respectively.

The overall agreement between the two sets of curves is good. The positions of the profiles relative to each other within the two sets are alike. The profiles for L1, L2 and L3, sections positioned at the bottom of the buffer, show somewhat larger remaining heterogeneity for the simulation as compared to the experimental data but the values are similar. Some difference in heterogeneity could be expected since the values from the experiment are obtained for a sample volume, i.e., an average for the volume, and not a point as in the case of the simulation. The profiles for L8 and L13, sections at the canister mid and just above the canister, respectively, show that nothing much has happened concerning the dry density distribution at the upper parts of the experiment.

7.4.3 Simulation of water supply layout D and E3 using a KBS-setup

As mentioned before, comparisons between models of experiments BU1_D and BU5_E3 were complicated by the difference in initial dry density of the pellet filled slot. So, in order to facilitate a direct comparison between models using water supply layout D and E3, a new pair of models were developed where the initial dry density of the pellet slot was chosen according to the KBS-3V design.

These simulations of fictive scale tests were run as to become “sufficiently close to” equilibrium. The different water supply layouts required significantly different simulated operational time as to get close to equilibrium. The KBS_D model simulated 10 years of operation whereas the KBS_E3 model simulated 400 years of operation. The states at the end of the simulations will be denoted final states of the systems.

To get a picture of how the two cases differ it seems natural to begin with the water transport and saturation process. To analyse this, isoline plots over the water pressure (in the present models = 0.1 − suction) are instructive. This is so since the water flux is driven by gradients in water pressure (suction) and the water inlet hydraulic boundary condition is expressed in terms of water pressure, 0.1 MPa along different sections of the boundary as described earlier. Figure 7-30 shows water pressure isobars for the two different simulated filter layouts. Two states are shown for each model, the first after 100 days and the second later on in order to show the evolution of the field.

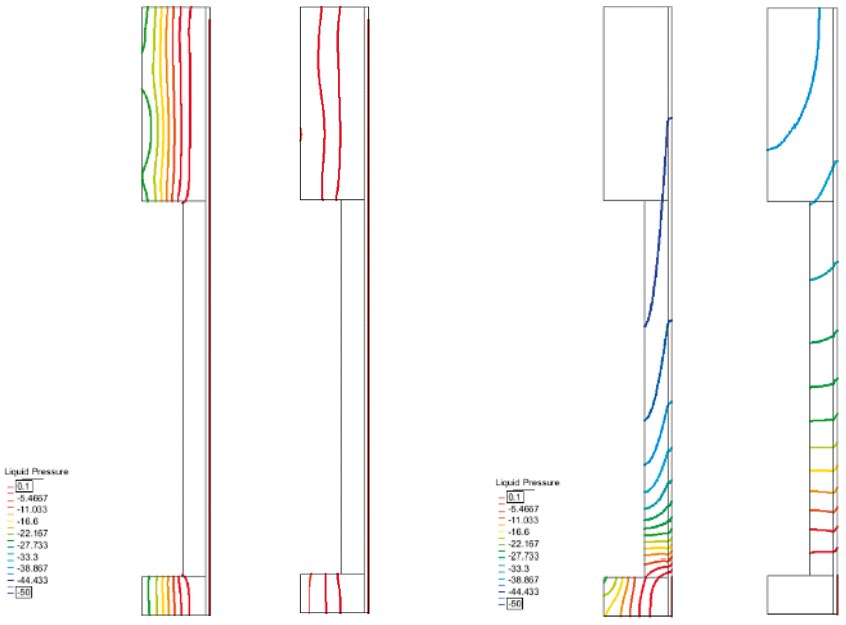

KBS_D: Isobars at 100 and 150 days KBS_E3: Isobars at 100 and 1000 days

Figure 7-30. *Water pressure isobars (MPa) of the KBS_D and KBS_E3 models at the indicated times.*

Comparing the plots after 100 days give a good overview of differences of the models. In KBS_D water flows more or less radially inwards from the entire boundary. In KBS_E3 water also flows more or less radially inwards at the bottom where the simulated filter is situated. Above the filter, however, the water flow has a dominating axial/upwards component and it is only at some height above the filter that a radial component starts to be visible. The radial component of the flow in the upper part increases more and more further away from the inlet. The plots at later times show lower pressure gradient magnitudes, thus less flow. KBS_D shows the same radially directed flow whereas KBS_E3 has less of a radially directed flow component for the plot later in time as compared to the one at 100 days.

Next, the axial deformation (swelling) of the buffer is studied. To do this, isoline plots over the axial displacements at 100 days and the final states are given for both models in Figure 7-31.

The appearance of the axial displacement field is clearly significantly different for the two cases, not only in terms of magnitude. After 100 days the KBS_D model has the major part of the axial displacements occurring above the canister, the opposite applies for KBS_E3. Another significant difference is the relative axial displacement between the buffer blocks and outer boundary which is clearly visible for the KBS_E3 model and not so for the KBS_D model.

At the final state of the KBS_D model the axial displacement field over the entire buffer resembles that obtained after 100 days except for a shift in magnitude. This is not the case for KBS_E3. Whereas the axial displacement field below the canister has not changed significantly between 100 days and the final state, much have changed above the canister when this part has taken up water and has swollen.

In short, the differences in appearances come from HM-processes being simultaneous (KBS_D) or sequential (KBS_E3) for different parts of the system. When a section of PS-material takes up water and swells, the friction against the wall increases and thereby prohibits vertical mechanical action between material above and below of it. The effect of this, in the present case, can the thought of as if in KBS_D, the hydromechanical process takes place under more confined conditions as compared to KBS_E3.

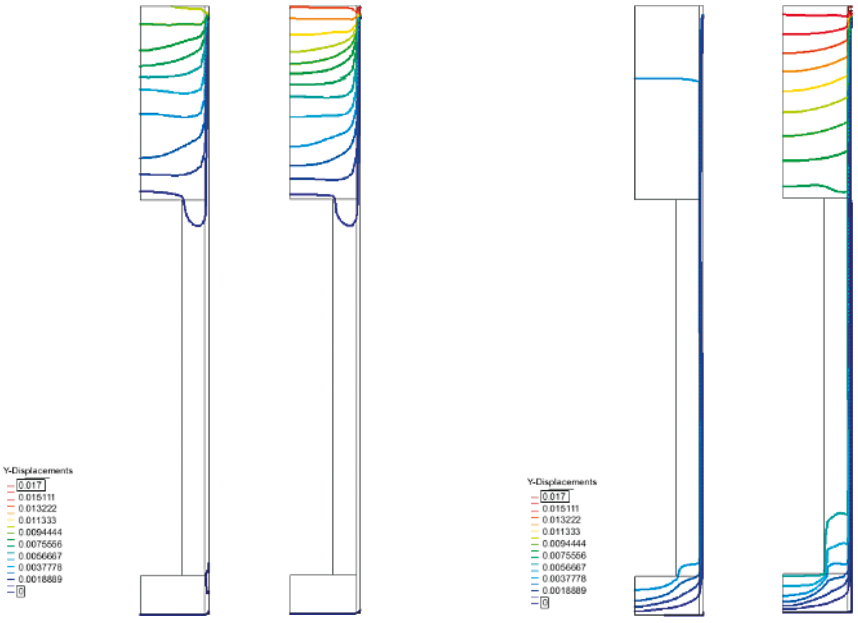

KBS_D: 100 days and final state (10 years)

KBS_E3: 100 days and final state (400 years)

Figure 7-31. *Iso maps of axial displacements (m) of the KBS_D and KBS_E3 models at the indicated times.*

The final states of the models are compared in terms of some chosen parameters which could be interesting with respect to safety of a deposition hole of KBS-3V design. Table 7-11 contains final state variables of the KBS_D and KBS_E3 models. The "plug mechanics", which should translate to mechanical interaction of materials within the deposition hole and deposition tunnel in the full-scale case, is described in terms of plug heave and plug pressure. KBS_E3 gives higher heave and pressure as compared to KBS_D due to the more unrestricted (less friction resistance) initial swelling of the block material close to the water inlet. The same process gives rise to significantly different canister heave and minimum/maximum values of the pressure and dry density fields, shown in Figure 7-32, as well.

Table 7-11. Overview of variables "at equilibrium" of the KBS_D and KBS_E3 models.

Variable	KBS_D	KBS_E3
Plug heave [mm]	14	17
Plug pressure [MPa]	2.8	3.3
Canister heave [mm]	0.9	6.7
Pressure min/max [MPa]	5.1 / 9.0	2.5 / 7.3
Dry density min/max [kg/m^3]	1 497 / 1 646	1 402 / 1 621

Another issue which are important for safety reasons is the mechanical action from the buffer on the canister. As an example, in Figure 7-33, the normal compressive stress acting on the canister surface is shown as a function of the indicated coordinates along the canister surface. This type of data could serve as input for the design of the canister or for checking that given criteria are fulfilled for different cases. In the present study, KBS_D generates higher magnitudes of normal compressive stresses. This is in line with thinking about this case as taking place under more confined conditions.

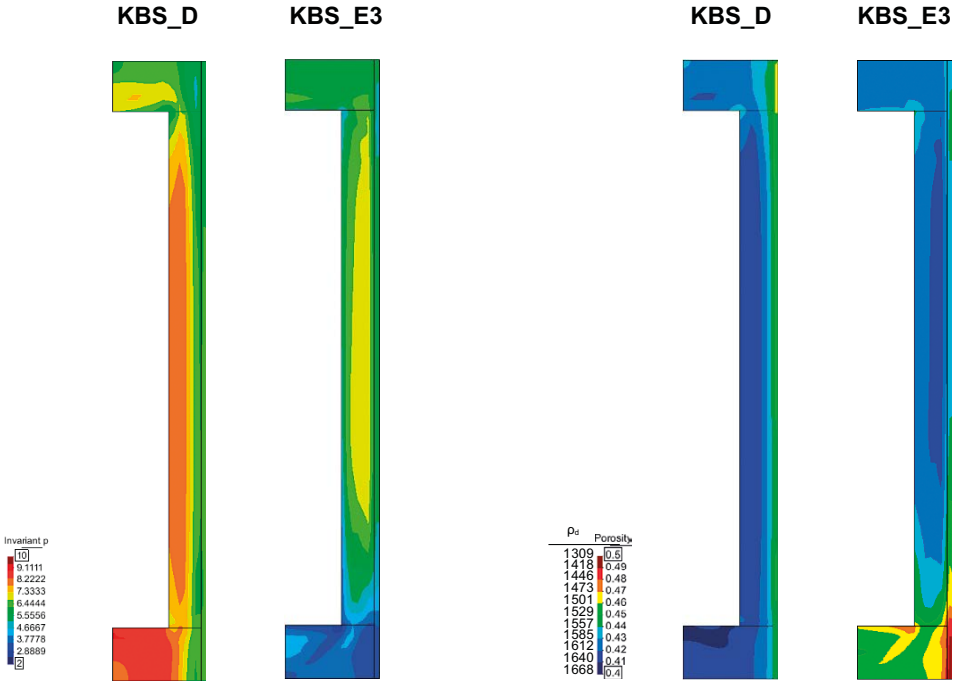

Figure 7-32. *Maps of pressure and dry density in the buffer volume of the KBS_D and KBS_E3 models at the final states.*

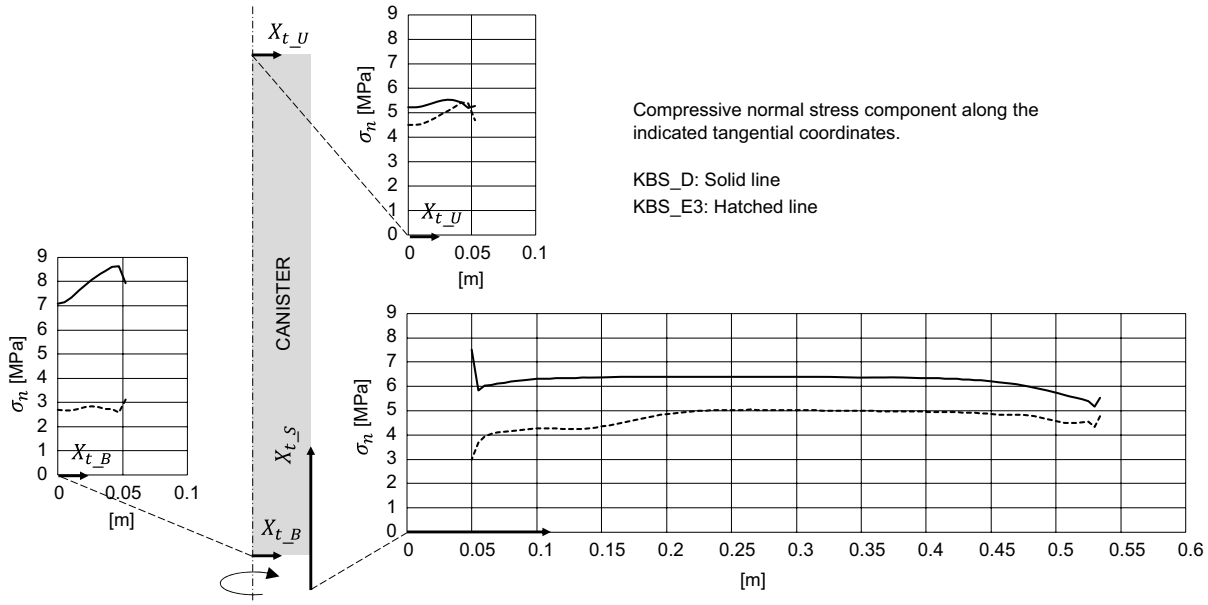

Figure 7-33. *Profiles of the compressive normal stress component along the indicated tangential coordinates aligned with the canister surface.*

7.5 Comments and conclusions

The described models could, for BU2_D as well as BU5_E3, capture the HM-processes properly during operation and also properly predict the states at excavation. The models used the same setup for the block materials. Due to a large difference between the two tests in terms of initial dry density of the pellet filled slot, the corresponding material model setup had to be changed regarding retention and mechanical properties between the models.

The study of the additional KBS_D and KBS_E3 models, directed towards investigating the sole effect from using different water supply layouts, proved to be valuable. In short, it was found that differences between the water supply layouts originate from HM-processes being simultaneous (KBS_D) or sequential (KBS_E3) for different parts of the system. When a section of pellet slot material takes up water and swells, the friction against the wall increases and thereby prohibits vertical mechanical action between material above and below of it. The effect of this, in the present case, can be thought of as if in KBS_D, the hydromechanical process takes place under more confined conditions as compared to KBS_E3.

KBS_E3 gave higher heave and plug pressure as compared to KBS_D due to the more unrestricted (less friction resistance) initial swelling of the block material close to the water inlet. The same process gave rise to significantly different canister heave and minimum/maximum values of pressure and dry density fields as well. Due to the more confined KBS_D model the normal stress acting on the canister was also higher for this case.

An investigation of the internal shearing properties of the block material and “external” pellets/steel interface shearing properties gave new insights of how to improve the setup of the corresponding mechanical material model.

A 1D-model of a buffer cross-section was used to investigate the radial homogenization process and the resulting dry density profile at full water saturation. This study gave that it was beneficial to change one parameter in the mechanical model of the block (P_{ref}) in order to obtain representative dry density profiles.

7.5.1 Uncertainties/future investigations

Since the water supply layout turned out to be a factor which affected the system significantly, other layouts should be investigated in order to assure that there is not another case which does produce results which are worse in a safety perspective. A potentially problematical water supply layout is one where water enters about the canister top.

In this first stage only smaller scale geometries have been used. In order to have full confidence in that results are valid at full scale (are fully scalable); full scale models should be developed.

The retention relation for block materials could be improved further. The moisture diffusivity analysis indicated that the block retention curve overestimated the suction for a given degree of water saturation. The retention curve could also be made dependent on porosity in order to account for the HM-coupling in retention.

In the present models the buffer has been assumed perfectly bonded to the canister. It worked out well when designing a special material for the pellet filled slot, where friction at the interface between the pellet filled slot and the hole wall interface were accounted for. This method could also be tested for the interface between block and canister.

The assumption made regarding the *p-q* relation, that it is relevant also for unsaturated conditions, should be considered an uncertainty in the present analysis.

In addition, the influence of temperature should be investigated by including a heated canister. This is however judged not to affect the upwards swelling.

8 New design of deposition tunnels

The present reference design with drill and blast excavated tunnels according to Chapter 2 may be changed since SKB has made a targeting decision to instead use mechanical rock excavation to produce deposition tunnels. Three different tunnel profiles have been evaluated, see schematic drawings provided in Figure 8-1 and Figure 8-2. The main new alternative is the tunnel profile presented in Figure 8-1, alternative A.

There will of course be an influence on the results derived from the project described in this report if the design of the tunnel will be changed. The influence of such new tunnel profiles and different backfill designs on the buffer swelling issue has not yet been investigated in this project. However, some general comments are provided below:

- The new suggested tunnel profiles have a higher block filling degree, between 75.9 and 83.1 %, compared to the present reference design which have a block filling degree of about 73 %, see description in Section 2.2. This is in general positive to prevent buffer swelling.
- The height of the new suggested tunnel profiles is somewhat lower compared to the reference design. This is also a factor that in general is positive to prevent the buffer swelling.
- The most important factor influencing the backfill resistance regarding buffer swelling is the thickness of the pellet filled layer at the floor. In the tunnel profile of alternative A, Figure 8-1, the blocks are close to the walls but the thickness of the pellet layer on the floor is 150 mm (maximum thickness according to reference design is 100 mm). One improvement may be to let the uppermost buffer block end 50 mm above the deposition hole.
- The thickness of the pellet layer at the ceiling is also important. In the tunnel profile of alternative A, Figure 8-1, there is a large gap at the top, with a width of 450 mm. This gap is in the same range as in the present reference design where it is between 300 and 500 mm, depending on if it is the nominal tunnel area or if there is overbreak. The thick pellet layers both at the floor and the ceiling means that the improvement regarding the upward swelling of the buffer by using the alternative A tunnel design is limited.
- The other two tunnel profiles suggested, Figure 8-2, have a relation between the block stacks and the tunnel peripheries that are believed to be more favourable regarding the buffer swelling issue. The blocks in these designs are piled so that the remaining gap between block stack and ceiling is smaller compared to both the alternative A tunnel design and the present reference design.
- All three tunnel profiles are suggested to have a block stack where the lower block corners are in contact with the rock surface. This is probably not possible in the real case and it is recommended that the block stack pattern for these tunnel profiles should be updated. This will probably result in a decreased block filling degree and an increase of the thickness of the pellet layer on the floor.
- It should be mentioned, that there are discussions ongoing regarding if it is necessary to fill the gaps between blocks and rock with pellets. If e.g. the volume above the block stack is left empty, this will worsen the situation additionally regarding the upwards swelling.
- In general, it appears as the tunnel alternative C is the best in order to hinder buffer swelling since the slots between the block stack and the floor and ceiling respectively can be made smaller than in the other alternatives.

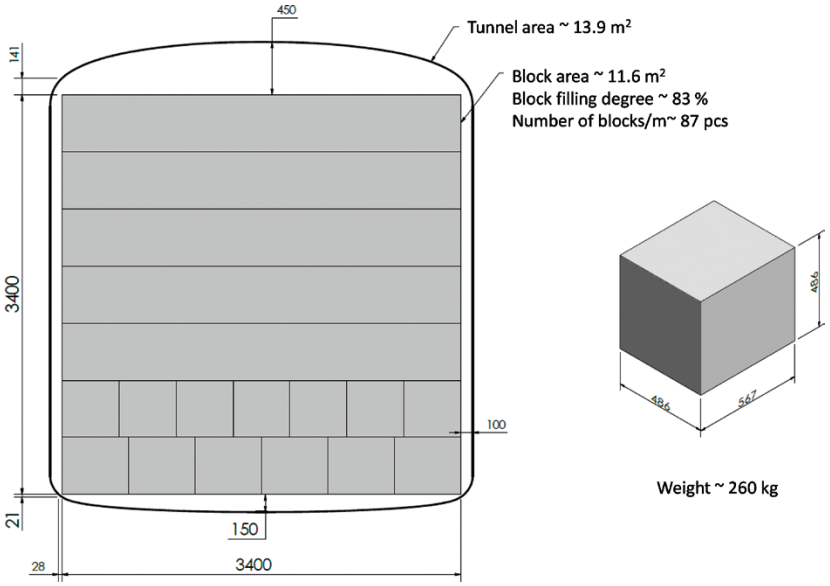

Figure 8-1. *The obtained tunnel profile and the planned block filling of alternative A, the main alternative.*

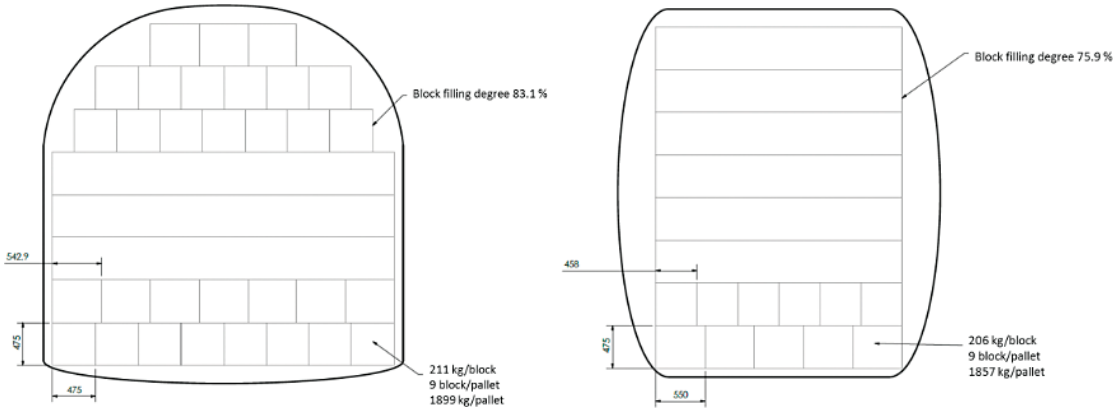

Figure 8-2. *Left: Alternative tunnel profile B and the planned block filling. Right: Alternative tunnel profile C and the planned block filling.*

9 Summary of results and conclusions

9.1 General

A large amount of interesting results from the laboratory tests, the scale tests and the modelling have been generated. Some analyses and conclusions have been made in the different chapters, but a general deeper analysis of the combined knowledge has not yet been made but should be a task in the continuation of the project.

Some preliminary conclusions from the performed laboratory tests and modelling are provided below:

- **Deposition tunnel tests in scale 1:20.** The results from the compression tests clearly show that the case with a completely dry backfill results in the largest displacements of the swelling buffer. Access to water results in that the backfill becomes stiffer. Backfill that have had access to water for long time will homogenize and is probably getting stiffer with time. In addition, there will be a swelling pressure from the backfill that will further hinder upswelling.
- **Modelling of the deposition tunnel tests.** The reasonable agreement obtained between modelling results and measurements in both the lab-scale test and the full-scale Buffer swelling test shows that 3DEC is a suitable modelling tool for this type of problem. However, there are a number of uncertainties (e.g., small-strain approximation, boundary conditions, material models and parameter values) that may need to be addressed in future studies in order to additionally improve the models.
- **Deposition hole tests in scale 1:10.** The performed scale tests have proven to be suitable for this kind of investigations. The results from the tests show that one important factor influencing the results strongly is the water supply layout. A water inflow at the bottom of the deposition hole, while the rest of the hole is dry, will result in a large heave of the buffer depending on local swelling of the bottom block. The final dry density of the bottom block will be low and corresponds for the test case to a mean swelling pressure of below 3 MPa.
- **Modelling of the deposition hole tests.**

The described models could capture the HM-processes properly during operation and also properly predict the states at excavation.

Since the water supply layout turned out to be a factor which affected the system significantly, other layouts should be investigated in order to assure that there is not another case which does produce results which are worse in a safety perspective. A potentially problematical water supply layout is one where water enters around the canister top.

9.2 Consequences when considering the present reference design

9.2.1 Compliance with requirements

There are several technical design requirements on the buffer and on the backfill specified in Posiva SKB (2017) e.g. regarding the dry density yielding a certain swelling pressure, hydraulic conductivity and shear strength. In the present report investigations have been made regarding the compression of the backfill and the upwards swelling of the buffer at different wetting scenarios. The requirement regarding the deformation properties is formulated according to the following:

"*The overall deformation of the installed backfill both in dry and saturated state shall resist the swelling pressure from the buffer and maintain the buffer swelling pressure > 3 MPa in average over the buffer volume*". The buffer volume extends from the bottom of the deposition hole to a distance of 500 mm above the canister.

The two tests performed simulating a buffer swelling against a dry backfill consisting of blocks and pellets (according to the reference design) showed that if the buffer is wetted in an adverse way, parts of the buffer will end up with a rather low density and thereby also locally a low swelling pressure. In the BU5_E3 test, the buffer only had access to water at the periphery of the bottom block below the canister. This resulted in that the bottom block swelled and pushed the canister and the other blocks

upwards. The swelling resulted in a rather low density of the bottom block corresponding to a mean swelling pressure of between 2.2 to 2.6 MPa. The average dry density of the buffer volume was, however, high enough to fulfil the swelling pressure requirement (mean swelling pressure 3.8 MPa). It is recommended that also other possible adverse wetting scenarios are investigated in the future.

9.2.2 Requirements on the backfill blocks

The backfill blocks used in the full-scale Buffer Swelling test at Äspö HRL (Sandén et al. 2017) had a dry density of between 1 650 and 1 680 kg/m^3. It was observed that these blocks cracked easily during the simulated buffer heave (above and around the deposition hole) and thereby couldn't transfer the applied pressure further up in the block stack. It was therefore concluded that the strength of these blocks was too low.

The model backfill blocks used in the scale tests described in this report had a bulk density of 2 064 kg/m^3 and a dry density of about 1 720 kg/m^3. The water content was 20 %. The strength of these backfill blocks has been investigated with two different types of tests: Beam tests and Uniaxial compression tests. The beam tests showed that the tensile strength of the new backfill blocks were much higher (800–1 200 kPa) than the tensile strength of the full-scale blocks (100 and 500 kPa). The Uniaxial compression tests showed similar behaviour. The uniaxial compression strength of the blocks was between 2 300 and 4 500 kPa compared to between 1 000 and 2 500 kPa for the full-scale blocks. The increased density and water content of the new blocks have thus influenced the block strength evidently.

It is thus recommended that backfill blocks should have a water content of about 20 % and a dry density of about 1 720 kg/m^3. The strength of the blocks should be at least 3 MPa (uniaxial compression tests) in order to withstand the upwards swelling of the buffer without cracking.

9.3 Uncertainties and recommendations for further work

Deeper analyses of all results and information gained from the reported tests and modelling should be done as the base for planning of additional tests and modelling. E.g. the upscaling from the scale tests to full scale should be further analysed.

Some conclusions, uncertainties and recommendation for further work have been included at the end of the modelling chapters:

Since the water supply layout turned out to be a factor which affected the system significantly, other layouts should be investigated in order to assure that there is not another case which does produce results which are worse in a safety perspective. A potentially problematical water supply layout is one where water enters around the canister top.

In this first stage only smaller scale geometries have been used in the modelling of the buffer. In order to have full confidence in that results are valid at full scale (are fully scalable); full scale models should be developed.

The retention relation for the buffer block materials could be improved further. The moisture diffusivity analysis indicated that the block retention curve overestimated the suction for a given degree of water saturation. The retention curve could also be made dependent on porosity in order to account for the HM-coupling in retention.

In the present models the buffer has been assumed perfectly bonded to the canister. It worked out well when designing a special material for the pellet filled slot, where friction at the interface between the pellet filled slot and the hole wall interface were accounted for. This method could also be tested for the interface between block and canister.

In addition, the influence of temperature should be investigated by including a heated canister. However, this is judged not to affect the upwards swelling.

More work should be done to improve the general agreement between models and measurements of the backfill models and to test to what extent upscaling results from lab-scale to full scale is possible.

References

SKB's (Svensk Kärnbränslehantering AB) publications can be found at www.skb.com/publications. SKBdoc documents will be submitted upon request to document@skb.se.

Alcoverro J, Alonso E, 2001. Scientific bases of Code_Bright, UPC 70-UPC-L-1-001: 1-12, Universitat Politècnica de Catalunya. SKBdoc 1918618 1.0, Svensk Kärnbränslehantering AB.

Andersson L, Sandén T, 2012. Optimization of backfill pellet properties. ÅSKAR DP2. Laboratory tests. SKB R-12-18, Svensk Kärnbränslehantering AB.

Arvidsson A, Josefsson P, Eriksson P, Sandén T, Ojala M, 2015. System design of backfill. Project results. SKB TR-14-20, Svensk Kärnbränslehantering AB.

Börgesson L, Johannesson L-E, Hernelind J, 2003. Earthquake induced rock shear through a deposition hole. Effect on the canister and the buffer. SKB TR-04-02, Svensk Kärnbränslehantering AB.

Börgesson L, Hernelind J, 2014. Modelling of the mechanical interaction between the buffer and the backfill in a KBS-3V repository. Updated design of backfill and deposition hole. SKB R-14-21, Svensk Kärnbränslehantering AB.

Börgesson L, Hernelind J, 2017. Modelling of the mechanical interaction between the buffer and the backfill in KBS-3V. Modelling results 2015. SKB TR-16-08, Svensk Kärnbränslehantering AB.

Dueck A, 2010. Thermo-mechanical cementation effects in bentonite investigated by unconfined compression tests. SKB TR-10-41, Svensk Kärnbränslehantering AB.

Dueck A, Johannesson L-E, Kristensson O, Olsson S, 2011. Report on hydro-mechanical and chemical-mineralogical analyses of the bentonite buffer in Canister Retrieval Test. SKB TR-11-07, Svensk Kärnbränslehantering AB.

Glamheden R, Fälth B, Jacobsson L, Harrström J, Berglund J, Bergkvist L, 2010. Counterforce applied to prevent spalling. SKB TR-10-37, Svensk Kärnbränslehantering AB.

Itasca, 2016. 3DEC – 3-Dimensional Distinct Element Code. User's guide, v. 5.2. Minneapolis, MN: Itasca Consulting Group Inc.

Leoni M, Börgesson L, Keto P, 2018. Numerical modelling of the buffer swelling test in Äspö HRL. Validation of numerical models with the buffer swelling test data. SKB TR-17-03, Svensk Kärnbränslehantering AB.

Posiva SKB, 2017. Safety functions, performance targets and technical design requirements for a KBS-3V repository. Conclusions and recommendations from a joint SKB and Posiva working group. Posiva SKB Report 01, Posiva Oy, Svensk Kärnbränslehantering AB.

Sandén T, Olsson S, Andersson L, Dueck A, Jensen V, Hansen E, Johnsson A, 2014. Investigation of backfill candidate materials. SKB R-13-08, Svensk Kärnbränslehantering AB.

Sandén T, Andersson L, Jensen V, 2015. System design of backfill. Full scale production test of backfill blocks. SKB P-14-24, Svensk Kärnbränslehantering AB.

Sandén T, Nilsson U, Andersson L, 2016. Investigation of parameters influencing bentonite block quality. Laboratory investigation. SKB P-16-06, Svensk Kärnbränslehantering AB.

Sandén T, Börgesson L, Nilsson U, Dueck A, 2017. Full scale Buffer Swelling Test at dry backfill conditions in Äspö HRL. In situ test and related laboratory tests. SKB TR-16-07, Svensk Kärnbränslehantering AB.

Sellin P (ed), Åkesson M, Kristensson O, Malmberg D, Börgesson L, Birgersson M, Dueck A, Karnland O, Hernelind J, 2017. Long re-saturation phase of a final repository. Additional supplementary information. SKB TR-17-15, Svensk Kärnbränslehantering AB.

SKB, 2010a. Design and production of the KBS-3 repository. SKB TR-10-12, Svensk Kärnbränslehantering AB.

SKB, 2010b. Design, production and initial state of the backfill and plug in deposition tunnels. SKB TR-10-16, Svensk Kärnbränslehantering AB

SKB, 2010c. Design, production and initial state of the buffer. SKB TR-10-15, Svensk Kärnbränslehantering AB

Svensson D, Dueck A, Nilsson U, Olsson S, Sandén T, Lydmark S, Jägerwall S, Pedersen K, Hansen S, 2011. Alternative buffer material. Status of the ongoing laboratory investigation of reference materials and test package 1. SKB TR-11-06, Svensk Kärnbränslehantering.

Åkesson M, Börgesson L Kristensson O, 2010. SR-Site data report. THM modelling of buffer, backfill and other system components. SKB TR-10-44, Svensk Kärnbränslehantering AB.

Appendix 1

Results from sampling of Test 2–4

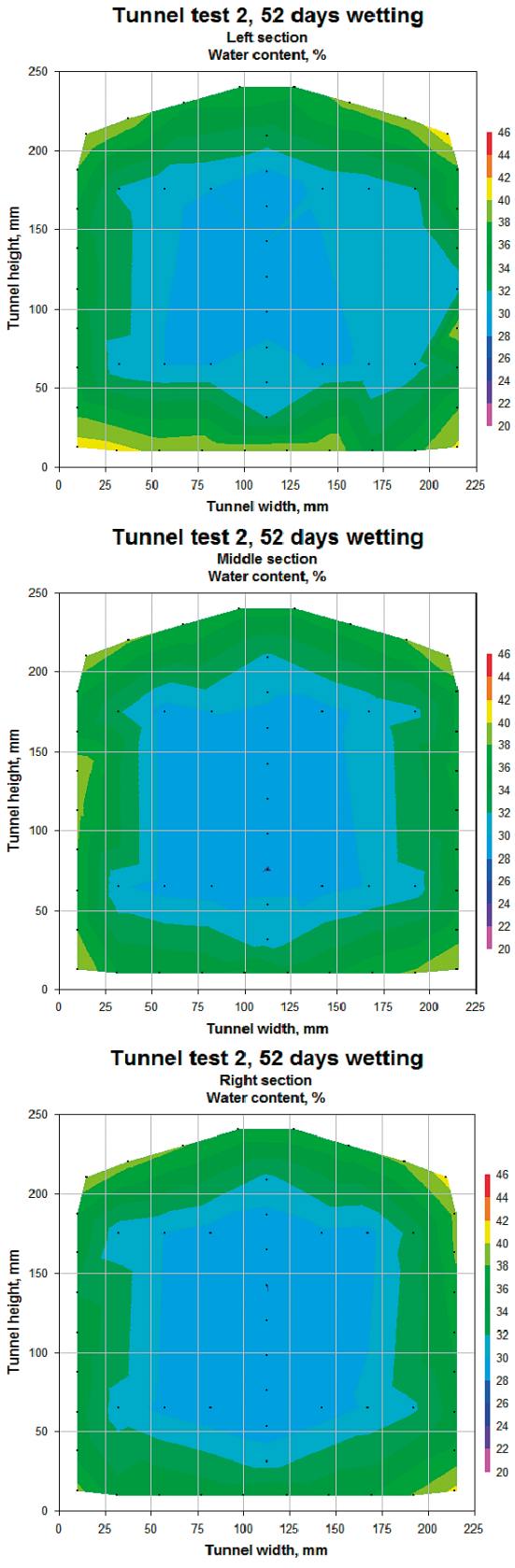

Figure A1-1. *Water content distribution in three cross-sections of Test 2 (left, middle and right).*

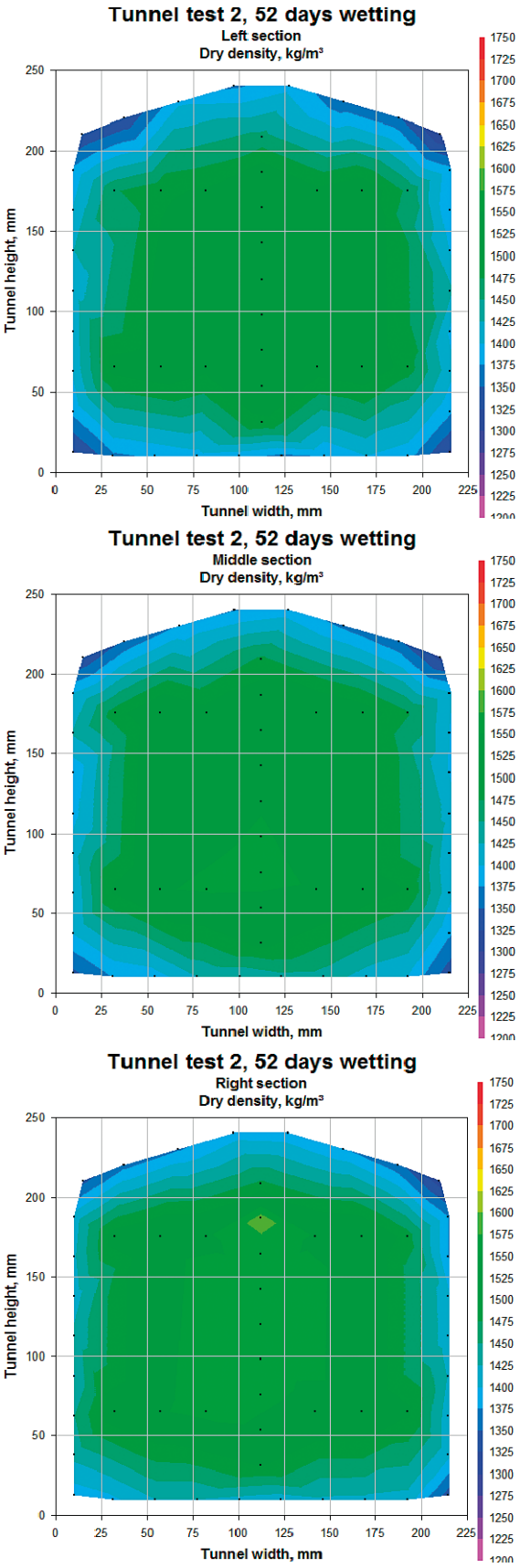

Figure A1-2. *Dry density distribution in three cross-sections of Test 2 (left, middle and right).*

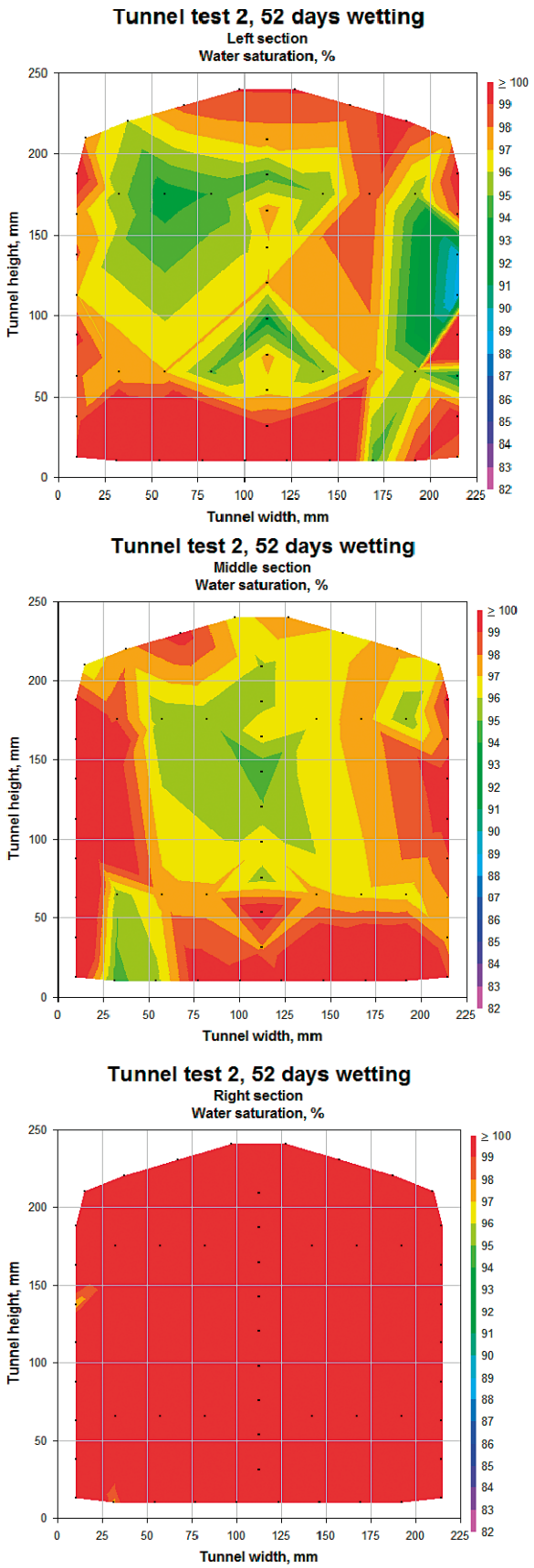

Figure A1-3. *Degree of water saturation distribution in three cross-sections of Test 2 (left, middle and right).*

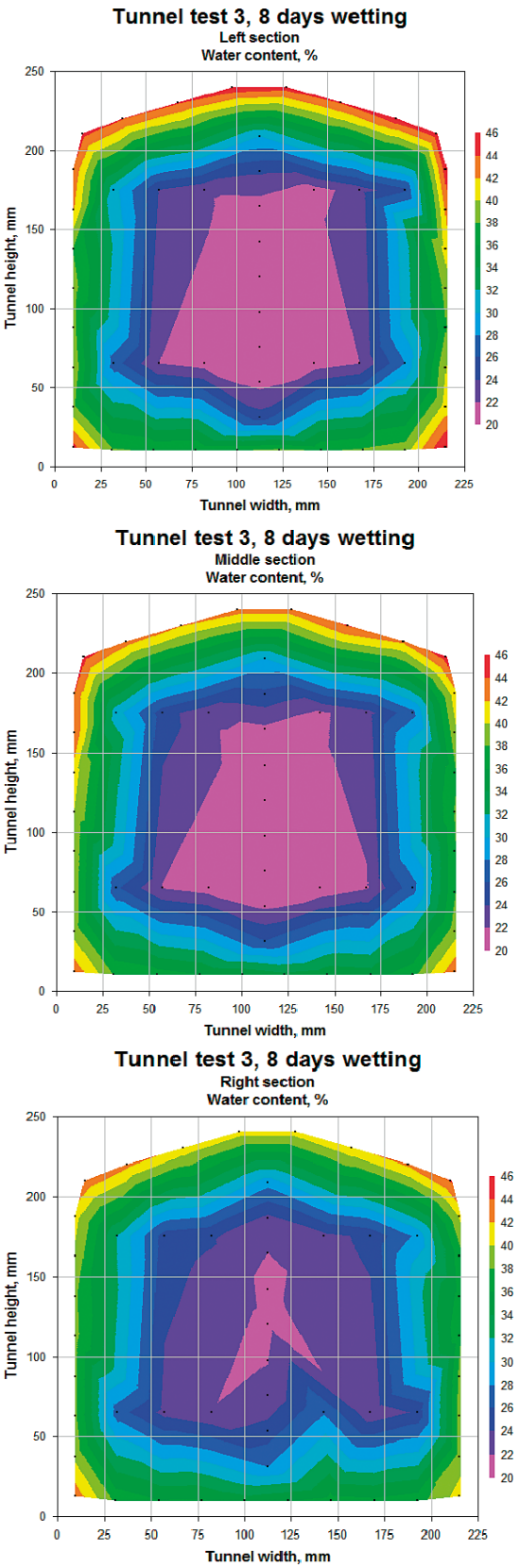

Figure A1-4. *Water content distribution in three cross-sections of Test 3 (left, middle and right).*

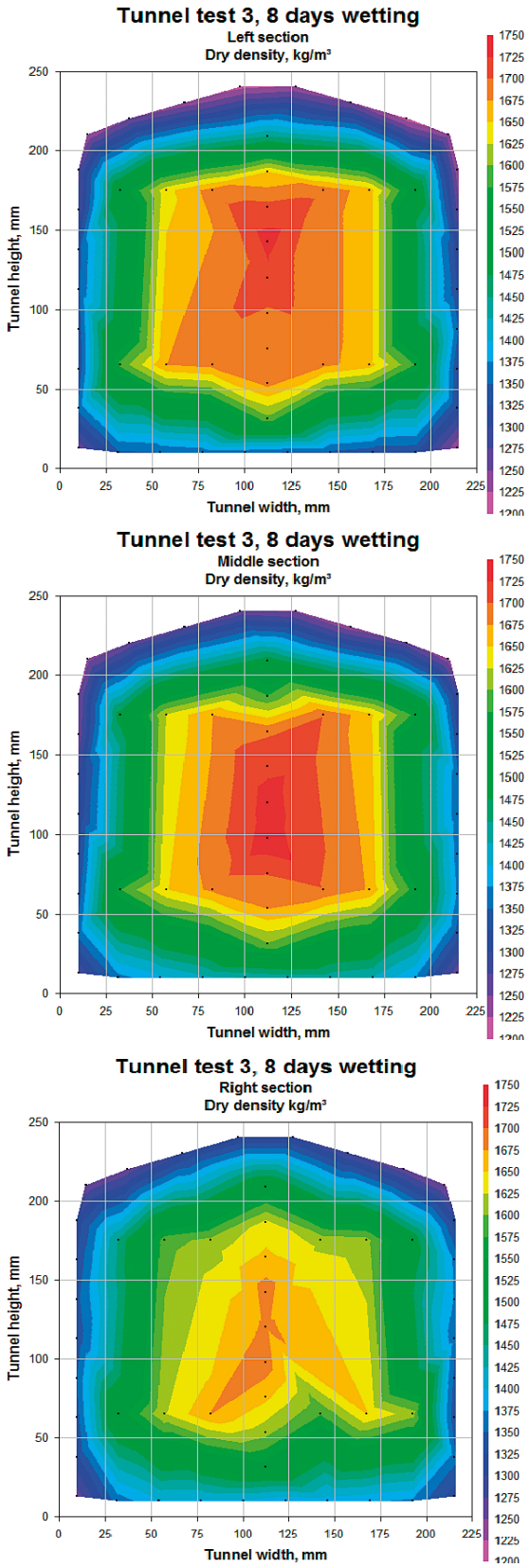

Figure A1-5. *Dry density distribution in three cross-sections of Test 3 (left, middle and right).*

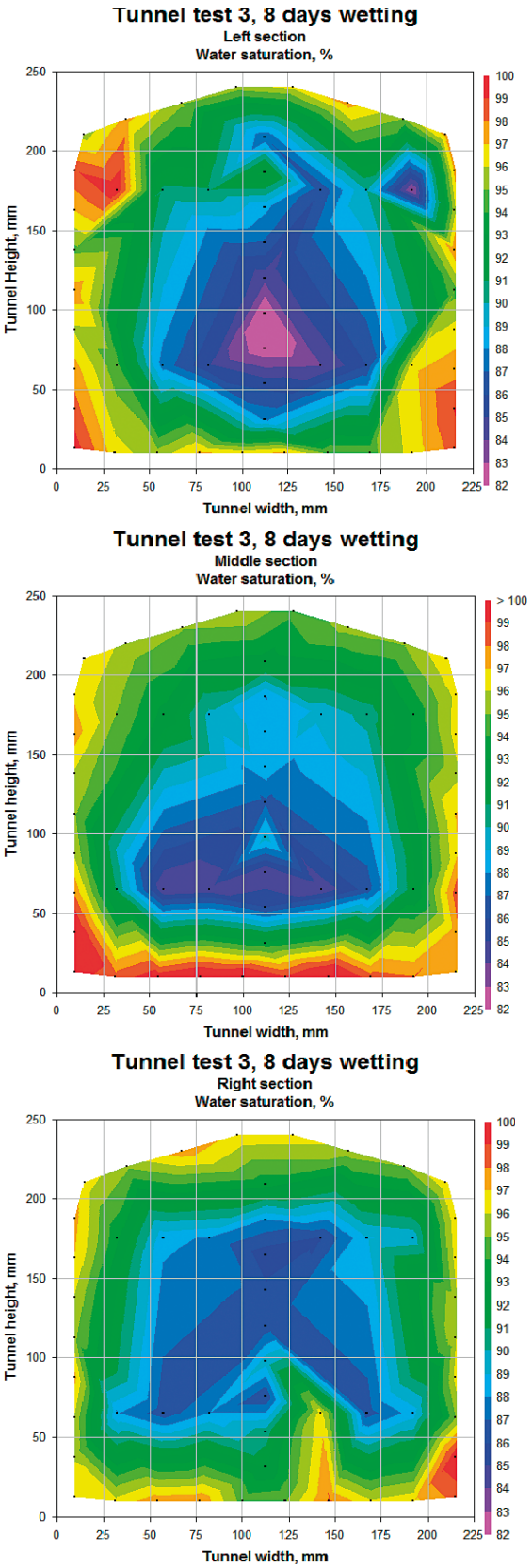

Figure A1-6. *Degree of water saturation distribution in three cross-sections of Test 3 (left, middle and right).*

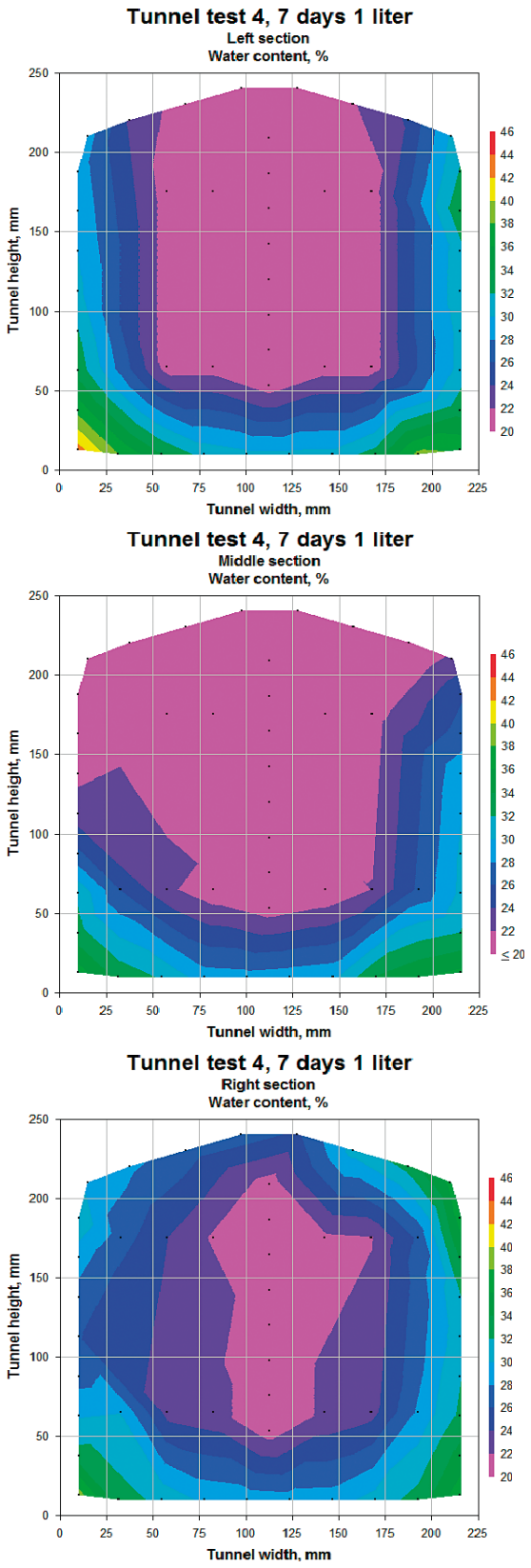

Figure A1-7. *Water content distribution in three cross-sections of Test 4 (left, middle and right).*

Appendix 2

Inflow to block joints – Test 1–18

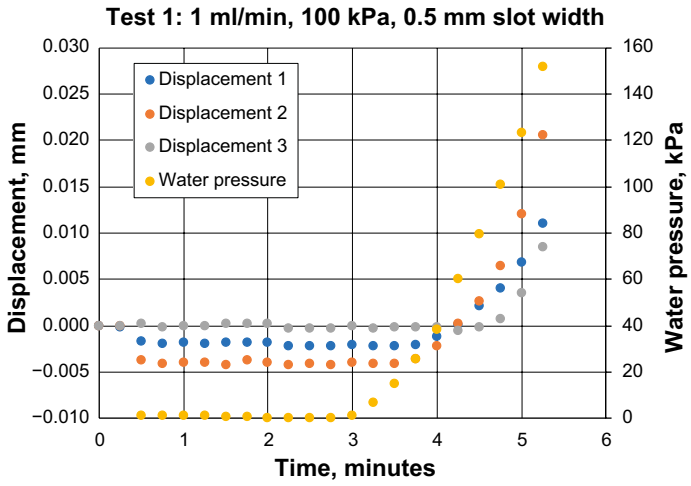

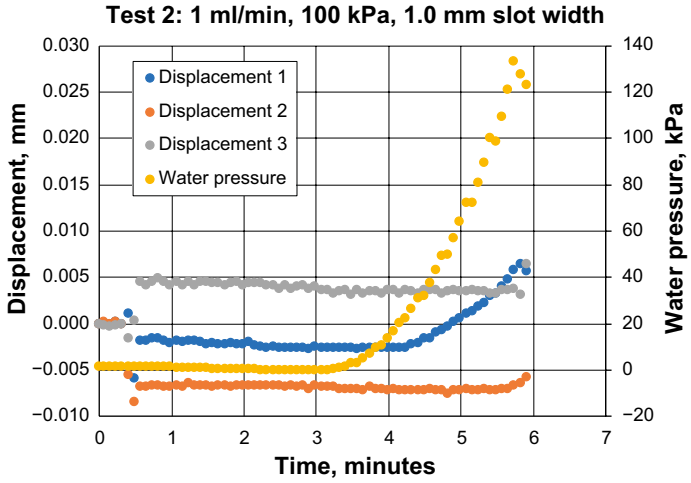

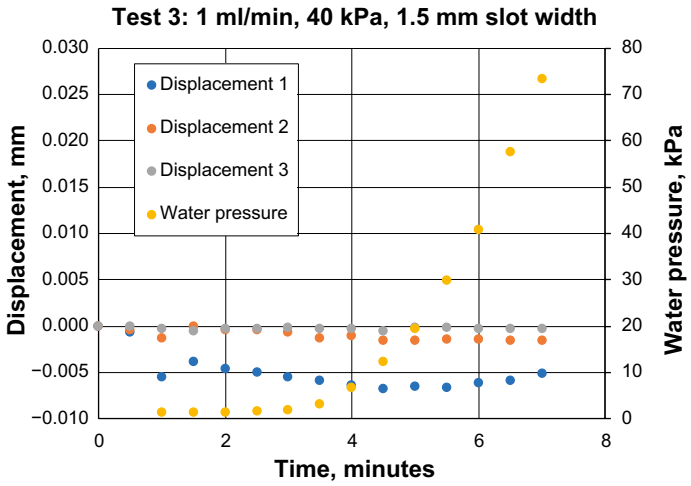

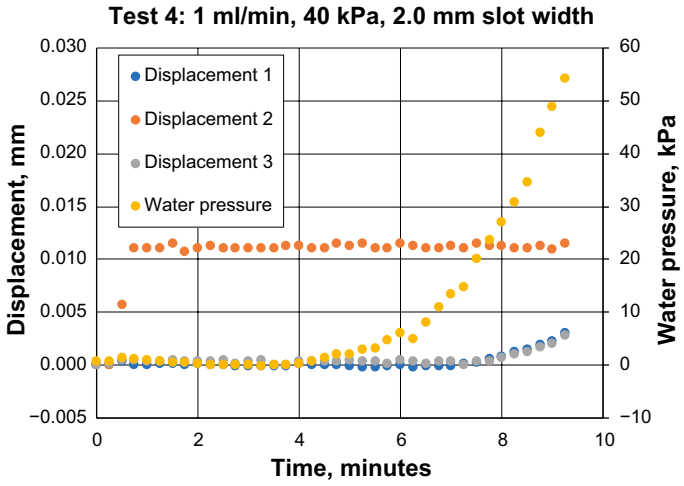
Test 4: 1 ml/min, 40 kPa, 2.0 mm slot width
Displacement 1
Displacement 2
Displacement 3
Water pressure
Displacement, mm
Water pressure, kPa
Time, minutes

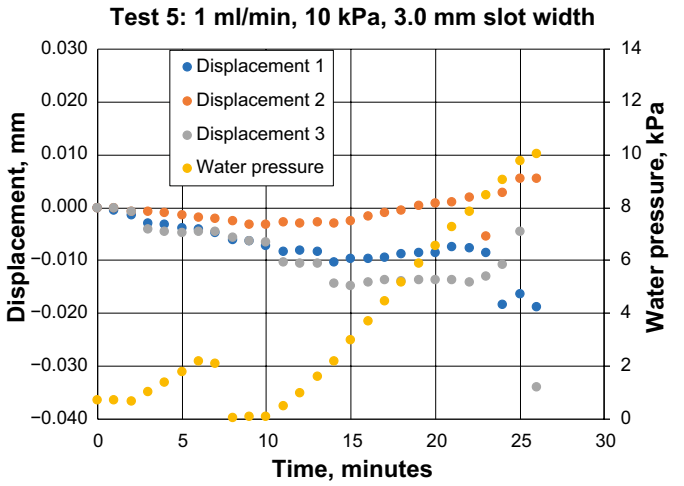
Test 5: 1 ml/min, 10 kPa, 3.0 mm slot width
Displacement 1
Displacement 2
Displacement 3
Water pressure
Displacement, mm
Water pressure, kPa
Time, minutes

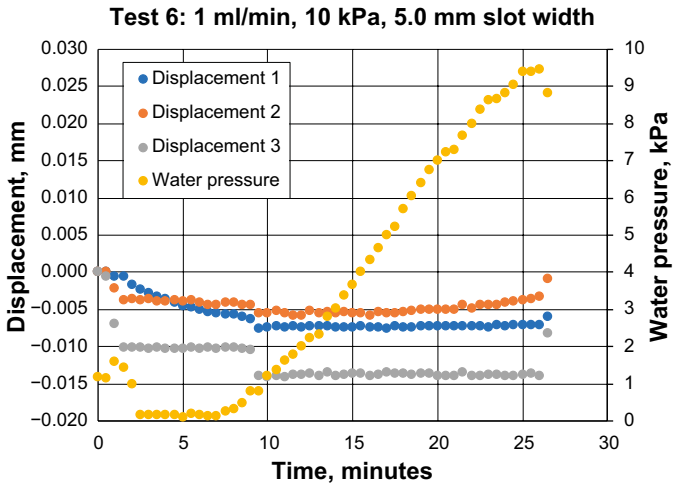
Test 6: 1 ml/min, 10 kPa, 5.0 mm slot width
Displacement 1
Displacement 2
Displacement 3
Water pressure
Displacement, mm
Water pressure, kPa
Time, minutes

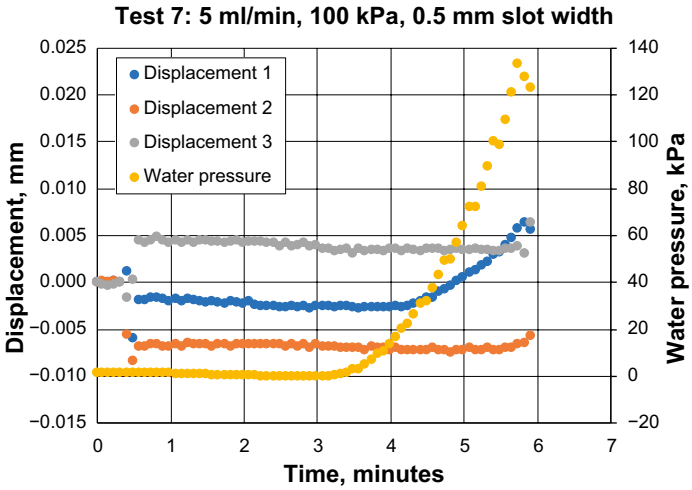
Test 7: 5 ml/min, 100 kPa, 0.5 mm slot width
Displacement 1
Displacement 2
Displacement 3
Water pressure
Displacement, mm
Water pressure, kPa
Time, minutes
0.025
0.020
0.015
0.010
0.005
0.000
−0.005
−0.010
−0.015
140
120
100
80
60
40
20
0
−20
0
1
2
3
4
5
6
7

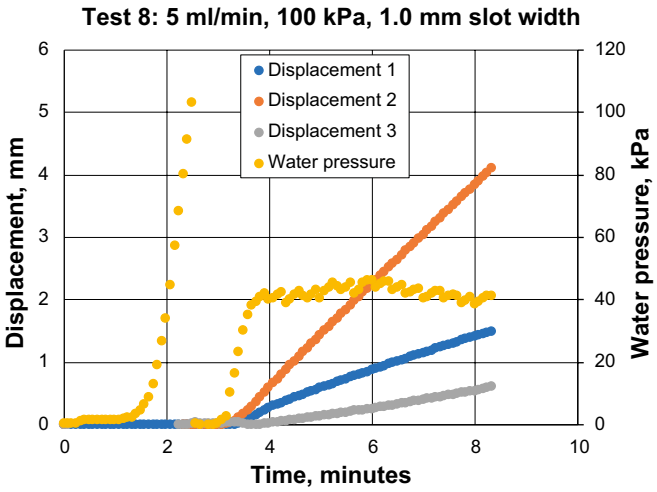
Test 8: 5 ml/min, 100 kPa, 1.0 mm slot width
Displacement 1
Displacement 2
Displacement 3
Water pressure
Displacement, mm
Water pressure, kPa
Time, minutes
6
5
4
3
2
1
0
120
100
80
60
40
20
0
0
2
4
6
8
10

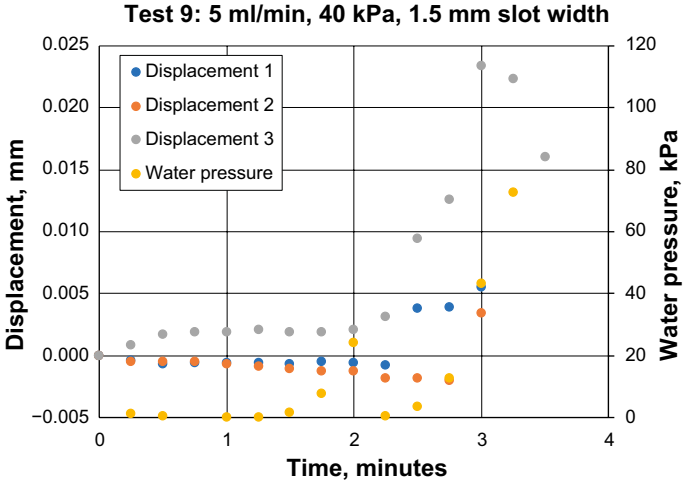
Test 9: 5 ml/min, 40 kPa, 1.5 mm slot width
Displacement 1
Displacement 2
Displacement 3
Water pressure
Displacement, mm
Water pressure, kPa
Time, minutes
0.025
0.020
0.015
0.010
0.005
0.000
−0.005
120
100
80
60
40
20
0
0
1
2
3
4

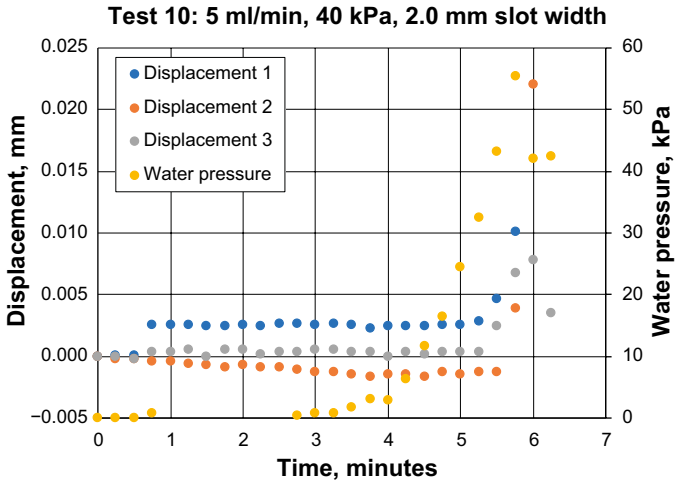
Test 10: 5 ml/min, 40 kPa, 2.0 mm slot width
Displacement 1
Displacement 2
Displacement 3
Water pressure
Displacement, mm
Water pressure, kPa
Time, minutes

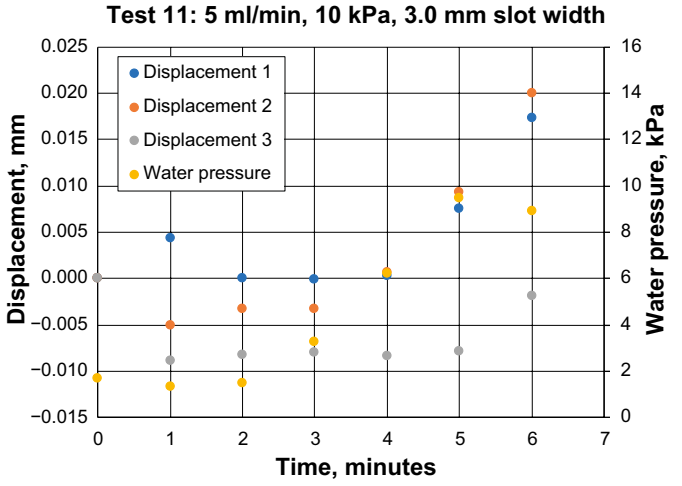
Test 11: 5 ml/min, 10 kPa, 3.0 mm slot width
Displacement 1
Displacement 2
Displacement 3
Water pressure
Displacement, mm
Water pressure, kPa
Time, minutes

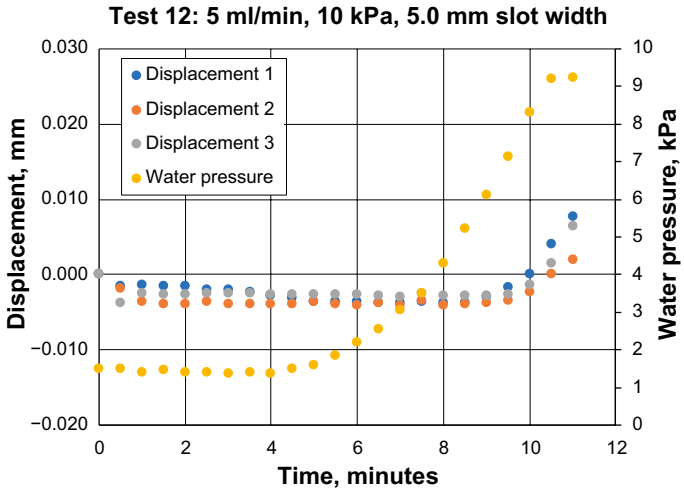
Test 12: 5 ml/min, 10 kPa, 5.0 mm slot width
Displacement 1
Displacement 2
Displacement 3
Water pressure
Displacement, mm
Water pressure, kPa
Time, minutes

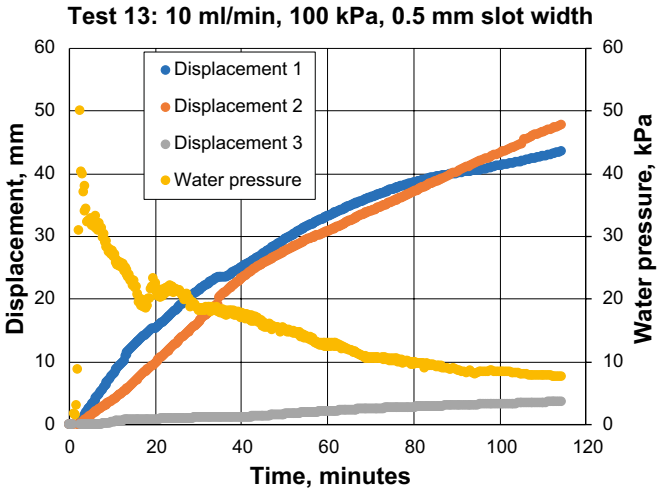
Test 13: 10 ml/min, 100 kPa, 0.5 mm slot width
Displacement 1
Displacement 2
Displacement 3
Water pressure
Displacement, mm
Water pressure, kPa
Time, minutes
0
10
20
30
40
50
60
0
20
40
60
80
100
120

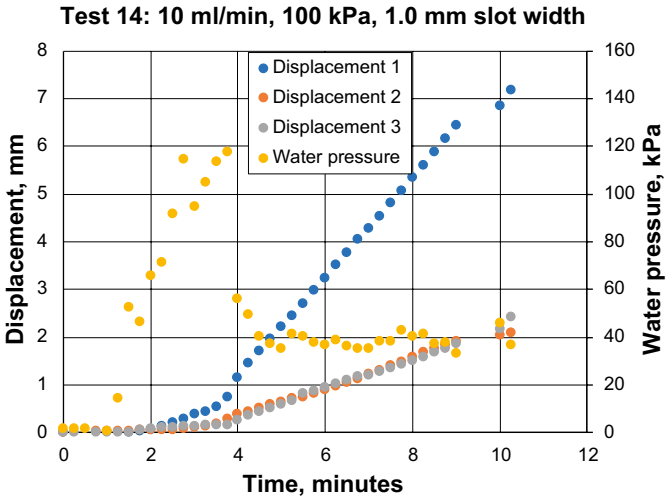
Test 14: 10 ml/min, 100 kPa, 1.0 mm slot width
Displacement 1
Displacement 2
Displacement 3
Water pressure
Displacement, mm
Water pressure, kPa
Time, minutes
0
1
2
3
4
5
6
7
8
0
20
40
60
80
100
120
140
160
0
2
4
6
8
10
12

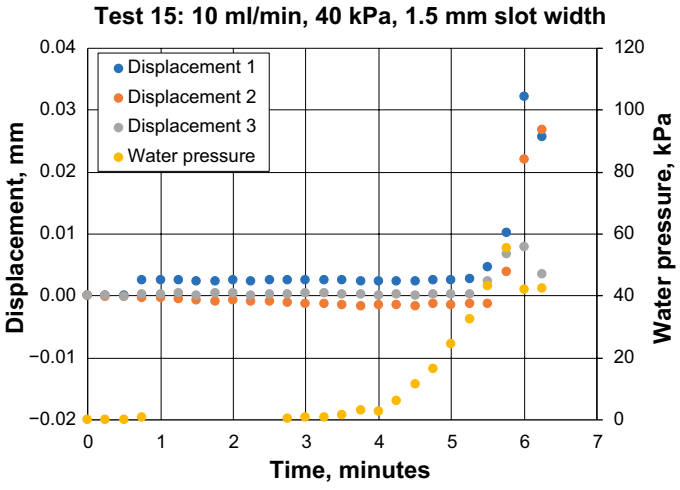
Test 15: 10 ml/min, 40 kPa, 1.5 mm slot width
Displacement 1
Displacement 2
Displacement 3
Water pressure
Displacement, mm
Water pressure, kPa
Time, minutes
0.04
0.03
0.02
0.01
0.00
−0.01
−0.02
120
100
80
60
40
20
0
0
1
2
3
4
5
6
7

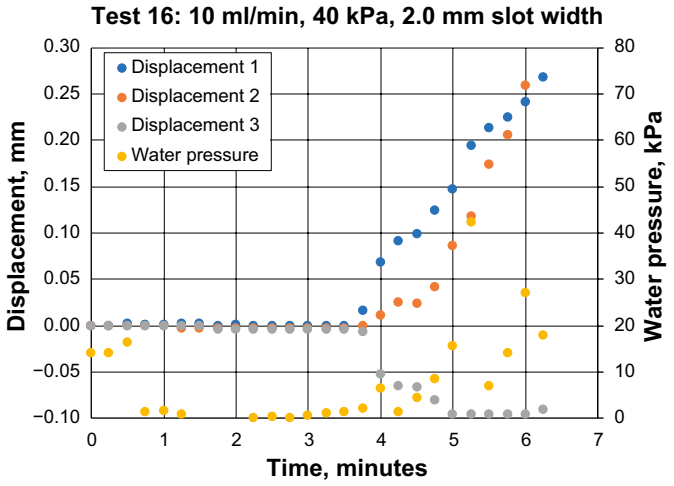
Test 16: 10 ml/min, 40 kPa, 2.0 mm slot width
Displacement 1
Displacement 2
Displacement 3
Water pressure
Displacement, mm
Water pressure, kPa
Time, minutes

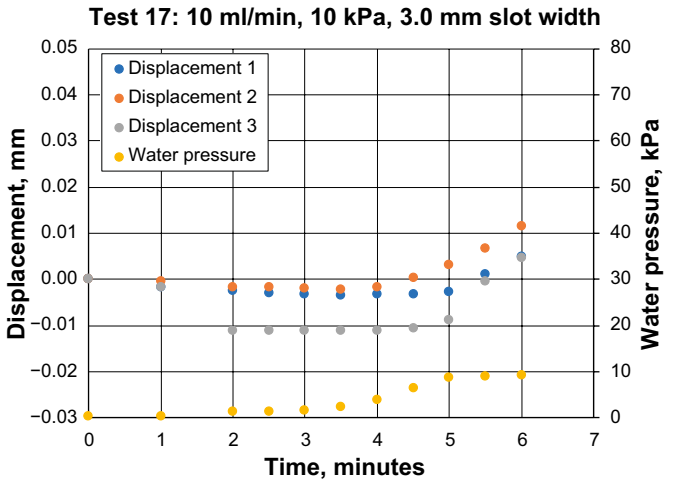
Test 17: 10 ml/min, 10 kPa, 3.0 mm slot width
Displacement 1
Displacement 2
Displacement 3
Water pressure
Displacement, mm
Water pressure, kPa
Time, minutes

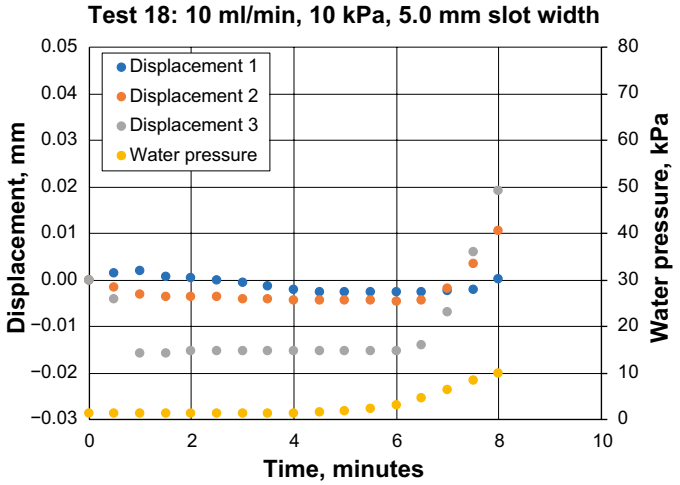
Test 18: 10 ml/min, 10 kPa, 5.0 mm slot width
Displacement 1
Displacement 2
Displacement 3
Water pressure
Displacement, mm
Water pressure, kPa
Time, minutes

Appendix 3

Deposition hole tests model identification

Case	Model directory name	Comment
BU1_D	GiD_M0_3_fine_corr.gid	
BU1_D	5deg/ GiD_M0_3_fine_corr.gid	5° friction angle (gen.dat edit)
BU1_D	10deg/ GiD_M0_3_fine_corr.gid	10° friction angle (gen.dat edit)
BU5_E3	DHE3_fine_5_corr.gid	
KBS_D	D_KBS_2_corr.gid	
KBS_E3	E3_KBS_5_corr.gid	

Mesh sensitivity check

Case	Model directory name	Comment
BU1_D	M0_3_fine/ DH_10_fineI2.gid	Directory-run, not final parameter setup
BU1_D	M0_3/DH_10_coarseI_constM.gid	Coarser discretization, not final parameter setup
BU1_D	GiD_M0_3_finer1.gid	Finer discretization, not final parameter setup

Appendix 4

Deposition hole tests mesh dependency study

No. elements: r-dir × a-dir			
Name	**Coarse**	**Fine**	**Finer**
S	9 × 13	18 × 26	34 × 52
C	5 × 50	10 × 100	20 × 200
CB	Top: 8 × 24 Bottom: 8 × 5	Top: 16 × 48 Bottom: 16 × 10	Top: 32 × 96 Bottom: 32 × 20
RB	3 × 50	6 × 100	12 × 200
PS	1 × 79	2 × 158	2 × 316

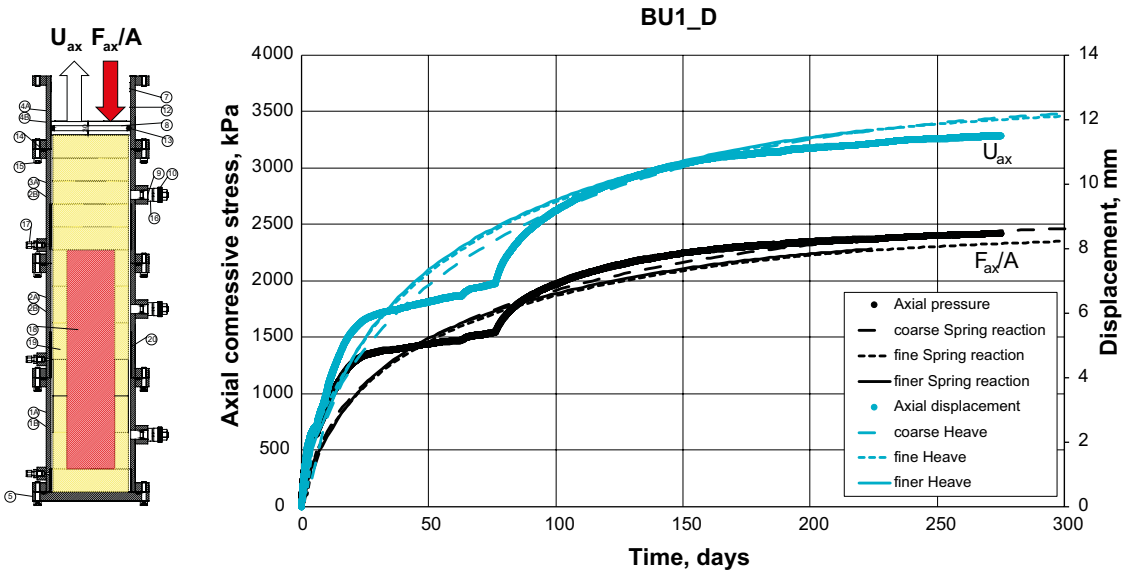

Figure A4-1. Accumulated water inflow.

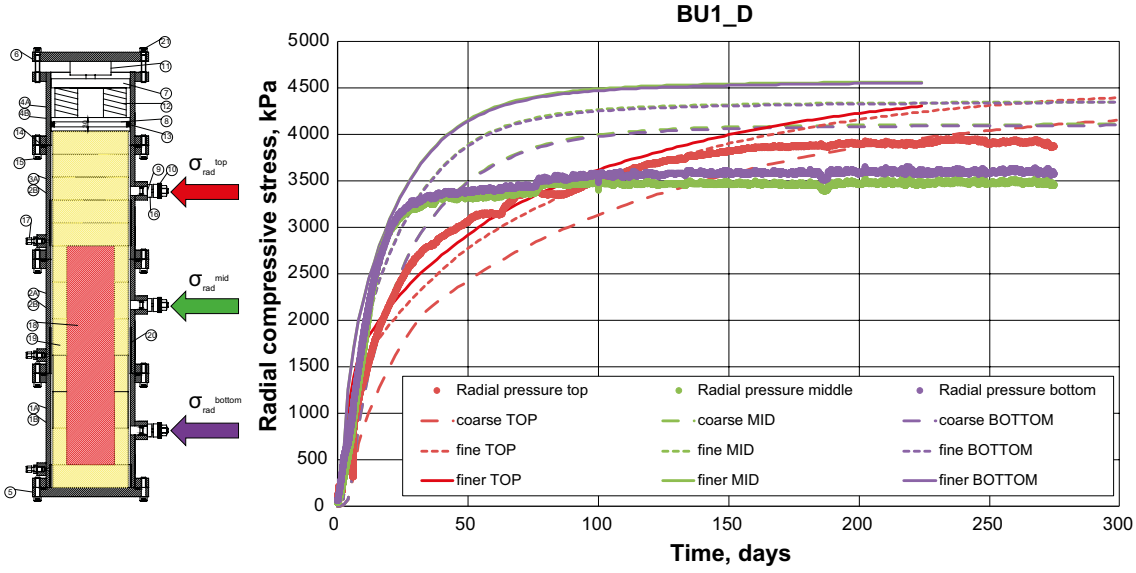

Figure A4-2. Accumulated water inflow.

Arkitektkopia AB, Bromma, 2020

SKB is responsible for managing spent nuclear fuel and radioactive waste produced by the Swedish nuclear power plants such that man and the environment are protected in the near and distant future.

skb.se